

---

# Investigation of stratospheric water vapour by means of the simulation of water isotopologues

Roland Eichinger

---



München 2014



---

# **Investigation of stratospheric water vapour by means of the simulation of water isotopologues**

**Roland Eichinger**

---

Dissertation  
an der Fakultät für Physik  
der Ludwig-Maximilians-Universität  
München

vorgelegt von  
Roland Eichinger  
aus München

München, den 03.06.2014

1. Gutachter: Prof. Dr. Robert Sausen

2. Gutachter: Prof. Dr. George Craig

Tag der mündlichen Prüfung: 17.07.2014



Doch immer höher steigt der edle Drang!  
Erlösung ist ein himmlisch leichter Zwang.  
Ein Aufgehäuftes, flockig lös't sich's auf,  
Wie Schäflein trippelnd, leicht gekämmt zu Hauf.  
So fließt zuletzt, was unten leicht entstand,  
Dem Vater oben still in Schoß und Hand.  
Howards Ehrengedächtnis, Cirrus, J.W. Goethe



# Contents

<b>Kurzfassung</b>	<b>ix</b>
<b>Abstract</b>	<b>xi</b>
<b>1 Introduction</b>	<b>1</b>
1.1 Motivation . . . . .	1
1.2 The potential of water isotopologues . . . . .	2
1.3 Science questions and strategy . . . . .	4
<b>2 Theoretical Background</b>	<b>7</b>
2.1 Water vapour in the stratosphere . . . . .	7
2.1.1 Pathways of water vapour into the stratosphere . . . . .	8
2.1.2 The chemical generation of water vapour . . . . .	11
2.1.3 Stratospheric water vapour and its climate effect . . . . .	12
2.2 Water isotopologues in the Earth's hydrological cycle . . . . .	15
2.2.1 Forms, abundances and notation . . . . .	16
2.2.2 Isotope fractionation . . . . .	17
2.2.3 Physical isotope processes in the hydrological cycle . . . . .	21
2.2.4 Chemical isotope fractionation in methane-oxidation . . . . .	24
2.2.5 Atmospheric processes derived from isotope ratios in precipitation .	25
<b>3 New EMAC model developments</b>	<b>27</b>
3.1 The EMAC model system . . . . .	27
3.1.1 The general circulation model ECHAM5 . . . . .	27
3.1.2 The submodel-coupling interface structure MESSy . . . . .	27
3.2 The TENDENCY submodel - preparatory work . . . . .	28
3.2.1 Implementation . . . . .	30
3.2.2 Diagnostic methods with TENDENCY . . . . .	35
3.2.3 Runtime performance analysis . . . . .	37
3.2.4 Process analysis of stratospheric water vapour . . . . .	38
3.3 The H2OISO submodel for stable water isotopologues . . . . .	41
3.3.1 A second hydrological cycle including water isotopologues . . . . .	43
3.3.2 Vertical diffusion . . . . .	43
3.3.3 Surface processes . . . . .	45
3.3.4 Advection . . . . .	46
3.3.5 Clouds - large-scale and convective . . . . .	46

3.3.6	Methane oxidation . . . . .	48
3.4	Setup of the model simulations . . . . .	51
3.4.1	The T31L39MA simulation (FREE_VAL) setup . . . . .	51
3.4.2	The T42L90MA simulation (SD_REF) setup . . . . .	52
<b>4</b>	<b>Evaluation of the H2OISO submodel</b>	<b>53</b>
4.1	Correctness of the second hydrological cycle . . . . .	53
4.1.1	Correctness of individual processes and the numerical error . . . . .	53
4.1.2	Analysis of the numerical error . . . . .	54
4.2	Evaluation of tropospheric isotope quantities . . . . .	55
4.2.1	Comparison with GNIP data . . . . .	56
4.2.2	Comparison with the ECHAM5-wiso model . . . . .	61
4.2.3	Discussion of the model results in the troposphere . . . . .	64
4.3	Evaluation of stratospheric isotope quantities . . . . .	64
4.3.1	Comparison of $\delta D(CH_4)$ with the CHEM2D model . . . . .	65
4.3.2	Comparison of $\delta D(CH_4)$ with balloon-borne observations . . . . .	66
4.3.3	Comparison of HDO with in situ observations . . . . .	69
4.3.4	Comparison of HDO and $\delta D(H_2O)$ with satellite observations . . . . .	70
4.3.5	Discussion of the model results in the stratosphere . . . . .	77
<b>5</b>	<b>Analysis of stratospheric water isotope ratios</b>	<b>81</b>
5.1	Time series of stratospheric $\delta D(H_2O)$ . . . . .	81
5.2	The impact of methane oxidation on $\delta D(H_2O)$ . . . . .	83
5.3	The origin of the $\delta D(H_2O)$ tape recorder . . . . .	88
5.4	The impact of ice lofting on stratospheric $\delta D(H_2O)$ . . . . .	95
5.5	Discussion of the analysis . . . . .	98
<b>6</b>	<b>Conclusions and Outlook</b>	<b>101</b>
6.1	Summary . . . . .	101
6.2	Conclusions . . . . .	106
	<b>Bibliography</b>	<b>109</b>
<b>A</b>	<b>Abbreviations</b>	<b>127</b>
<b>B</b>	<b>MESSy TENDENCY user manual</b>	<b>129</b>
B.1	Introduction . . . . .	129
B.2	Subroutines called from BMIL . . . . .	129
B.3	Subroutines and functions called from SMIL . . . . .	130
B.4	User interface . . . . .	133
B.5	Private subroutines . . . . .	134
	<b>Danksagung</b>	<b>137</b>
	<b>Lebenslauf</b>	<b>138</b>

# Kurzfassung

Diese Modellstudie hat ein besseres Verständnis jener Prozesse zum Ziel, die das Wasserdampfbudget in der Stratosphäre bestimmen und stützt sich auf die Untersuchung des Isotopenverhältnisses von Wasser. Zunächst wurde ein eigenständiger hydrologischer Zyklus in das Chemie-Klimamodell EMAC eingebaut, welcher die Wasserisotopologe HDO und  $\text{H}_2^{18}\text{O}$  sowie deren physikalische Fraktionierungsprozesse enthält. Zusätzlich wurde eine explizite Berechnung des Beitrages der Methanoxidation zu HDO eingefügt. EMAC simuliert eine hochaufgelöste tropische Tropopausenschicht sowie explizite Stratosphärendynamik. Mit diesen Modellerweiterungen ist es nun möglich, genaue Analysen von Wasserdampf und dessen Isotopenverhältnis im Bezug auf Deuterium ( $\delta\text{D}(\text{H}_2\text{O})$ ) in der gesamten Stratosphäre, sowie im Übergangsbereich zur Troposphäre durchzuführen.

Um die korrekte Darstellung der Wasserisotopologe im hydrologischen Zyklus des Modells zu gewährleisten, wurde das erweiterte System in mehreren Schritten evaluiert. Die physikalischen Fraktionierungseffekte wurden in einem Vergleich der simulierten Isotopenverhältnisse im Niederschlag mit Messungen eines Netzwerkes an Bodenstationen (GNIP) und mit Ergebnissen einer, mit Wasserisotopologen ausgestatteten, ECHAM5 Modellversion evaluiert. Die Güte des simulierten chemischen HDO-Vorläufers  $\text{CH}_3\text{D}$  in der Stratosphäre des Modells wurde durch einen Vergleich der Ergebnisse mit chemischen Transportmodellen (CHEM1D, CHEM2D) und Messungen von Radiosondenaufstiegen überprüft. Abschließend wurde simuliertes HDO und  $\delta\text{D}(\text{H}_2\text{O})$  anhand von Messungen drei verschiedener Satelliteninstrumente (MIPAS, ACE-FTS, SMR) evaluiert.

Abweichungen im  $\delta\text{D}(\text{H}_2\text{O})$  zwischen zwei der drei satellitengestützten Beobachtungen können nun teilweise erklärt werden. Der simulierte Jahresgang von tropischem  $\delta\text{D}(\text{H}_2\text{O})$  in der Stratosphäre weist ein schwaches 'tape recorder' Signal auf, welches sich in Höhen um 25 km auflöst. Dieses Ergebnis ist zwischen das ausgeprägte 'tape recorder' Signal in MIPAS-Beobachtungen und die nicht erkennbare vertikale Ausbreitung des Jahresgangs in ACE-FTS-Messungen einzuordnen. Die Beseitigung unterschiedlicher Mängel in den jeweiligen Satellitenmessungen lässt jedoch eine Veränderung beider Beobachtungsdatensätze in Richtung der Ergebnisse des EMAC Modells erwarten.

Eingehende Analysen der Wasserisotopenverhältnisse in der EMAC Simulation haben die für den stratosphärischen  $\delta\text{D}(\text{H}_2\text{O})$ - 'tape recorder' verantwortlichen Prozesse aufgezeigt. Eine Sensitivitätsstudie ohne Einfluss der Methanoxidation auf  $\delta\text{D}(\text{H}_2\text{O})$  veranschaulicht den dämpfenden Einfluss dieses chemischen Prozesses auf das 'tape recorder' Signal. Eine Untersuchung des Ursprungs des erhöhten  $\delta\text{D}(\text{H}_2\text{O})$  in der unteren Stratosphäre im Nordsommer weist isotopisch angereicherten Wasserdampf nach, welcher die Tropopause über dem subtropischen Westpazifik durchquert. Eine Korrelationsanalyse bestätigt diese Verbindung und kennzeichnet damit den Asiatischen Sommermonsun als den wesentlichen

beitragenden Faktor zum stratosphärischen  $\delta D(H_2O)$ -’tape recorder’. Dieses Ergebnis steht im Gegensatz zu einer Auswertung von ACE-FTS-Satellitendaten, welche den  $\delta D(H_2O)$  Anstieg in der unteren Stratosphäre im Nordsommer dem Nordamerikanischen Monsun zuweist. Als mögliche Erklärung für diesen Widerspruch konnte das, in dem verwendeten Konvektionsschema unzureichend auftretende, konvektive Überschießen von Wolkeneis ausgemacht werden.

# Abstract

This modelling study aims to gain an improved understanding of the processes that determine the water vapour budget in the stratosphere by means of the investigation of water isotope ratios. At first, a separate hydrological cycle has been introduced into the chemistry-climate model EMAC, including the water isotopologues HDO and  $\text{H}_2^{18}\text{O}$  and their physical fractionation processes. Additionally, an explicit computation of the contribution of methane oxidation to HDO has been incorporated. EMAC simulates explicit stratospheric dynamics and a highly resolved tropical tropopause layer. These model expansions, now allow detailed analyses of water vapour and its isotope ratio with respect to deuterium ( $\delta\text{D}(\text{H}_2\text{O})$ ), throughout the stratosphere and in the transition region to the troposphere.

In order to assure the correct representation of the water isotopologues in the model's hydrological cycle, the expanded system has been evaluated in several steps. The physical fractionation effects have been evaluated by comparison of the simulated isotopic composition of precipitation with measurements from a ground-based network (GNIP) and with the results from an isotopologue-enabled ECHAM5 general circulation model version. The model's representation of the chemical HDO precursor  $\text{CH}_3\text{D}$  in the stratosphere has been confirmed by a comparison with chemical transport models (CHEM1D, CHEM2D) and measurements from radiosonde flights. Finally, the simulated HDO and  $\delta\text{D}(\text{H}_2\text{O})$  have been evaluated in the stratosphere, with respect to retrievals from three different satellite instruments (MIPAS, ACE-FTS, SMR).

Discrepancies in stratospheric  $\delta\text{D}(\text{H}_2\text{O})$  between two of the three satellite retrievals can now partly be explained. The simulated seasonal cycle of tropical  $\delta\text{D}(\text{H}_2\text{O})$  in the stratosphere exhibits a weak tape recorder signal, which fades out at altitudes around 25 km. This result ranges between the pronounced tape recorder signal in the MIPAS observations and the missing upward propagation of the seasonal variations in the ACE-FTS retrieval. Revisions of different insufficiencies in the respective satellite measurements, however, are expected to alter both observational datasets towards the results of the EMAC model.

Extensive analyses of the water isotope ratios have revealed the driving mechanisms of the stratospheric  $\delta\text{D}(\text{H}_2\text{O})$  tape recorder signal in the EMAC simulation. A sensitivity study without the impact of methane oxidation on  $\delta\text{D}(\text{H}_2\text{O})$  demonstrates the damping effect of this chemical process on the tape recorder signal. An investigation of the origin of the enhanced  $\delta\text{D}(\text{H}_2\text{O})$  in the lower stratosphere during boreal summer, shows isotopically enriched water vapour, crossing the tropopause over the subtropical Western Pacific. A correlation analysis confirms this link, and thus the Asian Summer Monsoon could be identified to be the major contributing process for the stratospheric  $\delta\text{D}(\text{H}_2\text{O})$  tape recorder. This finding contradicts an analysis of ACE-FTS satellite data, which assigns the lower

stratospheric  $\delta D(H_2O)$  increase during boreal summer to the North American Monsoon. A possible explanation for this discrepancy has been found to be an underrepresentation of convective ice overshooting in the applied convection scheme.



# Chapter 1

## Introduction

### 1.1 Motivation

Water vapour is the most important greenhouse gas. It absorbs and emits infrared radiation and thereby warms the troposphere. Solomon et al. (2010) attribute 30% of the temperature change since 1980 to the radiative forcing of increased stratospheric water vapour. Furthermore, stratospheric water vapour has the potential to influence ozone destruction. According to Stenke and Grewe (2005), 10% of the global total ozone decline from 1960 to 1999 can be explained by the water vapour increase.

The mechanisms driving long-term changes in stratospheric water vapour are not well understood (Füglister et al., 2009). Chemistry climate models (CCMs) predict increases of stratospheric water vapour, but the confidence in these predictions is low. The models have a poor representation of the seasonal cycle of the tropical tropopause temperatures and of past changes in stratospheric water vapour abundances (WMO, 2006; IPCC, 2007).

Stratospheric water vapour is determined by in situ methane oxidation and the intrusion of water vapour through the tropical tropopause layer (TTL), which is considered as the “gate to the stratosphere” (Füglister et al., 2009). The contribution of methane oxidation depends on changing emissions and stratospheric circulation patterns. The transport of water vapour from the troposphere into the stratosphere is strongly controlled by the tropopause temperature, which leads to a drop of water vapour mixing ratios of four orders of magnitude from the surface to the lower stratosphere.

The seasonal cycle of lower stratospheric water vapour in the tropics is characterised by the tape recorder (Mote et al., 1996), which exhibits a hydrated lower stratosphere in boreal summer and a dry lower stratosphere in boreal winter. Thus, most of the water vapour enters the stratosphere during boreal summer, when Monsoon systems (e.g. Gettelman and Kinnison, 2004) and enhanced deep convection over the tropics (e.g. Khaykin et al., 2009) transport water vapour into the TTL. The influence of the individual mechanisms on the overall intrusion of water vapour into the stratosphere, however, is poorly quantified. The net effect of direct injection of ice crystals into the lower stratosphere through overshooting convection, is even under debate of hydrating or dehydrating the stratosphere (see e.g. Grosvenor et al., 2007; Corti et al., 2008). In order to quantify the contributions of the individual processes to the stratospheric water vapour budget, they need to be understood

in more detail. This will lead to an improved representation of the hydrological cycle in CCMs, thus a better representation of the variations of stratospheric water vapour mixing ratios can be achieved and therefore climate projections gain reliability.

## 1.2 The potential of water isotopologues

The application of water isotopologues (see Sect. 2.2) in tracer studies has the potential to answer the open questions concerning the stratospheric water vapour budget. Water isotopologues are characterised by small mass differences compared to 'normal' water. This causes differences in the respective zero-point energies and therewith physical and chemical fractionation effects during phase changes and chemical reactions (Dansgaard, 1964; Mook, 2000a). These lead to an enrichment of the lighter isotopologues in the more diffusive phase and in the products of chemical reactions. The individual processes, which control the water vapour budget in the stratosphere, are characterised by certain fractionation effects, which leave an isotopic fingerprint in the respective water vapour compound (Johnson et al., 2001a).

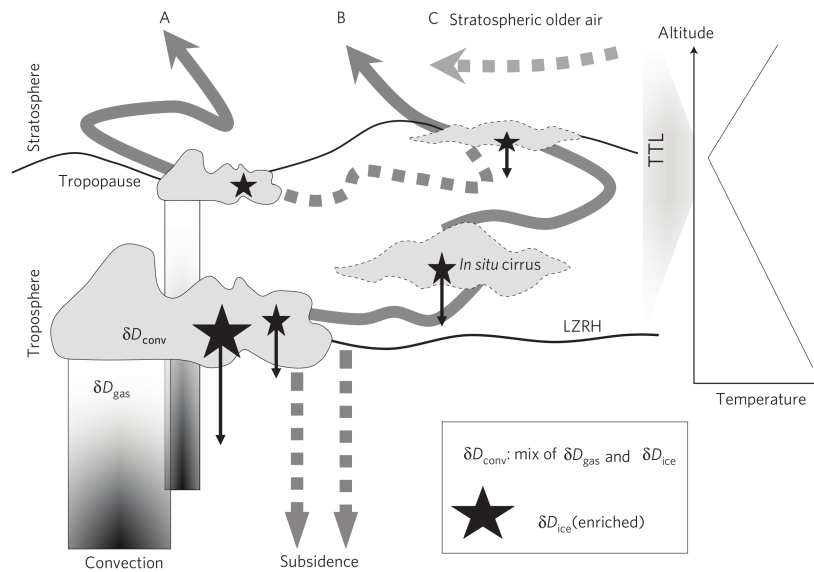


Figure 1.1: Schematic of the different pathways of water vapour through the tropics into the stratosphere (Steinwagner et al., 2010).

Fig. 1.1 illustrates the different pathways of water vapour into the lower stratosphere and their influence on its isotopic composition with respect to deuterium. Direct injection of ice into the stratosphere through deep convection (A) has the potential to isotopically enrich the stratospheric water vapour, if the ice crystals sublime within the stratosphere. Convectively lofted air that detrains above the Level of Zero net Radiative Heating (LZRH) will be further dehydrated during ascent by in situ formation of cirrus clouds (B). Since the isotopically enriched ice crystals subside in the following, isotopically depleted water vapour reaches the stratosphere on this pathway. The in-mixing of older stratospheric air

(C), which has experienced  $\text{H}_2\text{O}$  and  $\text{HDO}$  production through the oxidation of  $\text{CH}_4$  and  $\text{CH}_3\text{D}$ , also possesses a distinct isotopic signature. These processes constitute an offset of the isotope ratios in upper troposphere lower stratosphere (UTLS) from simple Rayleigh distillation (Steinwagner et al., 2010).

This elucidates the potential of water isotopologues for the investigation of the processes, that determine the stratospheric water vapour budget. Every process leaves a fingerprint in the water vapour isotope ratio. The responsible mechanisms can be detected through the isotopic signature, which they preserve on their way into the lower stratosphere. Spatial and temporal differences, as well as variations and trends in the isotopic composition, hence allow conclusions to the causes that lie behind changes of the budget of stratospheric water vapour itself.

Water isotopologues have long been used in paleoclimate studies, e.g. for reconstructing temperature changes, with the assistance of ice cores or data from other proxy records (Bradley, 1999), as well as with isotopologue-enabled circulation models (e.g. Joussaume et al., 1984). Due to an increasing number of reliable measurements of water isotopologues by in situ and remote sensing instruments, it is now also possible to evaluate simulations of water isotopologues in compounds other than precipitation and its archives. Subsequently, this also allows the analysis of the isotopic composition of stratospheric water vapour with global CCMs.

Model studies of water isotopologues in the TTL and in the stratosphere include approaches from conceptional (Dessler and Sherwood, 2003; Bolot et al., 2013), to one-dimensional (Ridal et al., 2001; Zahn et al., 2006) and two-dimensional (Ridal and Siskind, 2002) models. Schmidt et al. (2005) also applied a Global Circulation Model (GCM), in order to study stratospheric entry values of the isotope ratios of water vapour. However, this model has a comparatively low resolution in the stratosphere and the accounting for methane oxidation is prescribed with a fixed production rate.

Air borne in situ measurements of water isotopologues were carried out in high altitudes (Johnson et al., 2001b; Coffey et al., 2006; Hanisco et al., 2007; Sayres et al., 2010). Moreover, instruments on satellites are now able to observe the water vapour isotope composition in the stratosphere (Urban et al., 2007; Steinwagner et al., 2007; Randel et al., 2012) with a temporal and spatial coverage, which allows to obtain a global picture.

The different satellite retrievals, however, show considerable differences, when comparing profiles and annual cycles of  $\text{HDO}$  mixing ratios and isotope ratios, respectively, in the TTL and the stratosphere. Lossow et al. (2011) presented a comprehensive comparison of the observations of  $\text{HDO}$  of three different satellite instruments (Odin/SMR, ENVISAT/MIPAS and SCISAT/ACE-FTS). All in all favourable results of the comparison also yield large deviations between particular instruments caused by uncertainties in spectroscopic parameters. Moreover, certain regions, including the TTL, are subject of particularly large differences between the satellite retrievals.

Furthermore, Steinwagner et al. (2010) found a tape recorder signal in the water vapour isotope ratios in the tropical stratosphere in the MIPAS (Michelson Interferometer for Passive Atmospheric Sounding) observations, comparable to the known tape recorder in water vapour mixing ratios. This pattern could be explained by enhanced ice overshooting through deep convection during boreal summer, which increases the water vapour isotope

ratios in the lower stratosphere. Randel et al. (2012), in contrast, did not find an analogue upward propagation of the seasonal cycle of water vapour isotope ratios in the stratosphere, when analysing ACE-FTS data. This substantial difference in both observations can be due to several reasons. Randel et al. (2012) state that the low vertical resolution of MIPAS could lead to a confusion of a Monsoon signal with the tape recorder. Also, the difference between the horizontal resolutions of the  $\text{H}_2\text{O}$  and the  $\text{HDO}$  retrievals in MIPAS can amplify the  $\delta\text{D}(\text{H}_2\text{O})$  tape recorder signal (S. Lossow, personal communication, 2014). In addition to that, the sparse temporal sampling of the ACE-FTS (Atmospheric Chemistry Experiment - Fourier Transform Spectrometer) data may conceal the tape recorder signal. Before drawing conclusions to the reasons for variations of water vapour, itself, an improved understanding of the basic structure of the water isotope ratios in the stratosphere is necessary.

### 1.3 Science questions and strategy

The science questions, that lead to this study are stated as follows:

- What processes control the water vapour tape recorder in the stratosphere?
- Are the observed patterns of the deuterium water vapour isotope composition in the stratosphere reproducible with a global climate chemistry model and can the reasons for the discrepancies between the observations be solved?
- To what extent are the individual physical and chemical processes contributing to the patterns of the isotope composition of stratospheric water vapour?
- How can the simulated water isotope ratios serve for further investigations of the trends and variations in the stratospheric water vapour budget?

A detailed investigation of stratospheric water isotopologues requires not only measurements, but also the comprehensive simulation of the physical and chemical isotope processes in a well resolved global CCM with explicit stratospheric dynamics. For this purpose the water isotopologues  $\text{HDO}$  and  $\text{H}_2^{18}\text{O}$  are here implemented into the EMAC (ECHAM MESSy Atmospheric Chemistry) model (Jöckel et al., 2005, 2010). EMAC provides the opportunity to accurately analyse troposphere-stratosphere exchange processes on a global scale, since it comprises a GCM with a highly resolved tropopause region and explicit stratospheric dynamics. Additionally, it includes optional chemical mechanisms, which are needed for the correct representation of water vapour and its isotopologues in the stratosphere. In addition to that, the modular approach of the model allows a flexible implementation of extensions.

In order to evaluate the representation of the water isotopologues in the model, as a first step, the isotope ratios in precipitation are evaluated. This is conducted through a comparison of EMAC with long-term measurements of isotope ratios in precipitation provided by the GNIP (Global Network on Isotopes in Precipitation) measurement survey (IAEA, 2009) and with results from the ECHAM5-wiso model (Werner et al., 2011). Herewith

the confirmation of the correct representation of the fractionation processes during phase transitions is achieved.

The accounting for the influence of methane oxidation on atmospheric HDO requires the computation of the methane isotopologue  $\text{CH}_3\text{D}$ . In a next step, this tracer is evaluated with respect to chemical transport models (CHEM1D, CHEM2D, Ridal et al., 2001; Ridal and Siskind, 2002) and measurements from radiosonde flights (Röckmann et al., 2011). A high resolution EMAC simulation with specified dynamics of the last decades is performed for this evaluation. The results of this simulation are also applied to compare the stratospheric HDO mixing ratios and the water vapour isotope ratios, respectively, with different satellite observations (SMR, MIPAS, ACE-FTS, Urban et al., 2007; Steinwagner et al., 2010; Randel et al., 2012). This comparison yields a more complete picture of the isotopic composition of stratospheric water vapour. Finally, the results of the simulation are analysed, aiming to identify the processes, which determine the isotopic signature of stratospheric water vapour.



# Chapter 2

## Theoretical Background

### 2.1 Water vapour in the stratosphere

Water vapour is not distributed homogeneously in the atmosphere. With decreasing temperatures at higher altitudes, the capacity of air to absorb water vapour decreases and hence the air becomes dryer. The Clausius-Clapeyron equation for the phase transition between liquid and gaseous water describes the non-linear dependence of the saturation vapour pressure and the temperature:

$$\frac{de_s(T)}{dT} = \frac{I_e}{T(v_g - v_l)} \approx \frac{I_e}{Tv_g} = \frac{I_e e_s}{R_v T^2} \quad (2.1)$$

Here  $T$  denotes the temperature,  $e_s$  the saturation vapour pressure over water,  $I_e$  the heat of evaporation,  $v_l$  and  $v_g$  the specific volumes of liquid and gaseous water and  $R_v$  the gas constant of water vapour.

Fig. 2.1 shows balloon-borne laser spectrometer measurements by Durry et al. (2008) of the water vapour mixing ratio with altitude from Aire-sur-l'Adour ( $\sim 43^\circ\text{N}$ ). From the ground to the lower stratosphere at about 15 km altitude, the mixing ratio of water vapour decreases from  $10.000 \mu\text{mol/mol}$  to less than  $5 \mu\text{mol/mol}$ . The highest gradient in the water vapour mixing ratio can be seen in the tropopause region around 10 km. In the stratosphere the water vapour mixing ratio slightly increases again with altitude.

The water vapour budget in the stratosphere is controlled by two mechanisms. The exchange of water vapour between the troposphere and the stratosphere and the chemical generation of water vapour through methane oxidation within the stratosphere. Both of these mechanisms are explained in the subsequent sections.

The stratospheric water vapour budget has not been constant over time. Variations and trends in atmospheric dynamics and in the abundance of atmospheric methane alter the transport and the production of water and hence its budget. This again affects the energy budget of the Earth system and the stratospheric ozone chemistry. Hereinafter, changes of the stratospheric water vapour budget and recent studies of its climate effect are presented.

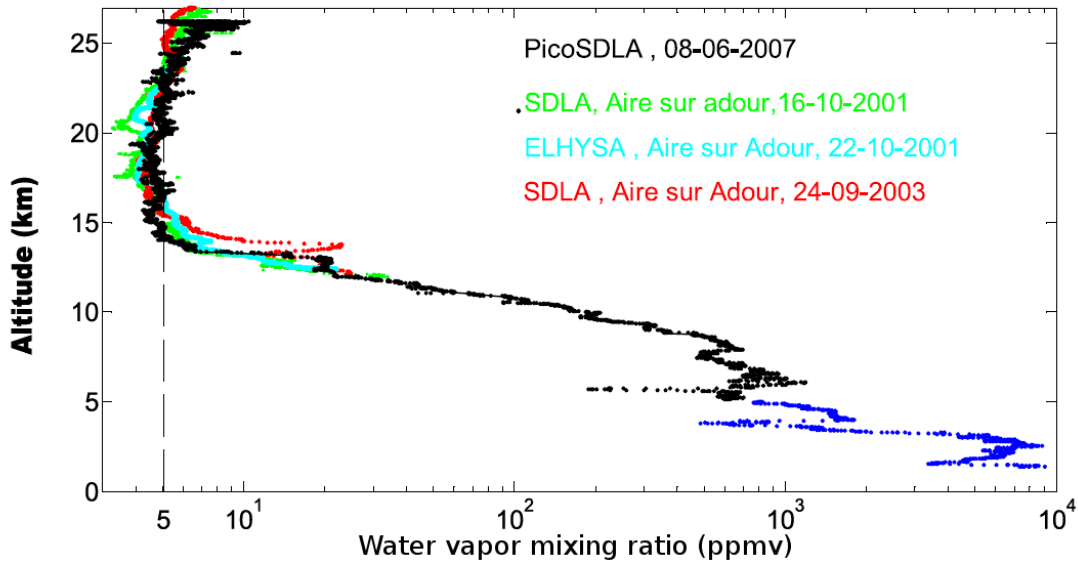


Figure 2.1: In situ vertical mixing ratio profiles of water vapour achieved with the balloon-borne diode laser spectrometer SDLA (Spectromètre à Diodes Laser Accordables) (Durry et al., 2008).

### 2.1.1 Pathways of water vapour into the stratosphere

The dynamical aspects of water vapour exchange between the troposphere and the stratosphere are shown schematically in Fig. 2.2. Most of the transport of water vapour from the troposphere into the stratosphere takes place through the tropical tropopause layer (TTL). Deep-convective clouds penetrate the tropopause and inject water into the stratosphere, partly by overshooting ice crystals. Another exchange mechanism between the troposphere and the stratosphere is meridional transport by eddy motions on isentropic surfaces, which include tropical upper tropospheric troughs and their cutoff lows, as well as their midlatitude counterparts including tropopause folds and blocking anticyclones (Hoskins et al., 1985; Holton et al., 1995). The amount of water vapour which enters the stratosphere dynamically is therefore determined mainly by convective activity, but also by the “cold trap”. This is the coldest point of the troposphere, the boundary of the TTL, which most of the water vapour has to pass to reach the stratosphere. This temperature regulates the dehydration of air on its way through the tropopause (Brewer, 1949; Newell and Gould-Steward, 1981; Danielsen, 1982).

The transport of air, and hence also water vapour, within the stratosphere is determined by the so called Brewer-Dobson circulation (BDC). It is dominated by rising air in the tropical regions, meridional transport to the winter pole and descending motion in the mid- and high-latitudes (Dobson et al., 1946; Brewer, 1949). The poleward transport is explained by tropospheric waves, which propagate up to the stratosphere, and is limited to the winter hemisphere due to its coupling to a westerly wind regime in the stratosphere (Charney and Drazin, 1961). Air masses are “pumped” polewards from the tropics and consequently air



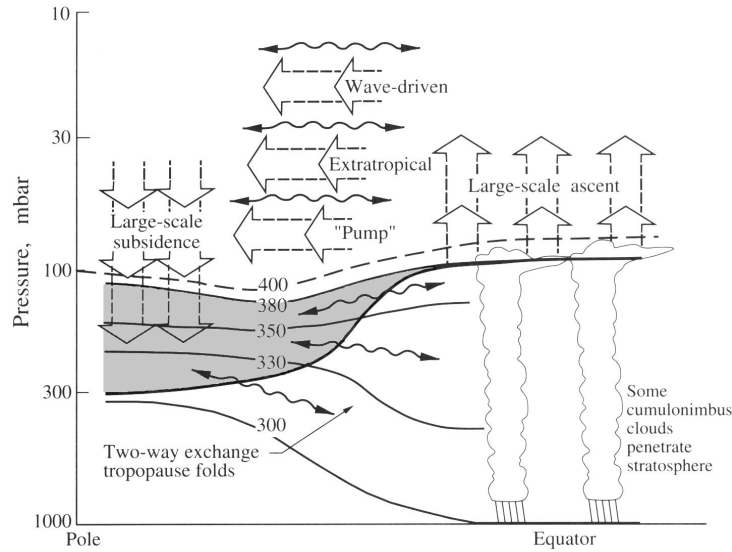


Figure 2.2: Dynamical aspects of stratosphere-troposphere exchange. The tropopause is shown by the thick line, thin lines are surfaces of constant potential temperature. The shaded region is the ‘lowermost stratosphere’, where isentropic exchange by tropopause folding occurs. The wiggly double headed arrows denote meridional transport by eddy motions, not all eddy transports are shown and the arrows are not meant to imply any two-way symmetry. The region above the 380 K surface is the ‘overworld’ in which isentropes lie entirely within the stratosphere. The overworld is dominated by wave-induced forcing (Holton et al., 1995).

must rise in the tropics and sink in the polar regions. This mechanism is called “downward control” or “extratropical pump” and was discovered by Haynes and McIntyre (1987) and Haynes et al. (1991). The tropics, the mid-latitudes and the polar vortex constitute the three sections of the stratosphere with distinct transport barriers between them. Within these sections, isentropic mixing processes generate a roughly homogeneous distribution of trace gases (see Plumb, 2002).

As mentioned above, the TTL, which features dynamical properties of the troposphere and the stratosphere, is of particular interest for being the dominant region for water vapour to enter the stratosphere. Fig. 2.3 shows a schematic of cloud processes and zonal mean circulation of the tropical troposphere and lower stratosphere.

(a) indicates deep convection which has its main outflow region in about 200 hPa, here radiative cooling and hence subsidence takes place (b). Above that region Füglistaler et al. (2009) set the lower bound of the TTL. Another outflow region of tropical convection is the upper troposphere, indicated by (g). Above the black dashed line, which stands for the level of zero net radiative heating (LZRH), positive radiative heating forces the air to further ascend (d) slowly (around 6 months between 15 and 20 km). This is usually coupled with large-scale horizontal transport through cold regions. Within the TTL the formation of thin, partly subvisible cirrus clouds, either as remnants of convective clouds or in situ, can take place (i). If these wide spread cirrus clouds can generate ice crystals large enough

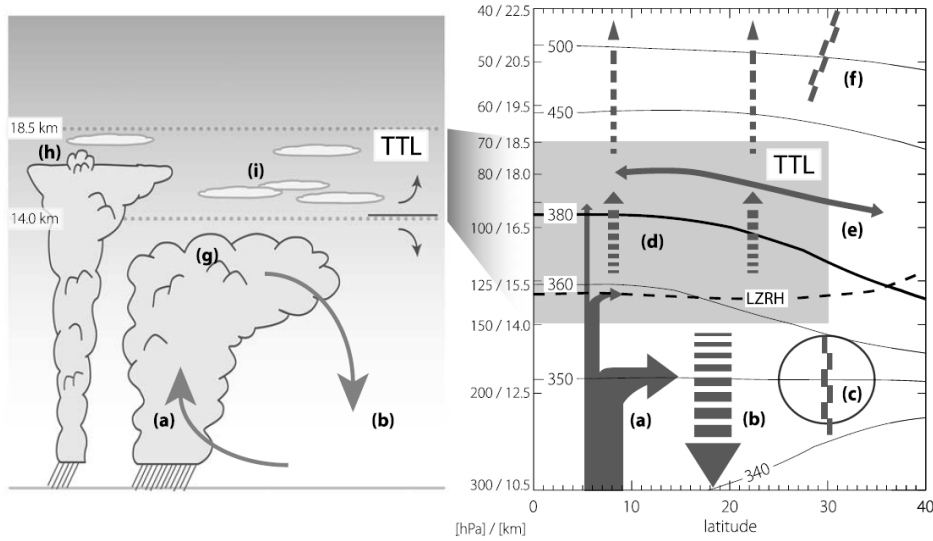


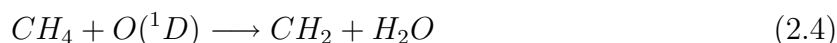
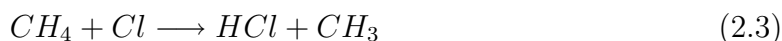
Figure 2.3: Schematic of cloud processes and transport (left) and of zonal mean circulation (right). Arrows indicate circulation, the black dashed line is the clear-sky level of zero net radiative heating (LZRH), and the black solid lines show isentropes (in K) (Füglister et al., 2009).

to gravitationally sediment out of the TTL, very dehydrated air can rise further up into the stratosphere. This is the most accepted mechanism driving dehydration in the TTL and is commonly referred to as the cold trap hypothesis (Holton and Gettelman, 2001; Gettelman et al., 2002b; Füglister et al., 2004).

Some water vapour even rises directly into the stratosphere by a convective core overshooting its level of neutral buoyancy (h). Aircraft and balloon measurements by e.g., Nielsen et al. (2007), Corti et al. (2008) or Khaykin et al. (2009) presented evidence of enhanced water vapour or ice crystals up to several kilometres above the TTL. Convective overshoots have the potential to both, hydrate and dehydrate the lower stratosphere. Adiabatically dried air with extremely low temperatures and water vapour mixing ratios penetrates into the stratosphere through strong convective updrafts. The deposition of water vapour on the ice crystals in the cold updraft dehydrate the air additionally. According to Jensen et al. (2007), however, for this mechanism the air in the TTL has to be initially supersaturated with respect to ice. Moreover, this process requires most of the ice crystals to be large enough to sediment out of the short-lived overshoots. Smaller ice particles may evaporate or sublimate after the convective event having entered the warmer lower stratosphere and hydrate it. The mechanism of dehydration by rapid cooling by e.g., Danielsen (1982), Russell et al. (1993) or Sherwood and Dessler (2000) is confronted with the theory of a net hydrating effect (e.g., Grosvenor et al., 2007; Chaboureaud et al., 2007; Corti et al., 2008; Khaykin et al., 2009). The quantification of the net effect of convective overshooting, as well as the contribution of these infrequent extreme events to the total stratospheric water vapour budget still remain unclear.

### 2.1.2 The chemical generation of water vapour

Some water vapour of the atmosphere is produced in situ through the oxidation of methane (Bates and Nicolet, 1950; Le Texier et al., 1988). Four main reactants are responsible for the chemical production of water, namely the hydroxyl radical (OH), chlorine (Cl), singlet oxygen ( $O(^1D)$ , oxygen atoms at an excited state) and photons ( $h\nu$ ). The four corresponding reactions are (Ravishankara, 1988):



The product HCl of Eq. 2.3 produces water in a follow-up reaction with OH



and the products of Eq. 2.5, which only proceeds with ultraviolet radiation short of 145 nm (Mordaunt et al., 1992), react further with:



Molecular and atomic hydrogen again produce water in reactions with OH and  $HO_2$ :



The major methane loss is its reaction with OH (Eq. 2.2), which takes place in the stratosphere and in the troposphere as well. The reactions with Cl and  $O(^1D)$  only contribute in the stratosphere. Photolysis of methane becomes important in the upper stratosphere and above (Ravishankara, 1988). The production of water through methane oxidation, therefore is strongest at the higher altitudes of the stratosphere and falls off sharply at lower altitudes (Hurst et al., 2011). The in-mixing of older stratospheric air masses with increased water vapour mixing ratios from oxidised methane and to a lesser degree in situ methane production (Füglistaler et al., 2009) is the reason for the slight increase of the water vapour mixing ratio above the tropopause in Fig. 2.1.

Due to an increase of livestock holding, rice cultivation, growing rubbish dumps and melting permafrost, atmospheric methane concentrations have risen during the last decades and centuries. The contribution of methane oxidation to the overall stratospheric water vapour budget is thought to be around 30%. This also agrees with Fig. 2.1 where the water vapour mixing ratio rises from around  $4 \mu\text{mol/mol}$  in the lower to about  $6 \mu\text{mol/mol}$  in the upper stratosphere. Analysing balloon-borne data from the period 1978-2003, Rohs et al. (2006) conceive a contribution of methane oxidation of 25-34% for the increase in stratospheric water vapour. Hurst et al. (2011) calculate that methane oxidation in the stratosphere accounts for at most  $28 \pm 4\%$  in the period from 1980 to 2000,  $14 \pm 4\%$  from 1990 to 2000 and  $25 \pm 5\%$  from 1980 to 2010 of the net stratospheric water vapour increases. The trends and variations of the stratospheric water vapour budget are discussed next.

### 2.1.3 Stratospheric water vapour and its climate effect

For monitoring trends and variations of the stratospheric water vapour budget, long-term observations have been conducted. Rosenlof et al. (2001) have combined ten different data sets, including measurements from rocket-borne (ATMOS - Atmospheric Trace MOlecule Spectroscopy) and satellite-borne (HALOE - Halogen Occultation Experiment) instruments as well as several balloon-borne records, to find an overall increase in stratospheric water vapour of 1% per year for the second half of the 20th century. Fig. 2.4 shows trend analyses of a 30 year record (1980-2010) of stratospheric water vapour measurements over Boulder, Colorado by 336 balloon flights of the NOAA (National Oceanic and Atmospheric Administration) frost point hygrometer at six altitude layers. Over the entire 30-year span, stratospheric water vapour increased by an average of  $1.0 \pm 0.2 \mu\text{mol/mol}$  ( $27 \pm 6\%$ ), including an abrupt decrease starting in mid-2000 followed by a significant increase starting in mid-2005. Water vapour growth during some of the trend periods strengthens with altitude (Hurst et al., 2011).

However, these trends and variations can not be attributed entirely to changes in methane concentrations and tropopause temperatures. Hurst et al. (2011) propose a slowing of the mass flux into the upper tropical stratosphere, which would increase water vapour growth at higher altitudes in the midlatitudes by methane oxidation and combinations of mechanisms in atmospheric dynamics as explanations. Since the root causes of the processes leading to the changes are still not identified, the question remains open.

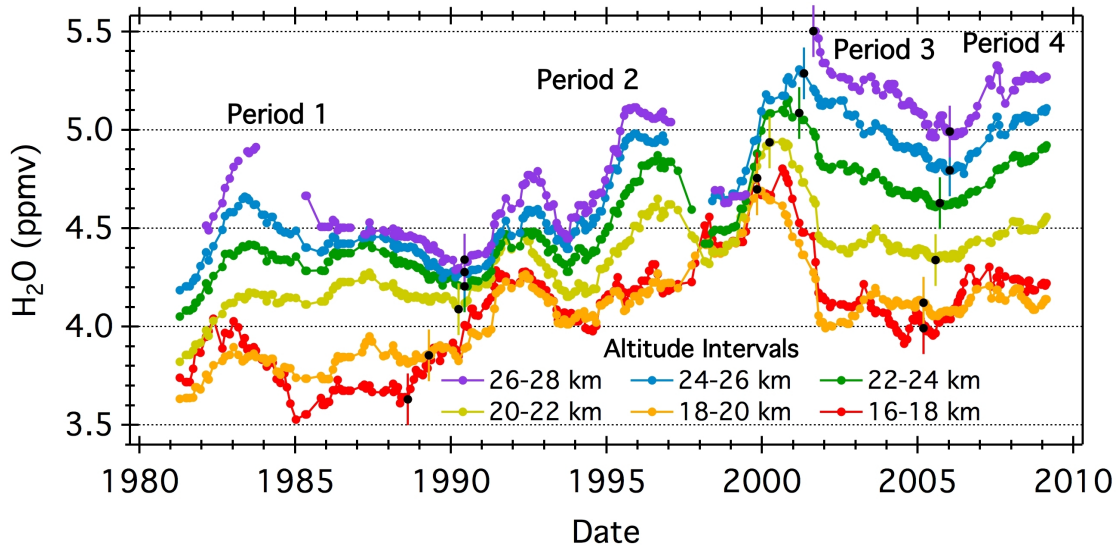


Figure 2.4: Moving averages (Averaging window with a width of  $\pm 1$  year and a threshold of 12 data points) of the 2km water vapour mixing ratio averages at six altitude layers from 1980 to 2010 measured by radiosondes over Boulder. Coloured vertical bars define the four trend periods for each altitude layer (Hurst et al., 2011).

Mote et al. (1996) have discovered an annual variation in the water vapour mixing ratio in the tropical stratosphere. In the lower stratosphere, relatively dry air in boreal winter and spring alternates with moist air in summer and autumn, corresponding with cold tropopause temperatures in winter and warm temperatures in summer. As the air enters the rising branch of the BDC in the tropical stratosphere, it is advected upwards, conserving its signature in water vapour mixing ratio. Imaging a recorded signal on an upward moving magnetic tape, Mote et al. (1996) called this mechanism the stratospheric "tape recorder".

Fig. 2.5 shows water vapour mixing ratios measured by the HALOE instrument on the Upper Atmosphere Research Satellite (UARS) from 1993 to 2005 averaged from 5°S to 5°N, which clearly features the described tape recorder signal. From the lower to the upper stratosphere, where the mixing ratio anomalies smear out, the signal needs about 1.2 years. From satellite measurements, Mote et al. (1998) derived a vertical advection velocity with a minimum of about  $0.2 \text{ mms}^{-1}$  near 20 km.

The high water vapour mixing ratios in the TTL during boreal summer are associated with enhanced convective events linked with the Indian/Southeast Asian and North American Monsoon circulations (Gettelman et al., 2002a). Seasonal and QBO-related (Niwa et al., 2003) variability affects the amplitude of the tape recorder signal, as well as its vertical velocity. A noticeable feature in Fig. 2.5 is the much lower water vapour mixing ratios after the year 2000, which was already seen in Fig. 2.4.

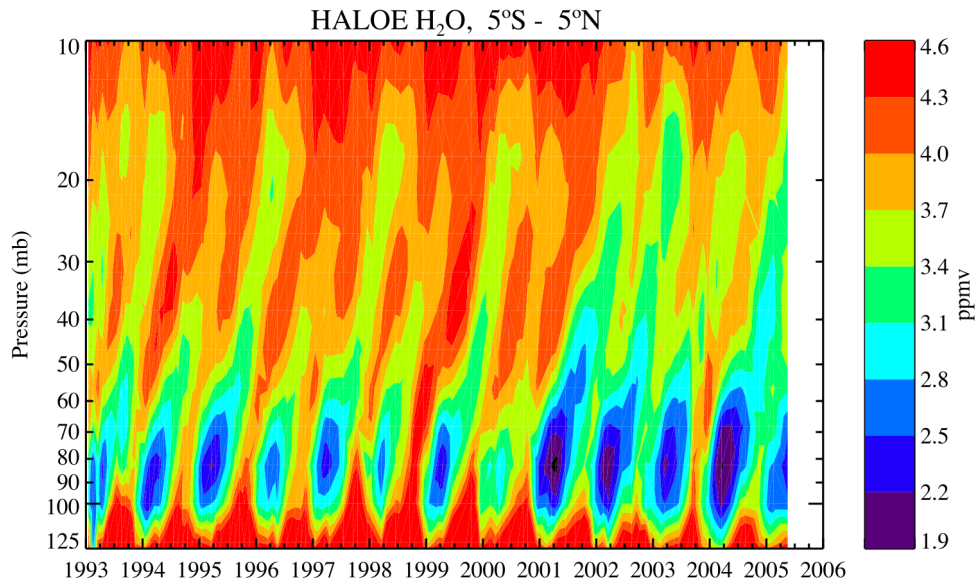


Figure 2.5: Stratospheric tropical (5°S-5°N) water vapour tape recorder, plotted versus time from 1993 to 2005 from HALOE observations (Rosenlof and Reid, 2008).

Water vapour is the primary greenhouse gas. Like carbon dioxide, methane, halocarbons, nitrous oxide and others it absorbs and emits infrared radiation. Rising greenhouse gas concentrations in the atmosphere increase the amount of absorbed infrared radiation

in the lower atmosphere and thereby warm the troposphere. The stratosphere albeit cools, firstly, because less longwave radiation from the surface reaches the upper atmosphere and secondly, higher stratospheric greenhouse gas concentrations effectively emit more radiation. The latter reason requires that the emissivity in a certain level and spectral band can still be increased (see Clough et al., 1992; Clough and Iacono, 1995). Stratospheric water vapour plays an important role in the radiative heat budget of the stratosphere (Forster and Shine, 1999). The typical stratospheric temperature response to a uniform increase of the water vapour mixing ratio is characterised by maximum cooling in the lowermost extratropical stratosphere (e.g. Forster and Shine, 2002; Maycock et al., 2013). The stratospheric equilibrium temperature response to changes in stratospheric water vapour, however, shows large disparities in different models (see e.g. Oinas et al., 2001; Zhong and Haigh, 2003; Maycock and Shine, 2012).

From the 30 year radiosonde data record of Boulder and two additional satellite data sets (UARS Haloe and SAGE II) Solomon et al. (2010) calculate a radiative forcing of roughly  $+0.25 \text{ Wm}^{-2}$  of stratospheric water vapour for the period between 1980 and 2000 and about  $-0.1 \text{ Wm}^{-2}$  after the year 2000 with a line-by-line radiative transfer model. The quantification of this radiative forcing on global temperature change since 1980 using a climate model, yields a contribution of 30%. Moreover, it plays a determining part in the flattening of the temperature increase since 2000 (see Fig. 2.6).

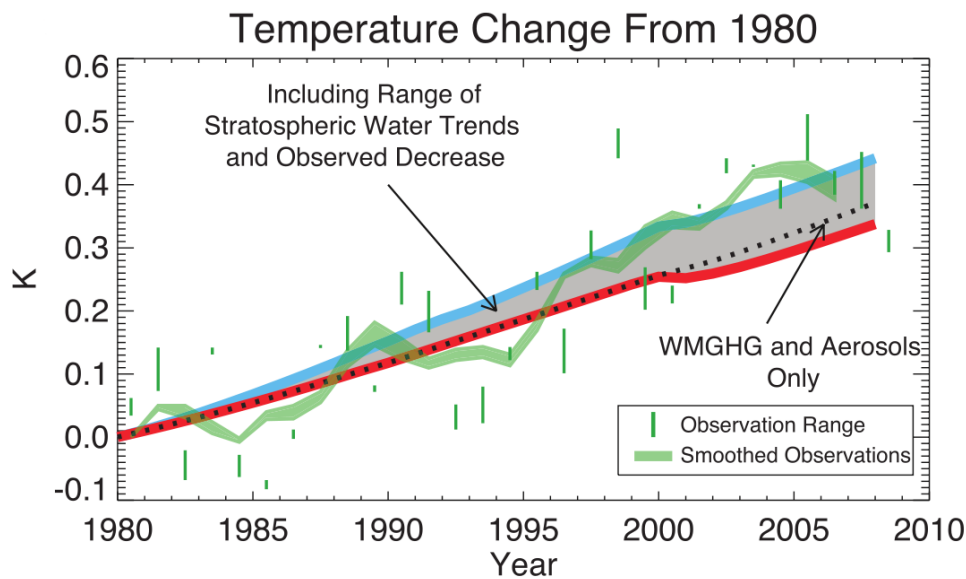


Figure 2.6: Measured and modelled temperature changes relative to 1980. The green markers indicate the range across three data sets in each year. The green shaded line shows the range of the 5-year running mean of the three data sets. The black dotted line shows a climate model simulation with the historical trend of greenhouse gases, the red line illustrates a simulation with the additional stratospheric water vapour amount of the last eight years and the blue line includes the overall data record of stratospheric water vapour (Solomon et al., 2010).

Another climate effect of a change in the stratospheric water vapour budget is its impact on stratospheric chemistry, in particular ozone destruction. Two chemical mechanisms are responsible for this. Water vapour as the primary source for  $\text{HO}_X$ -radicals and chemical processes on polar stratospheric clouds (PSCs), (Solomon et al., 1986).

The  $\text{HO}_X$ -radicals OH and  $\text{HO}_2$  are formed mainly by reactions of water with  $\text{O}(^1\text{D})$  and by photolysis. The reactions



sum to the equivalent of the reaction



and are designated as the  $\text{HO}_X$  catalytic chain (Bates and Nicolet, 1950).

PSCs develop at very low temperatures, which occur in the winter stratosphere. The theory of the processes that lead to PSC-development are illustrated in Zellner (1999). Heterogeneous reactions on the surfaces of PSCs evoke a denitrification of the gaseous phase in the polar stratosphere and shifts the ratio between nitrous oxides and chlorine compounds strongly to the latter. The low intensities of the radiation at the end of the polar night suffice to photolyse the chlorine compounds and the hereby forming chlorine radicals cause effective catalytic ozone depletion. Processes like stratospheric cooling or the increase in stratospheric water vapour, which support the formation of PSCs, hence increase the depletion of stratospheric ozone. A more detailed description of the ozone depleting mechanisms is given in Stenke (2005) or WMO (2006). Decreasing mixing ratios of stratospheric ozone due to increased stratospheric water vapour has been investigated in numerous studies (e.g., Dvortsov and Solomon, 2001; Shindell, 2001). The model study of Stenke and Grewe (2005) shows that 10% of the global total ozone decline can be explained by the water vapour increase in the 40 year time period 1960 to 1999.

## 2.2 Water isotopologues in the Earth's hydrological cycle

Chemical elements consist of several atoms of different mass, called isotopes (greek: isos = equal, topos = location). Isotopologues are the respective various molecules.  $^1\text{H}^1\text{H}^{16}\text{O}$  is the most abundant form of water and therefore commonly called 'normal' water (referred to as  $\text{H}_2\text{O}$  hereafter). Water isotopologues can be divided into radioactive and stable isotopologues. Radioactive water isotopologues contain at least one Tritium atom (T or  $^3\text{H}$ ), which has a core consisting of one proton and two neutrons. HTO and TTO are unstable, very rare and therefore not suitable as a trace gas for climate studies. Stable water isotopologues can differ in the element of hydrogen or oxygen, hence several combinations of isotopologues exist. Fig. 2.7 shows the three stable water isotopologues, which are used in this work:  $\text{H}_2^{16}\text{O}$ ,  $\text{H}_2^{18}\text{O}$  and  $\text{HD}^{16}\text{O}$  (deuterated water). These particular isotopologues are selected because comprehensive observations are available and their physical and chemical

properties are well-known. The D in HDO stands for Deuterium, which is  $^2\text{H}$  (first discovered by Urey and Teal, 1935), a hydrogen atom with a core consisting of one proton and one neutron, unlike the common hydrogen, which has one proton only. The  $^{18}\text{O}$  atom has two extra neutrons compared to the 'normal' oxygen atom  $^{16}\text{O}$

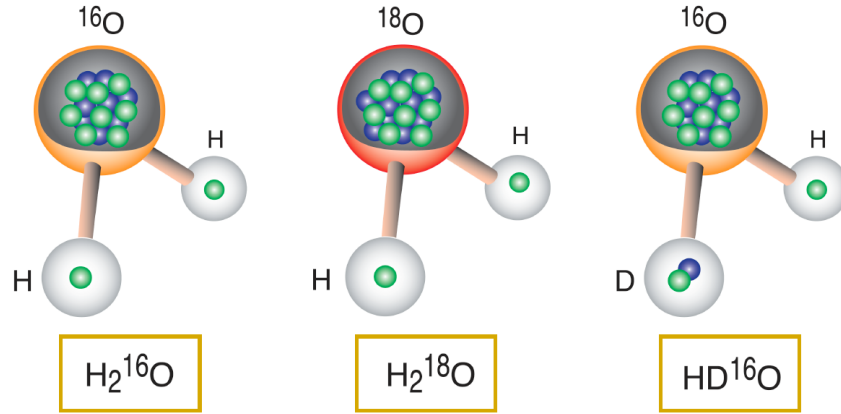


Figure 2.7: Cartoon of the composition of the stable water isotopologues  $\text{H}_2^{16}\text{O}$ ,  $\text{H}_2^{18}\text{O}$  and  $\text{HD}^{16}\text{O}$ , from M. Werner (personal communication, 2013).

The following sections give an overview about the different forms and properties of stable water isotopologues and the physical and chemical isotope fractionation processes. Moreover, the characteristics of water isotopologues in the hydrological cycle and their role as tracers for studies of atmospheric processes is explained.

### 2.2.1 Forms, abundances and notation

Tab. 2.1 gives an overview of most of the stable water isotopologues, showing their chemical compositions, abundances and molecular masses. The data was compiled by the International Atomic Energy Agency (see IAEA, 2009) who issue the standard for isotopologues in water called VSMOW (Vienna Standard Mean Ocean Water).

Variations of the rates of stable water isotopologues in certain compounds can provide information about processes in the hydrological cycle. Owing to the fact that the differences between natural isotope samples are usually very small, the conventional expression for isotopic abundances became the so called  $\delta$  notation. The  $\delta$  of a certain isotope expresses its abundance relative to the standard, for water isotopologues the VSMOW, and was first used by Urey (1948). The equation

$$\delta_X(Y)(\text{‰}) = \frac{R_{\text{sample}} - R_{\text{std}}}{R_{\text{std}}} \cdot 1000 = \left( \frac{R_{\text{sample}}}{R_{\text{std}}} - 1 \right) \cdot 1000 \quad (2.14)$$

shows the calculation of the  $\delta$  value for a given isotope X, where  $R_{\text{sample}} = [\text{X}]/[\text{Y}]$  denotes the ratio of the rare isotope (X) and the 'normal' isotope (Y) of the sample and  $R_{\text{std}}$  the according ratio of the standard. It is multiplied by 1000 to retrieve the  $\delta$  value in permil.  $\delta\text{D}(\text{H}_2\text{O}) = 0\text{‰}$  would therefore be exactly the ratio of VSMOW ( $R_{\text{std}} = R_{\text{VSMOW}} =$



Isotopologue	Abundance (in %)	Molecular mass (in g/mol)
H <sub>2</sub> <sup>16</sup> O	99.7317	18.01056469
H <sub>2</sub> <sup>17</sup> O	0.0372	19.01478156
H <sub>2</sub> <sup>18</sup> O	0.199983	20.0148105
HD <sup>16</sup> O	0.031069	19.01684143
HD <sup>17</sup> O	0.0000116	20.02105831
HD <sup>18</sup> O	0.0000623	21.0210872
D <sub>2</sub> <sup>16</sup> O	0.0000026	20.02311818

Table 2.1: Stable water isotopologues: Molecules, abundances and molecular weights according to VSMOW (IAEA, 2009).

$(155.76 \pm 0.05) \cdot 10^{-6}$ , Hagemann et al., 1970). Samples with negative  $\delta D$  values are depleted in Deuterium or isotopically lighter with respect to the standard and positive  $\delta$  values show an enrichment of the rare isotopologue.

## 2.2.2 Isotope fractionation

Due to their variations in mass and hence in zero-point energies, water isotopologues differ in their vapour pressures and binding energies. Consequently the lighter isotopologues tend to evaporate/sublimate or chemically react faster than the heavy ones and hence enrich in the more diffusive phase or in the reaction product (Mook, 2000a). This process is called 'isotope fractionation'. It has to be distinguished between isotope fractionation processes in open and in closed systems. For a closed system it is assumed that the precursor and the product are in isotopic equilibrium during the entire process. This is thus called 'equilibrium fractionation'. An open system in contrast assumes an equilibrium between product and precursor only for the just formed fraction of the product. In other words, the product is extracted from the system instantaneously, these processes are called 'kinetic fractionation'. Kinetic exceeds equilibrium isotope fractionation vastly in strength and while the latter is reversible, kinetic fractionation is a one-way process. The two fractionation theories are explained next, additionally the simple Rayleigh fractionation model is introduced.

### 2.2.2.1 Equilibrium fractionation

Equilibrium isotope fractionation is proportional to  $\Delta m/m$ , where  $\Delta m$  is the mass difference between the involved isotopes and  $m$  usually denotes the mass of the more abundant isotope. Moreover, the strength of the fractionation depends on conditions like the pressure, the humidity and especially the temperature during the phase transition or the chemical reaction. The equation,

$$R_{pre} = \alpha(T) \cdot R_{pro} \quad (2.15)$$

where  $R_{pre}$  and  $R_{pro}$  denote the isotopic compositions of precursor and product and  $\alpha$  the mainly temperature dependent fractionation factor, describes the equilibrium isotope

fractionation. The equilibrium fractionation factors  $\alpha$  for HDO and  $\text{H}_2^{18}\text{O}$  for the phase transitions of water between vapour (V) and liquid (L) or ice (I) have been measured by Majoube (1971a,b) and are given by:

$$\text{H}_2^{18}\text{O} : \ln(\alpha_{VL}) = \frac{1.137 \cdot 10^3 \text{ K}^2}{T^2} - \frac{0.4156 \text{ K}}{T} - 2.0667 \cdot 10^{-3} \quad (2.16)$$

$$\ln(\alpha_{VI}) = \frac{11.839 \text{ K}}{T} - 28.224 \cdot 10^{-3} \quad (2.17)$$

$$\text{HDO} : \ln(\alpha_{VL}) = \frac{24.844 \cdot 10^3 \text{ K}^2}{T^2} - \frac{76.248 \text{ K}}{T} + 52.612 \cdot 10^{-3} \quad (2.18)$$

$$\ln(\alpha_{VI}) = \frac{16.288 \cdot 10^3 \text{ K}^2}{T^2} - 93.4 \cdot 10^{-3}. \quad (2.19)$$

Here,  $T$  denotes the temperature in Kelvin. These equations are best-approximates for data between  $-40^\circ\text{C}$  and  $100^\circ\text{C}$ . The lower the temperature, the stronger is the isotope fractionation during, for example, evaporation, i.e. the isotopically heavier is the enriched residual liquid water compared to the depleted water vapour after the process.

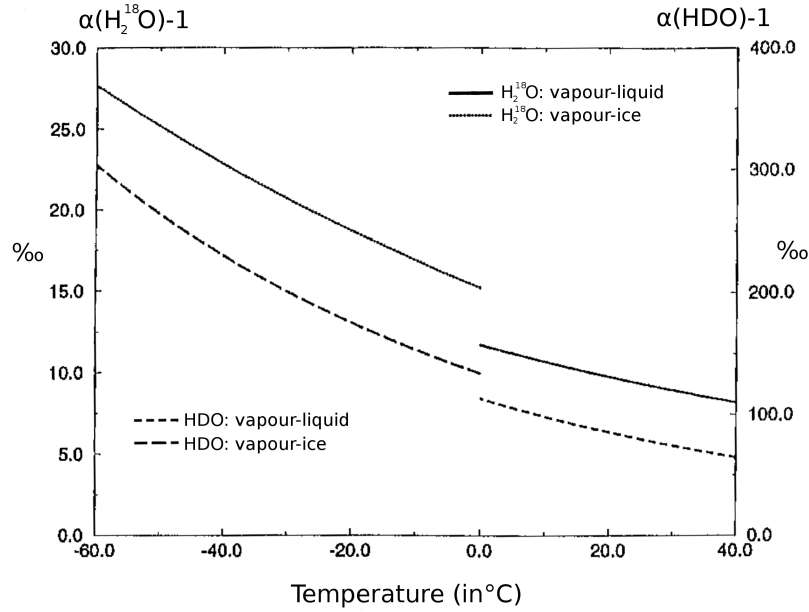


Figure 2.8: Temperature dependency of the fractionation factors (shown as:  $\epsilon = (\alpha - 1) \cdot 1000$ ) in permil for  $\text{H}_2^{18}\text{O}$  (left scale) and HDO (right scale) for the transitions vapour-liquid and vapour-ice (Hoffmann, 1995).

Fig. 2.8 shows the four fractionation factors (given as:  $\epsilon = (\alpha - 1) \cdot 1000$ ) in permil. Obviously, equilibrium fractionation is much stronger in HDO compared to  $\text{H}_2^{18}\text{O}$ . A comparison of the relative strength of the fractionation due to the isotopologues' differences in mass (HDO:  $\frac{\Delta m}{m} = \frac{1}{18}$ ,  $\text{H}_2^{18}\text{O}$ :  $\frac{\Delta m}{m} = \frac{2}{18}$ ), however, suggests the opposite. The reason is the disturbed symmetry of the  $^1\text{H}^2\text{H}^{16}\text{O}$  molecule due to the heavier deuterium (see also

Fig. 2.7). This allows kinetic energy to convert into rotational energy, which is not possible for the symmetric  $^1\text{H}_2^{18}\text{O}$  and  $^1\text{H}_2^{16}\text{O}$  isotopologues. As a result, HDO fractionates about eight times stronger than  $\text{H}_2^{18}\text{O}$  (Hoffmann, 1995).

### 2.2.2.2 Kinetic fractionation

The kinetic fractionation factor is influenced strongly by the difference of the isotopes' diffusivities. With the temperature (T) and mass (m) dependent mean thermal velocity  $v = \sqrt{\frac{8k_B T}{\pi m}}$ , where  $k_B$  denotes the Boltzmann constant and the mean free path length  $l$ , the diffusion constant can be approximated with

$$D \approx \frac{1}{3} \cdot v \cdot l. \quad (2.20)$$

According to Merlivat (1978), the molecular diffusion coefficients of  $\text{H}_2^{18}\text{O}$  and HDO relative to  $\text{H}_2\text{O}$  in vapour are:

$$\frac{D(\text{H}_2^{18}\text{O})}{D(\text{H}_2\text{O})} = 0.9723 \pm 0.0007 \quad (2.21)$$

$$\frac{D(\text{HDO})}{D(\text{H}_2\text{O})} = 0.9755 \pm 0.0009 \quad (2.22)$$

The quantitative description of the kinetic fraction factor emerged from a molecular evaporation model of Brutsaert (1975a,b) and was conducted by Merlivat and Jouzel (1979). The strength of the kinetic fractionation is proportional to the undersaturation of the atmosphere (the relative humidity  $h$ ) and can be described with (see also Hoffmann et al., 1998):

$$1 + \delta_E = (1 - k_f) \frac{\frac{1}{\alpha(T)} - h(1 + \delta_{v0})}{1 - h} \quad (2.23)$$

Here  $\delta_E$  denotes the  $\delta$  value of the evaporation flux,  $\delta_{v0}$  the  $\delta$  value of the vapour above the ocean surface,  $\alpha$  the equilibrium fractionation factor and  $k_f$  the kinetic fractionation factor.

During evaporation from surface waters, which is the most important kinetic fractionation process in the atmosphere, the kinetic fractionation factor also depends on the horizontal wind regime at the site of evaporation. The wind speed determines the deviation from the equilibrium of the process. The following equations by Brutsaert (1975b) (see also Hoffmann, 1995) approximate this relation:

$$k = \begin{cases} 0.006 & : \text{H}_2^{18}\text{O} \\ 0.00528 & : \text{HDO} \end{cases}, |v_h| < 7 \frac{m}{s} \quad (2.24)$$

$$k = \begin{cases} 2.85 \cdot 10^{-5} + 8.2 \cdot 10^{-5} \cdot |v_h| & : \text{H}_2^{18}\text{O} \\ 2.508 \cdot 10^{-5} + 7.216 \cdot 10^{-5} \cdot |v_h| & : \text{HDO} \end{cases}, |v_h| > 7 \frac{m}{s} \quad (2.25)$$

Another kinetic fractionation effect becomes important for ice formation in oversaturated air at low temperatures, for instance in clouds. Unlike for condensation, where it is assumed, that the condensate stays in isotopic equilibrium during the process, due to the low diffusivities of the isotopologues in ice ( $D \sim 10^{-14} m^2 s^{-1}$  Kuhn and Thürkauf, 1958) an instantaneous extraction of the condensate is specified for ice crystal formation. The isotope effect for diffusive formation of ice crystals in oversaturated environments is described with an effective fractionation factor  $\alpha_{eff}$  (Jouzel and Merlivat, 1984):

$$\alpha_{eff} = \alpha_{kin} \cdot \alpha_{eq} \quad (2.26)$$

$$\alpha_{kin} = \frac{S}{\alpha_{eq} \frac{D}{\hat{D}}(S-1) + 1}. \quad (2.27)$$

$D/\hat{D}$  stands for the relation between the diffusivities of the rare isotopologue and  $H_2O$  (see Eq. 2.21 and Eq. 2.22) and  $S$  for the oversaturation of the humidity above the ice vapour pressure. Since the oversaturation is difficult to determine, Jouzel and Merlivat (1984) developed a temperature-dependent numeric parametrisation for  $S$ :  $S = 1 - 0.003 \cdot T_{cond}$  ( $T_{cond}$  is the condensation temperature in  $^{\circ}C$ ), (see also Hoffmann et al., 1998). The constants of this parameterisation are still unknown and have been modified several times for different model studies, more details will be given in the model description in Sect. 3.3.

Kinetic fractionation occurs during non-equilibrium conditions. This implies the assumption that the product is removed from the system instantaneously or can not reequilibrate with the reservoir. Thus in this theory, only the just formed fraction of the product is in isotopic equilibrium with the reservoir, which leads to an infinitesimal approach to describe kinetic isotope fractionation. The so called Rayleigh equations describe such processes. These and the hereon based simple Rayleigh fractionation model are presented next.

### 2.2.2.3 The Rayleigh model

A simple box model of a reservoir with one sink can be derived to describe the isotopic change of a substance during its destruction accompanied by kinetic isotope fractionation. It is presented in Fig. 2.9. Here,  $N$  is the total number of abundant isotopic molecules,  $R$  the isotopic ratio and  $\alpha$  the constant kinetic fractionation factor.

The isotopic ratio of the remaining fraction of the reservoir after an infinitesimal amount of molecules  $dN$  has been removed, including fractionation, is determined by the mass balance:

$$RN = (R - dR)(N - dN) + \alpha R \cdot dN \quad (2.28)$$

Neglecting the products of differentials, this results in the differential equation

$$\frac{dR}{R} = (\alpha - 1) \frac{dN}{N}. \quad (2.29)$$

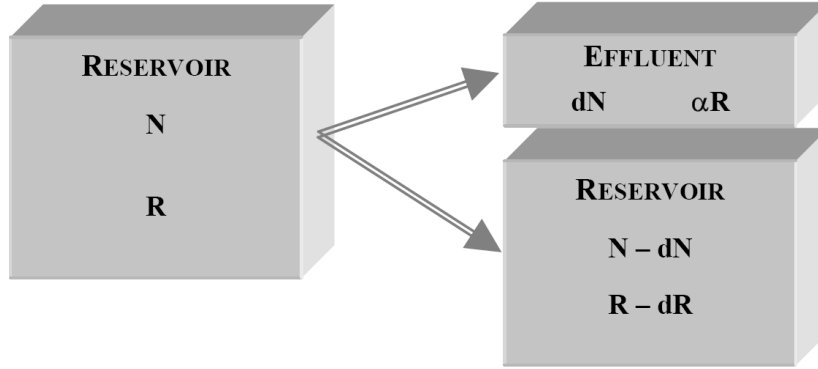


Figure 2.9: Simple box model approach of the Rayleigh model, (Mook, 2000b).

Applying the boundary condition that at the beginning of the process  $R = R_0$  and  $N = N_0$ , the solution is

$$R = R_0 \left( \frac{N}{N_0} \right)^{\alpha-1}, \quad (2.30)$$

or in  $\delta$  notation with respect to VSMOW:

$$\delta = (1 + \delta_0) \left( \frac{N}{N_0} \right)^{\alpha-1} - 1. \quad (2.31)$$

Rayleigh processes obey this relation, which is visualised in Fig. 2.10. An example for this simple process is the increase of  $[HDO]/[H_2O]$  of a confined water body by evaporation with  $\alpha < 1$  (Mook, 2000a,b).

The Rayleigh model is a reasonable first order approach to determine the isotopic ratios of water vapour in the atmosphere. Cloud processes, however, are far more precarious and extensive than this simple model can capture. The temperature differences between the boundary layer and the TTL, the numerous condensation, evaporation as well as sublimation and freezing processes taking place within one cloud and also the vertical and horizontal in-mixing of air can change the isotopic ratios vastly. At any point, only the differential equation Eq. 2.28 is valid and has to be evaluated numerically and also the other processes have to be captured to numerically describe water isotopologues in the hydrological cycle

### 2.2.3 Physical isotope processes in the hydrological cycle

Physical isotope processes of water include transport of water and phase changes between vapour, liquid and ice. As water and its isotopologues are undergoing the particular processes along the global hydrological cycle, certain isotope effects take place.

Starting with 'vapour transport' horizontal and vertical mixing through up- and down-drafts, diffusion or advection can change the isotopic composition of air. There is no isotope

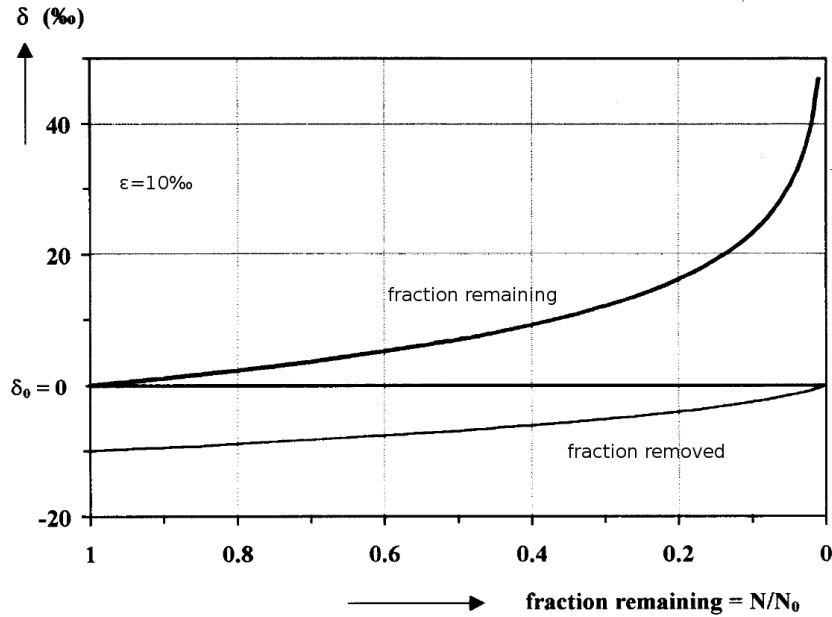


Figure 2.10: The enrichment of a rare heavy isotope in the reservoir and in the formed compound by the Rayleigh process as a function of the fraction remaining in the reservoir. ( $\epsilon = (\alpha - 1) \cdot 1000$  denotes the fractionation coefficient), (Mook, 2000a).

fractionation connected with transport or mixing, but the distinct masses of the respective isotopologues lead to a difference in transport velocities and thereby can change isotopic ratios by mixing.

As mentioned above, a number of isotope effects take place in clouds. From the formation of clouds to precipitation or dissipation, water evaporates, condensates, (de)sublimates, melts and freezes several times. Most of these processes are linked with isotope effects. For condensation and evaporation of water in clouds, a closed system or equilibrium fractionation (see Sect. 2.2.2.1) is assumed. An open system is used for desublimation or deposition of ice from the gas phase (see Eq. 2.27). Due to the low diffusivities of the isotopologues in ice, no fractionation is assumed for melting and sublimation of cloud-ice. During freezing of water, isotopic effects occur in a closed system (Souchez and Jouzel, 1984) and there is also evidence of a kinetic effect (Souchez et al., 2000). However, since the differences of the diffusion constants of water isotopologues in liquid water are much lower than in vapour, these effects are neglected in the present work. There is no isotope fractionation taking place during coalescence and conversion within clouds.

Kinetic isotope fractionation also occurs during the evaporation of waterdrops falling through an undersaturated atmosphere below the cloud. According to Stewart (1975), a similar approach to Eq. 2.27 can be taken for this process, with an  $\alpha_{eff}$  describing the

isotope ratio between the waterdrop and the surrounding vapour (Hoffmann, 1995):

$$\alpha_{eff} = \alpha_{kin} \cdot \alpha_{eq} = \frac{h \cdot \alpha_{eq}}{1 - \alpha_{eq} \cdot \left(\frac{D}{\hat{D}}\right)^n (1 - h)} \quad (2.32)$$

The non-equilibrium is hereby described by the relative humidity  $h$  below the cloud base. The exponent  $n$  was estimated to  $n = 0.58$  (see Stewart, 1975). However, the ratio  $\alpha_{eff}$  does not adjust instantaneously. The adjustment time crucially depends on the size of the waterdrop. In the model, this has to be parameterised by re-equilibrating only a part of the drop. The numeric description is given in Sect. 3.3.5 (see also Jouzel et al., 1987; Hoffmann et al., 1998). For snow and hail in contrast, this isotopic exchange with the ambient air does not occur, which leads to stronger isotopic depletion for solid precipitation (Jouzel and Merlivat, 1984).

Fractionation takes place during the formation of dew and rime on land too. Similar to condensation and desublimation in clouds, a closed system is assumed for the description of dew and an open system for rime formation.

As mentioned above, kinetic fractionation takes place during evaporation of water from surface reservoirs like lakes and oceans. While the isotopic composition of lakes can change seasonally or through rain showers, due to their huge reservoir the isotope ratio of the oceans can be assumed to be constant over time, however, with spatial variations. The isotopic composition of the evaporative flux depends on the sea surface temperature, the relative humidity and also the  $\delta$  values of the local atmospheric vapour and ocean water (see Eq. 2.23). Moreover, the kinetic part of the fractionation depends on the horizontal wind speed (Eq. 2.24 and Eq. 2.25).

As precipitation reaches the ground over land, many processes happen that can modify the isotopic composition of the water. These processes depend on the nature of the terrain and on the characteristics of the rain, such as its amount, duration, intensity and also on the intermittency of the soil (Gat, 1996).

A part of the precipitation is intercepted on the canopy of the vegetation. Some of the intercepted water evaporates facing fractionation processes. The isotopically enriched residual can fall further to the ground through wind or another rainshower flushing it down. Analyses of this process, however, show that it has only a minor effect, being overshadowed by the isotopic signature of the rainwater (e.g. Dewalle and Swistock, 1994).

If the holdup capacity of a surface is exceeded by the amount of water, this water appears as surface runoff. Apart from the evaporation of the top layers of the runoff and mixing, no mechanisms change the isotopic composition during runoff. The same applies for the groundwater flow and for water infiltrating into the soil. The holdup in the soil column and the transport through it does not, in itself, affect the isotopic composition of the infiltrating waters. Due to the differences in the isotopic composition of the respective rainshowers, the  $\delta$  values of the surface runoff and of soilwaters depend on the amount of water in the soil, the time between the rainshowers, plant cover, the composition and permeability of the soil and the topography (Gat, 1996). Stable water isotopologues have thus helped to explain the formation of surface runoff (see e.g. Fritz et al., 1976).

Plants take up soilwater through their roots, essentially unfractionated. Fractionation takes place when the water evaporates from the leaves of the plants. The water in the leaves is therefore isotopically enriched compared to the water in the rest of the plant. According to White (1989), however, in steady-state conditions which can already be approximated after a couple of hours for this process, the transpired water from plants does not show significant differences in its isotopic composition from the water taken up from the soil.

Due to the limitations of the processes in the soil in the here used EMAC model, most of these effects are neglected in the present study. The description of the implementation of the isotopologues in the surface reservoirs is given in Sect. 3.3.2 and Sect. 3.3.3.

### 2.2.4 Chemical isotope fractionation in methane-oxidation

Isotope fractionation also takes place during chemical reactions due to the differences in zero-point energies of the respective isotopes. The chemical reactions concerning water vapour are the methane oxidation reactions, which were discussed in Sect. 2.1.2. Analogue to Eq. 2.2 to Eq. 2.10 deuterated water is formed through the oxidation of  $\text{CH}_3\text{D}$ , the most abundant deuterium isotopologue of methane containing one deuterium atom instead of the fourth hydrogen. The lifetime of  $\text{CH}_3\text{D}$  depends on the reaction rates and the fractionation factors linked with the four known reactants ( $\text{OH}$ ,  $\text{O}(^1\text{D})$ ,  $\text{Cl}$ ,  $h\nu$ ), it varies vertically, horizontally and temporally. In the stratosphere the lifetime of  $\text{CH}_3\text{D}$  is about 1.2 times longer than of  $\text{CH}_4$  (Irion et al., 1996). Since the methane sink reactions are irreversible processes, kinetic isotope fractionation applies here and the Rayleigh equations can be used. The coefficients for the mass-dependent kinetic isotope effects (KIE) for the reactions of  $\text{CH}_3\text{D}$  with  $\text{OH}$ ,  $\text{O}(^1\text{D})$  and  $\text{Cl}$  have been determined in elaborate laboratory measurements by Saueressig et al. (1996) and Saueressig et al. (2001). They are partly temperature ( $T$ ) dependent and can be described with the function  $\text{KIE}(T) = A \cdot \exp(B/T)$ . The values for  $A$  and  $B$  and their temperature ranges are given in Tab. 2.2 (see also Röckmann et al., 2011).

Reactant	$T$	$A$	$B$
$\text{OH}$		1.097	$49 \pm 22$
$\text{O}(^1\text{D})$	224-295	1.066	0
$\text{Cl}$	223-295	1.278	$51.31 \pm 19.1$

Table 2.2: Temperature dependent kinetic isotope fractionation coefficients for the reaction with  $\text{CH}_3\text{D}$  for the given temperature ( $T$  in K) ranges. The kinetic isotope effect is determined by  $\text{KIE}(T) = A \cdot \exp(B/T)$  (Röckmann et al., 2011).

The absorption cross-section of  $\text{CH}_3\text{D}$  is shifted 0.9 nm blueward (Nair et al., 2005) relative to  $\text{CH}_4$ . For the photodissociation of  $\text{CH}_3\text{D}$ , this results in a fractionation factor of 0.995 in the atmosphere of Mars (Nixon et al., 2012). Since the photodissociation characteristics of methane do not differ from one planet of the solar system to another, this also seems like a reasonable approach for the Earth’s atmosphere.



Analogue to Eq. 2.30 the Rayleigh equation

$$R = R_0 \left( \frac{N}{N_0} \right)^{\frac{1}{\text{KIE}} - 1} \quad (2.33)$$

describes the fractionation by chemical reactions with the inverse of the KIE (Fritz and Fontes, 1980).

As can be seen in Eq. 2.2 to Eq. 2.10, the sink reactions of methane, however, do not necessarily directly produce water. The intermediate products (e.g.  $\text{CH}_3$ ) produce water through reactions, which are mainly controlled by molecular hydrogen. Molecular hydrogen is distributed almost equally with altitude and time throughout the stratosphere. Hence the intermediate reactions from  $\text{CH}_4$ , via  $\text{H}_2$  to  $\text{H}_2\text{O}$  have practically no effect on the altitude dependence of the water production by methane oxidation. As can be seen from Röckmann et al. (2003),  $\delta\text{D}(\text{H}_2)$ , in contrast, is increasing with altitude in the lower stratosphere. This is due to fractionation effects during the intermediate reactions from  $\text{CH}_3\text{D}$  via HD (an isotopologue of  $\text{H}_2$ ) to HDO (see i.e. Rhee et al., 2006). The isotope exchange reaction rate coefficients and the kinetic isotope fractionation factors for these reactions, however, are poorly quantified (Zahn et al., 2006).

### 2.2.5 Atmospheric processes derived from isotope ratios in precipitation

The development of the mass spectrometer for isotope analysis by Nier (1947), which first allowed precise and relatively easy measurements of isotope concentrations in water, started the utilisation of water isotopologues in geoscience. With data from the IAEA-WMO measuring survey GNIP (Global Network for Isotopes in Precipitation, further details are given in Sect. 4.2.1), which started in 1961, Dansgaard (1964) worked out the general effects of condensation-evaporation processes on the isotopic composition in precipitation.

A strong dependence between the isotope ratio and the temperature can be explained by the Rayleigh-model. For a given evaporation temperature, the 'temperature effect' determines the isotope ratio in precipitation mainly by the condensation temperature. At temperatures below  $-20^\circ\text{C}$ , the above mentioned non-equilibrium processes play a role.

A second effect is called the 'continental effect', which describes the isotopic depletion of water by its transport further inland. Since the heavier isotopologues preferably condensate and rain out, lower  $\delta$  values can be observed at stations located away from the oceans.

This process is also one of the reasons for the 'amount effect', which accounts for lower isotope ratios at higher amounts of precipitation in a rainshower. Other reasons for this effect are the partial reevaporation of the raindrops below the cloud base and the isotopic exchange of the drops with the surrounding air, which both cause an isotopic enrichment of the precipitation. Due to the lower humidity below the cloud base and the smaller rain drops in light showers, these effects are strong in light and suppressed in heavy showers. Additionally to these explanations by Dansgaard (1964), Rozanski et al. (1993) suggested the hypothesis that in strong showers the isotopic exchange with falling raindrops also decreases the isotope ratio of the vapour in the cloud. Thus the 'amount effect' can mainly

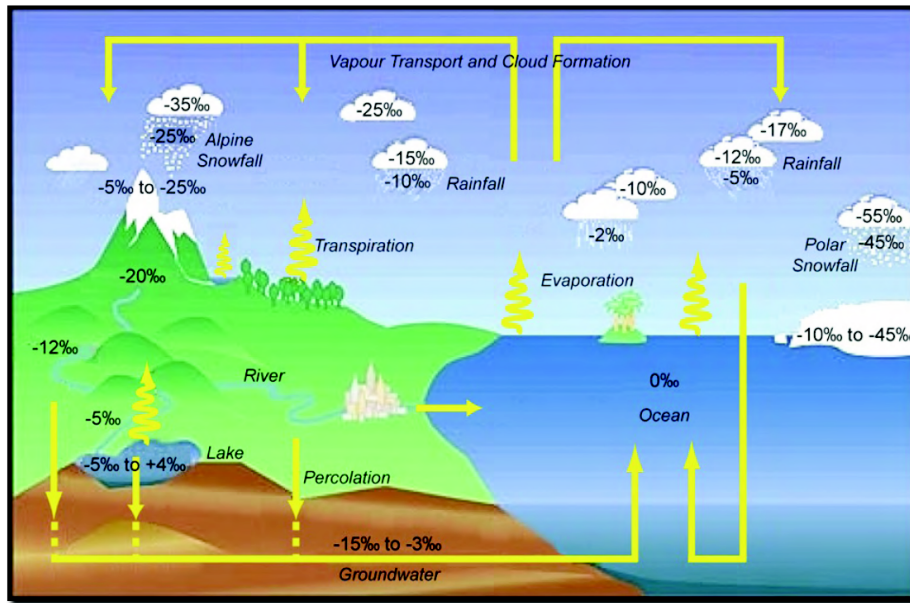


Figure 2.11: Schematic overview of the hydrological cycle showing approximate values of  $\delta^{18}\text{O}(\text{H}_2\text{O})$ , (Schotterer et al., 1996)

be observed in heavy convective showers within the tropics, a quantitative analysis of the respective processes has been conducted by Lee and Fung (2007).

Further on the 'altitude effect' explains strongly depleted isotope ratios in precipitation at higher altitudes. Orographically forced convection leads to rain out of heavy isotopologues and lower condensation temperatures. Ambach et al. (1968) detected an isotopic altitude effect of  $-0.2\text{‰}$  per 100 m in the Alps. Moreover, Friedmann and Smith (1970) measured more negative  $\delta$  values on the lee side of mountains compared to the windward side, due to the rain out. Fig. 2.11 schematically shows approximate  $\delta^{18}\text{O}(\text{H}_2\text{O})$  values within the hydrological cycle due to the various forms of isotopic depletion. The described effects can be derived from the image.

# Chapter 3

## New EMAC model developments

### 3.1 The EMAC model system

EMAC (ECHAM MESSy Atmospheric Chemistry) is a numerical Chemistry and Climate Model (CCM) system, which contains the General Circulation Model (GCM) ECHAM5 (described in the next section) and the MESSy (see Sect. 3.1.2) submodel-coupling interface. The ECHAM5 model constitutes the core atmospheric model (basemodel) of EMAC and is connected to the modular interface structure MESSy describing atmospheric and chemical processes and their interactions with oceans, land and human influences. EMAC is aiming at becoming a comprehensive Earth System Model (ESM), including all the interacting domains (atmosphere, hydrosphere, cryosphere, ...) of the environment and it is constantly further developed. This model system, which is extendable for miscellaneous processes, allows to study the feedbacks between chemical, physical and biological processes and how they influence the whole system (Jöckel et al., 2005).

#### 3.1.1 The general circulation model ECHAM5

ECHAM (ECMWF Hamburg) is an atmospheric general circulation model. The part describing the dynamics bases on a global numerical weather prediction model developed at the ECMWF (European Center for Medium Range Weather Forecasting) and includes a comprehensive parameterisation package developed at the Max-Planck Institute for Meteorology in Hamburg to meet the needs for climate simulations. The dynamical part of ECHAM is formulated in spherical harmonics and the transform technique is used such that non-linear terms, including parameterisations, are evaluated at a set of almost regularly distributed grid points - the Gaussian grid (Roeckner et al., 2003). The ECHAM5 model, which is the fifth generation of the ECHAM model, was used as basemodel for the EMAC model system.

#### 3.1.2 The submodel-coupling interface structure MESSy

The Modular Earth Submodel System (MESSy) provides a bottom-up approach towards Earth System Modelling. It comprises a modular interface structure for the standardised control of process-based modules (submodels) and their interconnections, an extendable

set of such for various processes and a coding standard. It is written in Fortran95. MESSy is an open, multi-institutional project providing a strategy for developing comprehensive Earth System Models (ESMs) with highly flexible complexity.

Technically, MESSy distinguishes four different model layers, the basemodel layer (BML), the submodel core layer (SMCL) and the two respective interface layers (BMIL and SMIL). In EMAC the ECHAM5 model constitutes the basemodel layer, whereas most of the processes are separated as submodels from the basemodel layer to the submodel layer. A status overview of version 2 of MESSy is given in Jöckel et al. (2010). The basemodel interface layer can be regarded as a socket where the individual modules of the SMCL can dock with their interface layer (SMIL). This structure is sketched in Fig. 3.1.

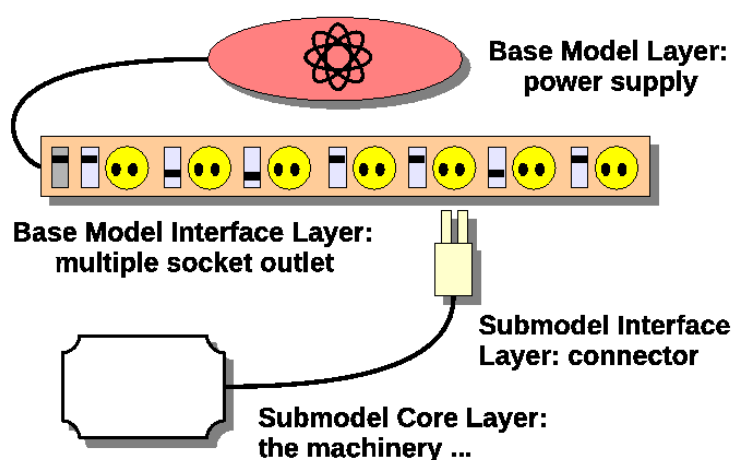


Figure 3.1: Sketch of the four layers of MESSy, from Kerkweg and Jöckel (2012).

To meet the needs of a chemistry model, the generic submodel TRACER was developed (Jöckel et al., 2008). Apart from several other features, this submodel provides the possibility to define a multitude of tracer sets. The required information about a specific chemical species is split into the static meta-information about the characteristics of the species and its abundance in the corresponding geometric representation.

## 3.2 The TENDENCY submodel <sup>1</sup> - preparatory work

In Earth System Models (ESMs) individual processes are described by various numerical algorithms for solving the underlying mathematical equations. Here, the term “process” describes any abstraction of a mechanism which alters the state of the system, those could be of physical, dynamical, chemical, biogeochemical, or even socio-economical nature. A

<sup>1</sup>A modified version of this section has been submitted for publication in Geoscientific Model Development (Eichinger, R. and Jöckel, P. (2014). The generic MESSy submodel TENDENCY (v1.0) for process-based analyses in Earth System Models) and is under review at the time of the submission of this PhD thesis.

corresponding “operator” describes the processes’ algorithmic formulation, which yields a deterministic output for any given (reasonable) input. Finally, within MESSy any coded realisation of the corresponding operator is defined as a “submodel”. (Not all the MESSy submodels, however, necessarily represent processes. Some are designed for diagnostic purposes, only, and a third class, comprising the here presented TENDENCY submodel provide some basic model infrastructure.) Thus, in a certain sense, the terms “process”, “operator” and “submodel” can be used as synonyms (and will be hereafter throughout the text).

The method of choice for the combination of the individual processes is the so-called *operator splitting concept*. In this method the contributing processes modifying a specific prognostic variable are calculated in sequence, each adding its individual contribution to the overall change over time (i.e., the total tendency). Depending on the chosen time integration scheme, these individual process tendencies (of a specific prognostic variable) depend on the initial condition (or the state of the prognostic variable at the end of one or more time steps before), and the sum of the process tendencies at the same time step in the sequence of operators before. Commonly in ESMs only the total tendency is analysed and the information about the individual contribution of a certain process to the change of a state variable is lost. Understanding the effects of individual processes on the state variables, however, is important for unravelling the driving mechanisms of patterns generated by ESMs. Moreover, the process-based tendencies of state variables can serve as input to further calculations of physical or chemical processes.

Approaching the issue by excerpting every process tendency of each state variable directly from the operators would cause a range of technical problems like an excessive memory usage and a very inflexible data handling. Therefore a comprehensive and easily expandable infrastructure submodel was implemented in this study, which is based on the outsourcing of the tendency accounting from every process submodel to it, and name it TENDENCY. Beginning with version 2.42 of MESSy (Jöckel et al., 2010) TENDENCY is part of the overall model infrastructure. TENDENCY operates on all prognostic variables, including tracers (generic submodel TRACER, Jöckel et al., 2008). The structure of TENDENCY is independent of the used time-integration scheme and thus the method is applicable to other model systems as well. Moreover, the process-based diagnostics can be set up by the user via namelist during runtime, tailor-made for the desired application, and thus avoiding a waste of memory. In Sect. 3.2.1 the implementation of TENDENCY is described, including specifics of the used EMAC model system (Jöckel et al., 2010). The benefits and the methods of the user-controlled diagnostics are described in Sect. 3.2.2. Furthermore in this section an optional closure test is explained, which is included in the TENDENCY submodel and makes the model less error-prone. A runtime performance analysis was carried out to determine the additional computing time arising from the increased usage of subroutine calls. Sect. 3.2.3 describes the test-method and the results which indicate an overhead of  $1.8 \pm 1\%$ . An analysis of the water vapour tape recorder by means of the method is presented in Sect. 3.2.4. Since the TENDENCY submodel was developed in a manner that all MESSy users can use and extend it to other sub- and basemodels, a detailed reference manual of submodel is available in the appendix.

### 3.2.1 Implementation

ESMs aim on representing the physical and chemical processes of the real world as realistic and complete as possible. To approach this aim these processes are solved numerically by individual algorithms. In the model the algorithms perform sequentially as operators which alter the prognostic variables. The common method of choice for the sequential combination of the operators is the operator splitting concept, which is illustrated in Fig. 3.2. According

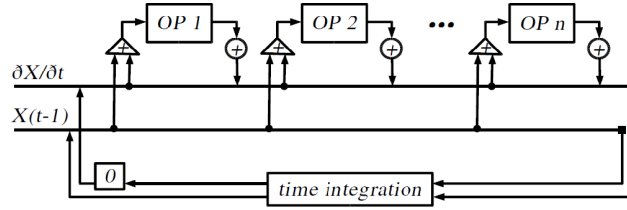


Figure 3.2: Operator splitting concept, from Jöckel et al. (2005).

to this principle a total tendency is computed for a given state variable ( $X$  in Fig. 3.2) by the different operators ( $OP 1 \dots OP n$  in Fig. 3.2) in sequence and the sum ( $\partial X / \partial t$ ) is added at the end of the time step to the value from the beginning of the time step ( $X(t-1)$ ). Exemplarily, the operator sequence controlling the specific humidity  $q$  in EMAC is explained. The first operator to be called is ADVECT ( $OP 1$ ), which simulates the advection of water vapour. As all the tendencies are set to zero at the beginning of the model time step, the ADVECT tendency is based solely on the initial value ( $X(t-1)$ ). The next operator, e.g. VDIF (representing vertical diffusion) computes a tendency based on the initial value and the tendency calculated by the ADVECT operator. The operator  $OP n$ , which in this example is CLOUD, hence bases on the initial value and the sum of the tendencies of all the previous operators. At the end of each time step the sum of all the tendencies calculated by the individual submodels results in the total change of the prognostic variable. The individual process tendencies, however, are commonly computed within the respective operators and afterwards not used anymore. Thus these values are overwritten in the following time step and hence the information is lost.

Extracting always all process tendencies for all state variables with a straightforward approach by making them globally available would cause several technical problems, for instance an excessive memory requirement. A more flexible method is therefore required. Hence, in order to retrieve the process-based model tendencies of the state variables in a standardised and configurable manner, additional code has to be included throughout the model system. Apart from the development of the TENDENCY module itself (details see Sect. 3.2.1.1), every subroutine which computes tendencies has to be modified: the tendency accounting is relocated to the TENDENCY module, where a user-defined record is kept. Details of the implementation are given in Sect. 3.2.1.2 and special notes concerning the EMAC model are documented in Sect. 3.2.1.3.

Each MESSy submodel comprises subroutines for the initialisation, the time integration and the finalising phase. The submodels are connected via standardised interfaces and are controlled by a central unit (generic submodel SWITCH/CONTROL) calling one after the

other. During the initialisation phase, among other things, the memory is set up, while during the integration phase the actual development of the state variables in space and time is calculated. The memory in the EMAC model is managed via the MESSy submodel CHANNEL (Jöckel et al., 2010), which is also utilised for TENDENCY.

Commonly, within each prognostic submodel a process tendency for a specific state variable is calculated and added directly to the total tendency. The TENDENCY submodel is based on the outsourcing of this tendency accounting (i.e., the addition to the total tendency) from the submodels to the TENDENCY module. Fig. 3.3 illustrates this concept. The addition of the process tendency to the total tendency in a specific submodel is replaced by a call to an interface subroutine of TENDENCY, thus handing over the control over the tendency (Tend in Fig. 3.3). This allows to keep a record of the process-based tendencies of state variables. The output and corresponding memory requirements, however, can now be controlled via a namelist by the user. This generalised access to the process tendencies is less error-prone and more user-friendly, because no recoding is required for tailor-made tendency diagnostics. Additional submodels can easily be equipped with the TENDENCY feature by following the recipe in Sect. 3.2.1.2. The principle of the TENDENCY submodel is independent of the time-integration scheme and therefore can be applied to every model system. An overview about the TENDENCY module itself is given next.

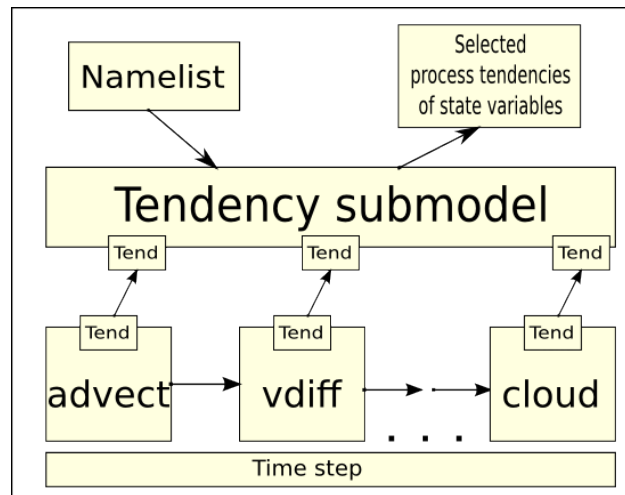


Figure 3.3: Schematic of the MESSy TENDENCY submodel within the framework of the EMAC model system. The addition of the individual process tendencies to the total tendency is now outsourced from the respective submodels to the TENDENCY submodel. A user-controlled namelist provides several possibilities for the output of the process tendencies of state variables.

### 3.2.1.1 The TENDENCY module

The TENDENCY module operates in all three phases of the model: the initialisation phase, the time integration phase, and the finalising phase.

The main entry points are called once from the basemodel interface layer (BMIL, for definition see Jöckel et al., 2010). In the initialisation phase the subroutine

- `main_tendency_initialize` reads the TENDENCY CPL-namelist and sets up the “handles” and prognostic variable registrations (both explained below) for those processes of the basemodel, which have not yet been re-implemented as MESSy submodels.
- `main_tendency_init_coupling` parses the TENDENCY coupling (CPL)-namelist entries and sets up internal data structures and memory (channels and channel objects, Jöckel et al., 2010), depending on the user request in the CPL-namelist.

In the time integration phase the subroutine

- `main_tendency_global_end` performs the internal closure test (explained below), if requested by the user in the CPL-namelist.
- `main_tendency_reset` resets the internal tendencies to zero at the beginning of the next time step.

And in the finalising phase the subroutine

- `main_tendency_free_memory` frees the non-channel object related memory and deletes the internal data structures.

Besides these main entry points, TENDENCY provides a number of functions and subroutines, which need to be called from within the various submodels (more precisely from their respective submodel interface layer, SMIL; for definition see Jöckel et al., 2010). During the initialisation phase, each submodel needs to

- be associated with a unique integer identifier (which is called “handle”). This is accomplished by calling the function `mtend_get_handle` as provided by the TENDENCY submodel. This function requires as argument a unique name of the process, which can be used in the user interface (see Sect. 3.2.2.1), i.e., the CPL-namelist.
- register the prognostic variables, which are subject to be modified. This is done by calling the subroutine `mtend_register` with the process handle and a unique identifier (provided as integer parameter by TENDENCY) of the respective prognostic variable as arguments.

Note that for processes of the basemodel, which have not yet been re-implemented as MESSy submodels, these two steps are performed within `main_tendency_initialize` (see above). These initialisation procedures are used to set up an internal logical structure, which is used in combination with the user request (CPL-namelist), to set up the memory (in `main_tendency_init_coupling`) and to control the tendency accounting during the time integration phase.

During the time integration phase, mainly two subroutines are called by each submodel:

- `mtend_get_start` is called to calculate the up-to-date (“start”) values of the respective prognostic variable.
- `mtend_add` is called to add the new process tendency to the total tendency.

Both subroutines need to be called for each prognostic variable to be modified. Details on the argument lists of TENDENCY subroutines are documented in the appendix.



### 3.2.1.2 Equipping submodels with the TENDENCY feature

Tab. 3.1 shows the required submodel modifications exemplarily for the temperature as prognostic variable. As can be seen, the TENDENCY approach has some advantages: The direct access (by Fortran `USE`) to the central prognostic variables and their corresponding tendencies (in the example *tm1* and *tte*) is not longer required. The same holds for the time step length (*time\_step\_len*) for calculating the start value (*t*), which is potentially (in Tab. 3.1 not explicitly shown) required to calculate the process tendency *my\_tte*. This is less error prone, since the correct calculation (last two rows in Tab. 3.1) is entirely hidden in the TENDENCY submodel.

As Tab. 3.1 shows, equipping a submodel with the TENDENCY option requires four main modifications. Two during the initialisation phase and two during the time-integration phase of the submodel. During the initialisation phase a handle (see Sect. 3.2.1.1, in the example *my\_handle*) has to be assigned to each submodel by calling the function `mtend_get_handle`. Additionally the subroutine `mtend_register` must be called for every variable which is going to be altered by the submodel (temperature in the example, selected via the identifier *mtend\_id\_t*). This registers the respective process - prognostic variable pair in the TENDENCY module and sets an individually assigned logical to "true". This is used for the definition of the respective channel object (memory) as well as for controlling the calculations in the time integration phase.

During the integration phase of the model the computation of the start values of the prognostic variables as well as the addition of the process-based tendencies are replaced by calls of subroutines from the TENDENCY module. The subroutine `mtend_get_start` now computes the start values and the subroutine `mtend_add` updates and records the tendencies. The respective start values represent the sum of the initial value (the value from the previous time step) and all the process tendencies of the submodels called prior to this submodel multiplied with the time step length.

Since not all submodels could be modified for TENDENCY at once, and also to enable model configurations without the TENDENCY feature, the submodel modifications were encapsulated in pre-processor directives. Additional code is introduced using

```
#ifdef MESSYTENDENCY
... new code ...
#endif
```

and code, which is modified for the usage of TENDENCY, looks like:

```
#ifndef MESSYTENDENCY
... original code ...
#else
... TENDENCY specific code ...
#endif
```

Thus all modifications and the TENDENCY submodel are only active if the model is configured with `--enable-MESSYTENDENCY`. This structure is also recommended for equipping further submodels with the TENDENCY feature.

without TENDENCY	with TENDENCY
initialisation phase	
	USE messy_main_tendency_bi, & ONLY: mtend_get_handle, & mtend_register, mtend_id_t
	INTEGER :: my_handle
	my_handle = & mtend_get_handle(modstr) CALL mtend_register & (my_handle, mtend_id_t)
time integration phase	
USE messy_main_data_bi, & ONLY: tte, tm1 USE messy_main_timer, & ONLY: time_step_len	USE messy_main_tendency_bi, & ONLY: mtend_add_l, mtend_get_start_l
t(:,:)=tm1(:,:)+tte(:,:)*time_step_len	CALL mtend_get_start_l & (mtend_id_t, v0=t(:,:))
tte(:,:) = tte(:,:) + my_tte(:,:)	CALL mtend_add_l & (my_handle, mtend_id_t, px = my_tte(:,:))

Table 3.1: Required modification of submodels. The example shows the modification of the total temperature tendency *tte*. The left column shows the typical classical code, the right column the TENDENCY approach. The value from the time step before is *tm1*, the local variable *t* is the current (start) value, and *my\_tte* is the new, additional tendency, also a local variable. The time step length is *time\_step\_len* and *modstr* denotes the name of the respective submodel. Note that the “\_l” suffix of *mtend\_add* and *mtend\_get\_start* are due to different possible entry points with access to different ranks of the variables (here 2 dimensional, see Sect. 3.2.1.3).

### 3.2.1.3 EMAC-specific implementation details

Since some processes of the physics in EMAC (v2.42) have not yet been re-implemented as independent MESSy submodels, they are still operated directly within the ECHAM5 basemodel. In the sequence of operations, the MESSy infrastructure initialises the memory before the remaining parts of the basemodel ECHAM5 are initialised. On the other hand, the process - prognostic variable pair registrations determine the memory (channel objects). Thus the function `mtend_get_handle` and the subroutine `mtend_register` would be called too late, if only called from the remaining parts of the ECHAM5 basemodel. Therefore these associated process identifiers (namely ADVECT, SURF (In MESSy 2.50 SURF has been replaced by the MESSy submodel SURFACE) VDIFF, GWSPECT, SSO-DRAG, DYN) have to be assigned, and the possible process - prognostic variable pairs have to be registered already during the initialisation phase of the TENDENCY module itself (see also Sect. 3.2.1.1).

A second EMAC specific is owed to the spectral transform dynamical core of the ECHAM5 basemodel: The wind speed is usually in units of m/s, but to meet the needs of the spectral transform on the sphere, it has to be scaled with the cosine of the latitude. Various physical subroutines in the EMAC model, however, perform with the unscaled wind speed. Within TENDENCY always the scaled wind speed is used. To avoid inconsistencies, TENDENCY provides the subroutine `mtend_set_sqcst_scal`, which is used to set an internal logical switch telling TENDENCY if the incoming wind tendency is scaled or not.

The third EMAC specific is related to the dimensions of the prognostic variables in 3-dimensional grid-point space. The ECHAM5 basemodel uses a specific order of dimensions  $((h_1, z, h_2))$  where  $h_1$  and  $h_2$  denote the horizontal and  $z$  the vertical dimensions) for code optimisation. Hereby some of the processes perform within a loop over the outer horizontal dimension  $h_2$ . Therefore a distinction had to be made between those processes being called globally (outside the  $h_2$  loop) and those being called locally (inside the  $h_2$  loop). In the TENDENCY submodel this issue occurs during the time integration phase, i.e., concerning the `mtend_get_start` and the `mtend_add` subroutines. Here, the arrays have to be of rank 2  $((h_1, z))$ , if called inside the local loop, and of rank 3  $((h_1, z, h_2))$ , if called outside. Therefore both subroutines are found twice in the TENDENCY module suffixed by either `_l` (for local) or `_g` (for global), and differing only by the rank of the array arguments.

## 3.2.2 Diagnostic methods with TENDENCY

The implementation of the MESSy generic submodel TENDENCY provides several benefits concerning the handling of the process-based tendency data. The CHANNEL infrastructure allows a flexible and user-defined output of the information and thus the memory requirement can be minimised depending on the specific needs. This section describes the independent modes of operation, how the information can be extracted by the user and the optional closure test.

### 3.2.2.1 User interface

The TENDENCY submodel provides various options for the user to receive data output, which have to be set prior to the model simulation. This is realised via two interfaces

connected with the module, the corresponding coupling (CPL) namelist and the integrated subroutine `mtend_request`.

The CPL-namelist contains three logical parameters:

- `l_full_diag` enables the full diagnostic output, i.e., channel objects (in a separate output channel “`tendency_full`”) for the tendencies of all possible process - prognostic variable pairs are created. This option requires considerably large memory and has been mainly implemented for debugging purposes.
- `l_closure` enables the internal closure test and creates the additional channel “`tendency_clsr`” with objects required for the closure test (see Sect. 3.2.2.2). This test has been implemented to check if all submodels in a given model setup work correctly with respect to the tendency accounting.
- `l_clos_diag` enables additional output of information during the model simulation into the log file. This contains the external and the internal tendencies (for explanation see Sect. 3.2.2.2) as well as their difference and is mostly used for development and debugging purposes, e.g., when including a new submodel.

Individual tendency diagnostics can be requested in the CPL-namelist with entries looking like

```
TDIAG(i) = 'X', 'p1;p2+p3;...;pn',
```

where `i` is an arbitrary but unique number, `X` is the name of the prognostic variable (or tracer), and `p1` to `pn` are the names of the processes (see Sect. 3.2.1.1). `TENDENCY` creates a new output channel (named “`tendency_diag`”) and one channel object for each semicolon separated list of process sums. These objects either contain the individual tendency of the process - variable pair (example `p1`), or the sum of tendencies of the corresponding processes (example `p2+p3`). An additional “unaccounted” object is created, which contains the sum of all process tendencies missing in the list. If the “unaccounted” object is zero for all time steps in every grid box, all processes influencing the variable `X` are within the set of processes `p1` to `pn`. With this feature, tailor-made diagnostics excerpting only the desired tendencies, thus with a minimised memory requirement, can be set up.

Besides the CPL-namelist controlled generation of new output objects containing individual process tendencies (or sums thereof), `TENDENCY` also provides an interface subroutine to enable the access to individual process tendencies by other submodels. Calling `mtend_request` from the entry point “`init_coupling`” of submodel *A* with the name of the desired submodel *B* and the identifier of the desired prognostic variable *X* will generate a new channel object in the channel “`tendency_exch`” (for exchange) and return a pointer to its memory. If the corresponding process submodel *B* will commit its tendency by calling `mtend_add`, this tendency will be copied into this new channel object and therefore be available in submodel *A* for further calculations.

As for each of the possible modes of operation of the `TENDENCY` submodel an individual channel is generated, they do not exclude or influence each other, but rather work independently.

### 3.2.2.2 Closure test

An optional closure test can be performed with the TENDENCY submodel for every time step during the simulation. The test is mainly implemented for development tasks like including new submodels to the TENDENCY structure. If activated via the namelist (see Sect. 3.2.2.1), two additional process handles (*IHANDLE\_SUM* and *IHANDLE\_DIFF*) are defined. Further, a separate channel “tendency\_clsr” is created with corresponding channel objects, two (“sum” and “difference”) for each prognostic variable. The “sum” objects are updated every time a tendency is updated in the `mtend_add` subroutines and thus display the total sum of tendencies, which are calculated only within the TENDENCY module (in the following called “internal tendency”). As with TENDENCY the total model tendency (in the following called “external tendency”) should be calculated only within the TENDENCY submodel, those two values are supposed to be equal. If these two values differ, the respective variable must be altered by another process of which the tendency computation was not relocated to the TENDENCY submodel. Testing this denotes the closure test which is conducted as follows: The channel objects corresponding to the handle *IHANDLE\_DIFF* are used to store the difference between the two tendency values calculated in the subroutine `main_tendency_global_end` by subtracting the internal from the external tendency. This difference is used in the subroutine `compute_eps_and_clear`. In this subroutine an  $\varepsilon$  is calculated by

$$\varepsilon = (\max |xte_e|) \cdot 10^{-10} \quad , \quad (3.1)$$

where  $xte_e$  denotes the external tendency of the variable or tracer  $x$ . Next, the difference between the two tendencies is challenged to be smaller than  $\varepsilon$ . If so, certainty is given that all processes changing the respective prognostic variable are properly captured by the TENDENCY submodel. If not, an error message will occur in the log file.

### 3.2.3 Runtime performance analysis

Including the TENDENCY submodel into the EMAC model leads to a number of additional subroutine calls during the simulation. To estimate the extra computing time the EMAC model requires for these, a runtime performance analysis has been conducted. For this, four model simulations (with EMAC version 2.42) over ten model days with a time step of 15 minutes were carried out on one node with 64 tasks per node on the “blizzard” IBM Power 6 of the DKRZ (Deutsches Klimarechenzentrum) in Hamburg. While in two of the four simulations the TENDENCY submodel was performing, in the other two it was switched off.

The model resolution of T42L90MA was chosen with a model setup including only the dynamical core of the ECHAM5 basemodel and the basic submodels of the MESSy system (namely: CLOUD, CONVECT, CVTRANS, H2O and RAD4ALL) as well as the extra routines for the middle atmosphere (GWSPECT, SSODRAG). In order to receive comparable results, apart from the wall clock no data output was enabled and due to the initialisation phase of the model the first time step was not taken into consideration. For the calculation, the sum of the wall clock time has been taken for every MPI (Message Passing

Interface) parallel task and for every time step of one model simulation. The equation

$$O = \left( \frac{\sum_{p=1}^P \sum_{n=2}^N t_{on}(p, n)}{\sum_{p=1}^P \sum_{n=2}^N t_{off}(p, n)} - 1 \right) \cdot 100 \quad (3.2)$$

yields the averaged value of the overhead (O) produced by the additional submodel per time step in percent. Here,  $n$  indicates the time step,  $P$  the number of MPI tasks and  $t_{on}$  and  $t_{off}$  represent the wall clock time for the simulations with the TENDENCY submodel either switched on or off. In these tests the use of the TENDENCY submodel results in an additional  $1.8 \pm 1\%$  of computing time for the EMAC model in the described setup.

### 3.2.4 Process analysis of stratospheric water vapour

By means of this new analysis tool, the water vapour tape recorder in the stratosphere is investigated. The left panel of Fig. 3.4 shows the simulated representation of the well-known tropical ( $5^\circ\text{N}$ - $5^\circ\text{S}$ ) tape recorder signal between 100 hPa and 10 hPa for three simulated years, which was first discovered by Mote et al. (1995), Weinstock et al. (1995) and Mote et al. (1996). For this, a model simulation in T42L90MA resolution (approximately  $2.8^\circ \times 2.8^\circ$ , 90 vertical layers) initialised from a previous long-term simulation was carried out. Only the basic MESSy submodels (CONVECT, CLOUD, CVTRANS, RAD4ALL, TROPOP) and the ECHAM5 basemodel are used plus the submodel H2O, which provides a simple prescribed water vapour production accounting for the methane oxidation in the stratosphere.

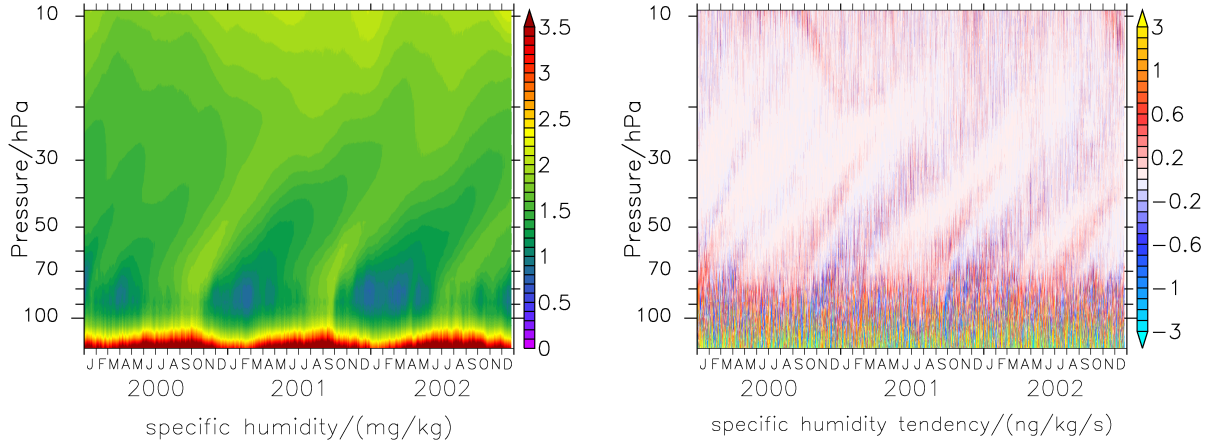


Figure 3.4: Zonally averaged specific humidity (left) and total tendency of the specific humidity (right) from  $5^\circ\text{S}$ - $5^\circ\text{N}$ .

In the right panel of Fig. 3.4 the total tendency of the water vapour is shown for the simulated time period. Here a fairly clear distinction can be made between reddish (increasing water vapour) and bluish (decreasing water vapour) patches. These in fact correspond to the increasing and decreasing specific humidity over time in the left panel.

White patches in the tendency correspond to the maxima and minima of the respective total value. The signal of the total tendency also propagates upward in time, like the actual tape recorder signal. At a pressure lower than 30 hPa, the signal dissolves or mixes in with less clear patterns in the upper stratosphere.

Fig. 3.5 shows the process-based tendencies retrieved via the TENDENCY submodel. For this the line

```
TDIAG(2) = 'q' , 'vdiff;cloud;convect;advect;h2o',
```

was included into the CPL namelist. As explained in Sect. 3.2.2 this generates an output file for the process tendencies of the specific humidity for each of the five stated submodels, involved in controlling the prognostic development of the specific humidity. The sixth generated output object accounting for the unaccounted submodels was tested to be zero at any time and location, to assure that all the processes influencing the specific humidity have been captured.

The two uppermost panels of Fig. 3.5, showing the tendencies caused by large-scale clouds (CLOUD) and convective clouds (CONVECT), reveal, as expected, no signal above the tropopause or the lower stratosphere. The mostly bluish colour at the bottoms of the images accounts for condensating and re-sublimating water vapour and cloud formation, which reduces the specific humidity of the vapour. The small red spots (hardly visible) on top of the blue colour are due to water vapour transport in the convection submodel (CONVECT) and due to evaporation and sublimation of transported liquid or ice water in the CLOUD submodel.

The central panel of Fig. 3.5 shows the impact of vertical diffusion (VDIFF). A strong signal goes up to 80 hPa. Above that region, the signal is considerably weaker. The vertical diffusion tendencies are about three orders of magnitude smaller than the total tendencies. Above 50 hPa there are almost no changes caused by vertical diffusion, apart from a downward propagating signal. It seems to be in phase with the quasi-biannual oscillation (QBO), which may influence the strength of the tape recorder signal (Niwano et al., 2003).

The prescribed water vapour production caused by methane oxidation is shown in the lower left panel of Fig. 3.5. The continuous production of water vapour from the chemical reactions increases with height and varies slightly with season. The magnitude of the tendencies are about one order of magnitude smaller than the maxima of the total tendencies.

The advection tendency of the specific humidity can be seen in the lower right panel of Fig. 3.5. It reproduces the tendency tape recorder signal from the total specific humidity tendency in Fig. 3.4 fairly well, but is weaker. The advection tendency indicates upward propagation from 80 hPa to 30 hPa where it fades out. In the upper stratosphere the advection tendencies also resemble the total tendencies, but with reduced magnitude.

Fig. 3.6 shows the three-year temporal and zonal averages of the individual tendencies at the equator, to provide a picture of the net effect of the processes over the entire simulated period. Here again can be seen, that the influence of the two cloud processes and of the vertical diffusion fade out above the tropopause and the water vapour production by methane oxidation simply increases with height. The averaged advection tendency changes

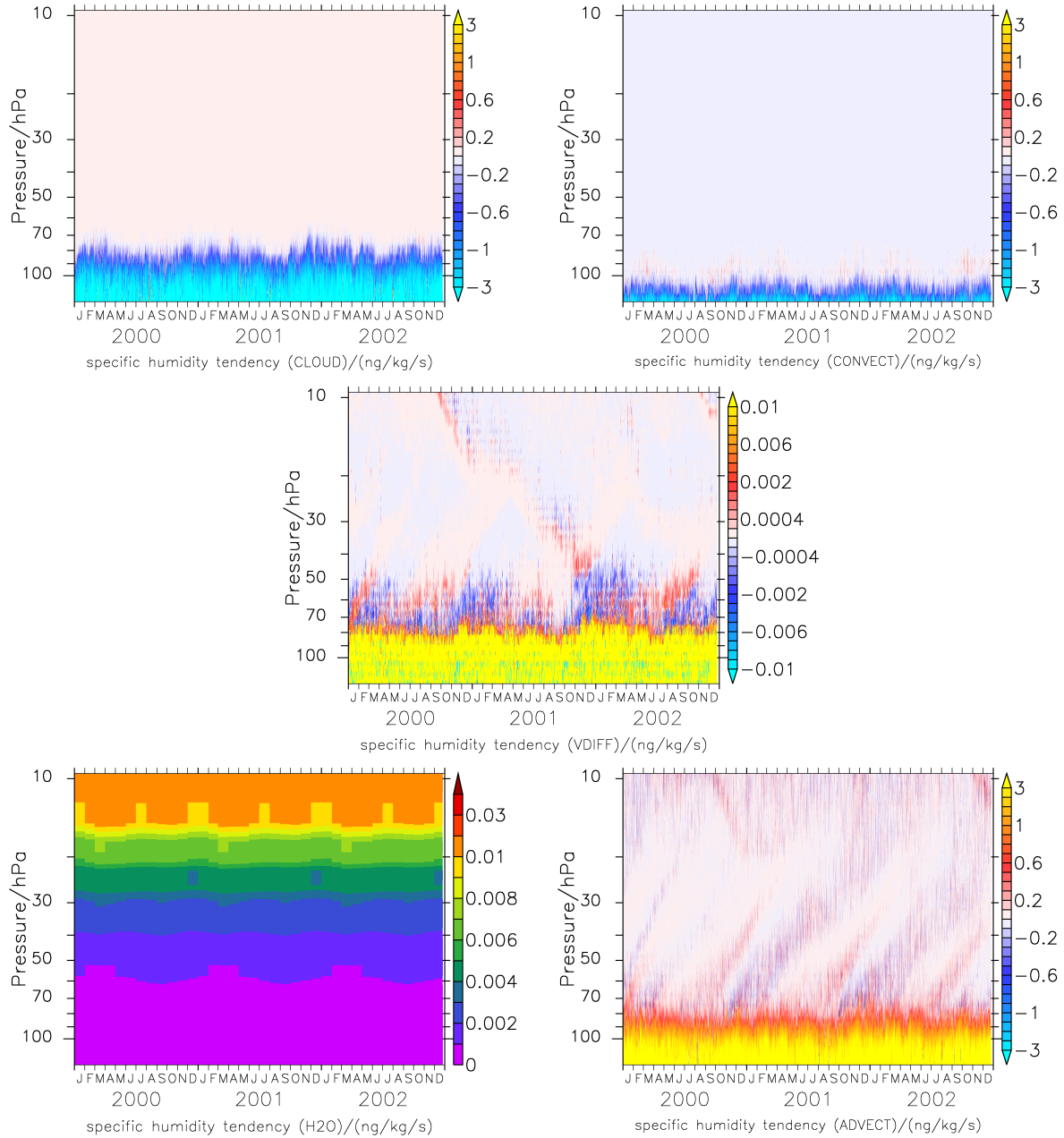


Figure 3.5: Zonally averaged tendencies of the individual processes influencing the specific humidity from 5°S-5°N: CLOUD for large-scale clouds, CONVECT for convective clouds, VDIFF for vertical diffusion, H2O for the chemical production of water, ADVECT for advection.



from positive to negative values at around 50 hPa and above balances the chemically produced water vapour. As the methane oxidation provides a constant signal, it has the same net effect as the advective impact when temporally averaged, even though the maxima are one order of magnitude smaller. Without the chemical production of water vapour, the advection tendencies would become zero above around 30 hPa, from where on the specific humidity is fairly constant over time for a given altitude.

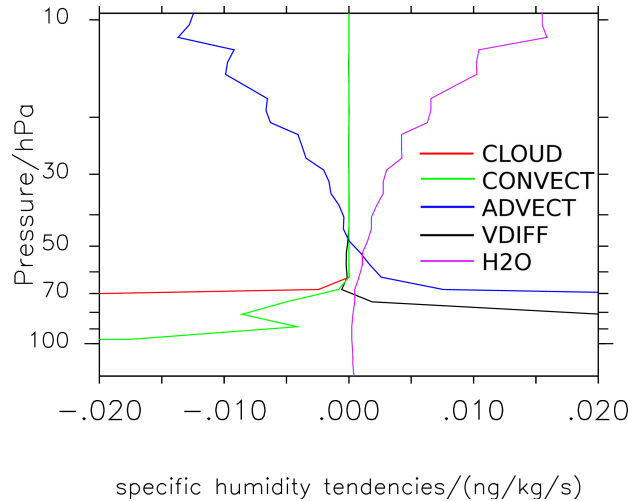


Figure 3.6: Temporally and zonally averaged process tendencies of the specific humidity at the equator. (CLOUD: large-scale clouds, CONVECT: convective clouds, ADVECT: advection, VDIFF: vertical diffusion, H2O: chemical production of water.)

### 3.3 The H2OISO submodel for stable water isotopologues

The explicit simulation of the stable water isotopologues HDO and  $\text{H}_2^{18}\text{O}$  has been included in several GCMs during the previous decades. Tab. 3.2 gives a chronological overview of the models and the associated references and institutes.

With some exceptions (e.g., Schmidt et al., 2005) most of these GCMs are designed for tropospheric research, usually for applications in paleoclimate. Hence, the models possess a rather sparse vertical resolution, usually no explicit stratospheric dynamics and moreover no component accounting for methane oxidation. The novelty of this work is therefore the focus on the stratosphere, including a well resolved stratosphere with explicit dynamics and a parameterisation for the chemical impact on the isotopic water vapour budget, which is described in Sect. 3.3.6.

The initial idea to use the individual process tendencies, provided by the TENDENCY submodel, directly, to compute the tendencies of the isotopologues, could not be pursued. The reason for this is, that firstly many intermediate values of the state variables between

Model	Reference	Institute
LMD	Joussaume et al. (1984)	LMD-Paris
GISS	Jouzel et al. (1987)	GISS-New York
ECHAM3	Hoffmann et al. (1998)	MPI-Hamburg
ECHAM4	Werner et al. (2001)	MPI-Hamburg
GENESIS	Mathieu et al. (2002)	Penn U.
MUGCM	Noone and Simmonds (2002)	Melbourne U.
MIROC3.2	Kurita et al. (2005)	JAMSTEC-Yokosuta
GISS-E	Schmidt et al. (2005)	GISS-New York
CAM2	Lee et al. (2007)	UC Berkeley
GSM	Yoshimura et al. (2008)	Scripps-San Diego
HadAM3	Sime et al. (2008)	BAS-Cambridge
HadCM3	Tindall et al. (2009)	U. Bristol
LMDZ4	Risi et al. (2010)	LMD-Paris
CAM3	Noone and Sturm (2010)	U. Colorado
ECHAM5	Werner et al. (2011)	AWI-Bremerhaven

Table 3.2: Stable water isotopologue enabled GCMs in chronological order.

individual phase changes within the respective submodels are needed for further calculations and secondly, a lot of additional information would have to be transferred from the submodels to H2OISO for this approach. This additional information is partly even overwritten many times within one time step (e.g., precipitation fluxes in CLOUD) and thus additional coding inside the submodels would be needed. Altogether, this approach could therefore not provide the assumed reduction of coding and computation expenses and hence a duplication of the entire hydrological cycle was applied (see next section).

Still, the TENDENCY submodel was of large assistance for the implementation of the water isotopologues in the H2OISO submodel. Debugging during the implementation of the submodel and the assurance of the correctness of the second hydrological cycle was largely simplified by the TENDENCY submodel. Moreover the correct calculation of the start values for the various state variables, which are needed for the isotopologue computations, could be generated in a structured manner through the transfer of the individual process tendencies to the H2OISO submodel. Lastly, the process-based tendencies of the isotopologues can also be of assistance for diagnosis of the processes controlling certain patterns, as was presented Sect. 3.2.4.

Since most of the code of the concerned parts for implementing the physics and dynamics of the water isotopologues in the EMAC model is adapted from the ECHAM5 model, plenty of it could be adopted from Werner et al. (2011). Due to the modularity of EMAC, however, the structural approach is entirely different. While the additional code in ECHAM5 is included directly in the model, which leads to another branch of the model, namely ECHAM5-wiso (wiso for water isotopologues), in EMAC it is implemented

as a MESSy-conform submodel. It contains tracers for the three stable water isotopologues  $\text{H}_2^{16}\text{O}$ ,  $\text{H}_2^{18}\text{O}$  and  $\text{HDO}$  for all three phases (vapour, liquid and ice), respectively (see Sect. 2.2) and an additional hydrological cycle, which includes all the processes that modify the water isotopologues. The modality of the implementation of the second hydrological cycle is described in the following section. For the isotopologues the fractionation processes are included for every relevant physical and chemical process, respectively, according to the theoretical basis explained in Sect. 2.2. In Sect. 3.3.2 to Sect. 3.3.6, a detailed description of the numerical implementation of all the parts of the individual modules, which are relevant for the modification of water vapour and hence the isotopologues in the EMAC-model, are given.

### 3.3.1 A second hydrological cycle including water isotopologues

Besides the regular hydrological cycle of the EMAC model, the H2OISO submodel contains a second one. For that, all the relevant computations of the quantities concerning water were doubled. This concerns the modules VDIFF (vertical diffusion), SURF (surface processes), ADVECT (advection), CLOUD (large-scale clouds), CONVECT (convective clouds) and CH4 (methane oxidation).

A schematic overview of the hydrological cycle is shown in Fig. 3.7. Here the blue arrows denote the regular pathways of water vapour, liquid water and ice. The standard ECHAM5 variables for these are  $Q$ ,  $XL$ ,  $XI$ , in the given order. The red arrows indicate the new, additional hydrological cycle, which contains the tracers for the three isotopologues in the three phases, respectively, namely  $\text{HHO}_{vap}$  for  $\text{H}_2^{16}\text{O}$  in the vapour phase,  $\text{HHO}_{liq}$  for  $\text{H}_2^{16}\text{O}$  in the liquid phase and  $\text{HHO}_{ice}$  for  $\text{H}_2^{16}\text{O}$  as ice and analogously  $\text{HH}^{18}\text{O}_{vap}$ ,  $\text{HH}^{18}\text{O}_{liq}$ ,  $\text{HH}^{18}\text{O}_{ice}$  and  $\text{HDO}_{vap}$ ,  $\text{HDO}_{liq}$ ,  $\text{HDO}_{ice}$ . Additionally to the regular hydrological cycle, here the fractionation processes are included for the isotopologues. The red boxes indicate the locations where fractionation takes place and describe the effects. More details are given in the following sections. Supplementary to previous studies, the chemical fractionation effects during the formation of water vapour through methane oxidation were considered (Sect. 3.3.6).

Although the  $\text{HHO}$  tracers actually only represent the isotopologue  $\text{H}_2^{16}\text{O}$ , for simplicity it is set to account for all the water isotopologues. Tab. 2.1 shows that the abundance of all the other isotopologues together is three orders of magnitudes smaller than that of  $\text{H}_2^{16}\text{O}$ . Hence, for its calculation, the remaining parts are negligible. Therefore the isotopologue  $\text{H}_2^{16}\text{O}$  represents a second water vapour, liquid water and ice content and can be used for the validation of the correctness of the second hydrological cycle by comparing it to  $Q$ ,  $XL$  and  $XI$  (see Sect. 4.1).

### 3.3.2 Vertical diffusion

As any conservative quantity, also the isotopologues in their three phases experience turbulent vertical transport and in the vapour phase also turbulent exchanges with the surface. The equation for the vertical diffusion of the water vapour mixing ratios  $\psi$  is

$$\frac{\partial \psi}{\partial t} = \frac{1}{\rho} \frac{\partial}{\partial z} \left( \rho K_{\psi} \frac{\partial \psi}{\partial z} \right) = \frac{1}{\rho} \frac{\partial}{\partial z} J_{\psi}, \quad (3.3)$$

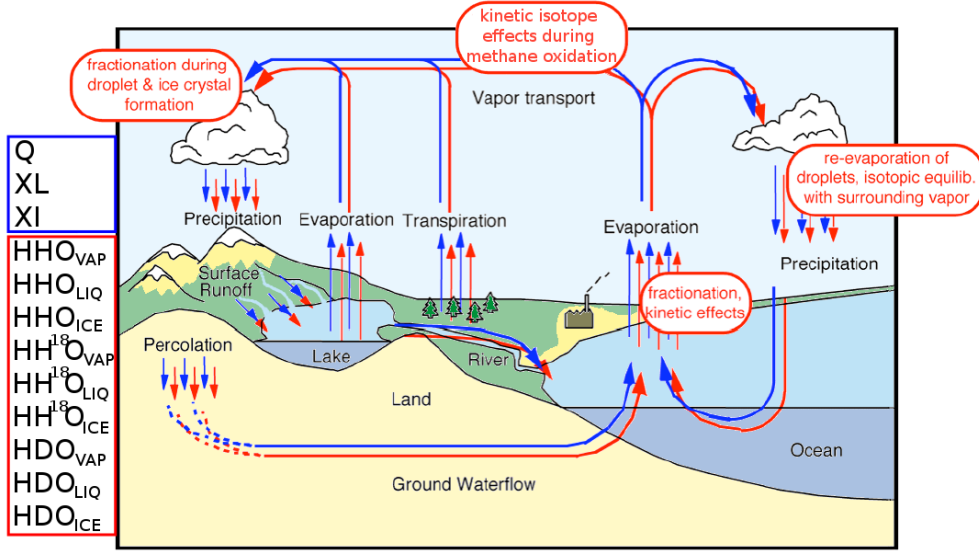


Figure 3.7: Schematic overview of the two hydrological cycles, adapted from M. Werner (personal communication, 2013)

where  $\rho$  stands for the density of the air,  $K_\psi$  for the exchange coefficient and  $J_\psi$  for the vertical turbulent flux. This scheme works mainly in the boundary layer, but operates also above, when static instability is generated. The upper and the lower boundary conditions are

$$K_\psi \cdot \frac{\partial \psi}{\partial z} = 0 \quad \text{for } p = p_T \quad (3.4)$$

and

$$K_\psi \cdot \frac{\partial \psi}{\partial z} = C_\psi \cdot |\vec{v}_h(z)| \cdot (\psi(z) - \psi_S) \quad \text{for } p = p_S. \quad (3.5)$$

Here  $p_T$  is the pressure at the top level of turbulence,  $p_S$  is the pressure at the surface and  $\vec{v}_h(z)$  is the horizontal wind vector. The drag coefficient  $C_\psi$  is dependent on the height  $z$  and on the stability of the layer.  $\psi_S$  denotes the value of  $\psi$  at the surface.

The lower boundary condition for the humidity and hence also for the vapour phase of the isotopologues is evaporation from oceans and land. For the latter, no fractionation is assumed in this study. As mentioned in Sect. 2.2.3 the fractionation of most of these processes are negligible or not resolved adequately in the model for consideration. The following section gives a more detailed overview about the surface processes. During the evaporation from the ocean, equilibrium and kinetic fractionation take place. Above the ocean surface,  $\psi_S$  represents the saturation mixing ratio  $q_{sat}$  for water vapour, which is dependent on the surface temperature and pressure. For a given isotopologue  $\xi$  the saturation mixing ratio  $q_{\xi,sat}$  is

$$q_{\xi,sat} = \frac{R_{oce}}{\alpha(T_S)} \cdot q_{sat}. \quad (3.6)$$

Here  $\alpha(T_S)$  stands for the surface temperature dependent equilibrium fractionation factor from Eq. 2.16 to Eq. 2.19 and  $R_{oce}$  is the isotope ratio of the ocean. Due to evaporation and precipitation,  $R_{oce}$  is not exactly VSMOW. As in the study by Werner et al. (2011), this lower boundary condition is prescribed with a global gridded data set based on the  $^{18}\text{O}$  isotopic composition in sea water by LeGrande and Schmidt (2006). Since there is no equivalent data set for the deuterium isotopic composition, the HDO content is prescribed with eight times the  $\text{H}_2^{18}\text{O}$  mixing ratios. This is in accordance with global observations (Craig and Gordon, 1965). For calculating the surface flux for water isotopologues  $J_\xi$ , the lower boundary condition (Eq. 3.5) thus changes to

$$J_\xi = \rho K_\xi \cdot \frac{\partial \xi}{\partial z} = \rho C_\xi \cdot |\vec{v}_h(z)| \cdot (1 - k) \cdot \left( \xi(z) - \frac{R_{oce}}{\alpha(T)} \cdot q_{sat} \right), \quad (3.7)$$

where  $1 - k$  accounts for the kinetic isotope effects during the diffusion of vapour (Eq. 2.24 and Eq. 2.25) (see also Merlivat and Jouzel, 1979; Hoffmann et al., 1998).

### 3.3.3 Surface processes

The land surface in the EMAC model is divided into a skin layer, intercepting parts of the precipitation, a snow layer and a soil water pool. From the soil water pool in turn, water either evaporates directly from bare soil, or is taken up by plants and then transpired into the atmosphere. The fractionation during evaporation from bare soil (see Gat, 1996), which was explained in Sect. 2.2.3, is not taken into account, because the surface scheme of the EMAC model includes only one soil reservoir. The isotope ratio of transpiring water from bare soil is therefore equal to the ratio of the water in this reservoir. This simplification has to be kept in mind for the analysis of the results. A similar approach was used for the other reservoirs. Fractionation during evaporation of water in the canopy and from the leaves of plants is negligible for time scales longer than a few hours (see Sect. 2.2.3). Also for evaporation from snow covered areas, we assume no fractionation. Hence the evaporation fluxes  $J$  for the respective reservoirs over land for the gaseous isotopologues  $\xi$  are (see also Hoffmann, 1995; Hoffmann et al., 1998):

$$J_{\xi,soil} = R_{soil} \cdot J_{\psi,soil} \quad (3.8)$$

$$J_{\xi,skin} = R_{skin} \cdot J_{\psi,skin} \quad (3.9)$$

$$J_{\xi,snow} = R_{snow} \cdot J_{\psi,snow} \quad (3.10)$$

$$J_{\xi,plant} = R_{plant} \cdot J_{\psi,plant} \quad (3.11)$$

Here  $\psi$  represents “normal” water and  $R$  the isotope ratio of the respective reservoir. The total evaporation flux  $J_\xi$  from land is therefore calculated by the sum of the individual surface fluxes:

$$J_\xi = J_{\xi,soil} + J_{\xi,skin} + J_{\xi,snow} + J_{\xi,plant} \quad (3.12)$$

### 3.3.4 Advection

The advection scheme used for tracer transport in the EMAC model is a flux form semi-Lagrangian (FFSL) scheme. This scheme was introduced by Lin and Rood (1996). The switch for advection, which is set in the meta-information during the tracer initialisation in MESSy, is set to ON for the water isotopologue tracers (see Jöckel et al., 2008). This applies the advection scheme for the tracers. The Lin and Rood advection scheme satisfies mass conservation, the consistency with the discretisation of the continuity equation, the monotonicity of the 1D advection schemes and the preservation of linear tracer correlations. A detailed description of this tracer advection, which was adapted from the ECHAM5 basemodel, is given in Roeckner et al. (2003).

### 3.3.5 Clouds - large-scale and convective

The cloud and convection parameterisation routines (CLOUD and CONVECT) in EMAC include a number of phase transitions and therefore several different fractionation effects. During the formation of clouds, condensation of water vapour to liquid water and deposition of vapour to cloud ice take place. For condensation within clouds, a closed system is assumed. The condensate is taken on to be in contact and hence in isotopic equilibrium with the surrounding vapour during the entire process. This also applies for the evaporation of cloud water, where, in contrast to evaporation from the ocean, also a closed system is assumed. An open system is used for the deposition of water vapour to ice. Due to the low diffusivities of the isotopologues in the ice phase, no exchange happens between ice and vapour. The effective fractionation factor (Eq. 2.26) is used here, including a function for the supersaturation  $S$  (see Sect. 2.2.2.2). Werner et al. (2011) adjusted this function to  $S = 1.01 - 0.0045 \cdot T_{cond}$  in order to attain realistic isotope ratios in Antarctic snow. The constants of this function are similar but not equal to those used in other recent studies (Lee et al., 2007; Tindall et al., 2009; Risi et al., 2010). Since the focus of the present study lies on the tropopause region, where also low temperatures have a major effect on kinetic fractionation through deposition, the values by Werner et al. (2011) have been taken. During the melting of ice and the freezing of water, no fractionation happens. Other in-cloud processes like sedimentation of ice, autoconversion, accretion and aggregation include no fractionation effects either.

The isotopic (non-)equilibrium  $\alpha_{eff}$  (Eq. 2.32) between a falling raindrop and the surrounding water vapour only adjusts after some time. This time is again dependent on the humidity, the temperature, the diffusivity of the water molecules and the droplet size. Since these processes are not resolved in GCMs the fractionation during reevaporation of raindrops falling through undersaturated air can only be approximated. Following Jouzel et al. (1987) and Hoffmann et al. (1998), an isotopical equilibration of 45% is assumed for large drops from convective rain and 95% for small drops falling from stratiform clouds. Due to their low exchange rates, snow and ice do not reequilibrate at all, which leads to more depleted isotope ratios in solid precipitation.

For each phase transition of water, the corresponding effects are implemented in the H2OISO submodel for the isotopologues. The precipitation fluxes, turbulence, cloud generation and dissipation, cloud ascent and descent, up- and downdrafts all contain phase

transitions. For all these processes, the current meteorological conditions (temperature, humidity, ...) have to be used to calculate the fractionation effects, and all these processes modify the latter.

Physically, three different scenarios are considered in the model to determine the isotope ratios: No fractionation, equilibrium fractionation and kinetic fractionation. Numerically, a tendency is calculated for each isotopologue in the concerning phase for the transition, which is later added to the total process tendency of the isotopologue. The calculation of the tendencies of the isotopologues are implemented in the code relative to the tendencies of regular water. For processes that do not contain fractionation, the isotope ratio of the product  $R_{pro}$  will be the same as for the precursor  $R_{pre}$ . The approach therefore is

$$R_{pre} = R_{pro} \quad (3.13)$$

which, with  $\xi$  representing the isotopologue,  $\psi$  the 'normal water' and  $\partial\xi/\partial t$  and  $\partial\psi/\partial t$  their respective tendency, gives

$$\frac{\xi - \frac{\partial\xi}{\partial t}}{\psi - \frac{\partial\psi}{\partial t}} = \frac{\frac{\partial\xi}{\partial t}}{\frac{\partial\psi}{\partial t}} \quad (3.14)$$

and thus

$$\frac{\partial\xi}{\partial t} = \frac{\partial\psi}{\partial t} \cdot \frac{\xi}{\psi}, \quad (3.15)$$

for the tendency of the isotopologue.

For equilibrium fractionation, Eq. 2.15 is used, which leads to

$$\frac{\xi - \frac{\partial\xi}{\partial t}}{\psi - \frac{\partial\psi}{\partial t}} = \alpha(T) \cdot \frac{\frac{\partial\xi}{\partial t}}{\frac{\partial\psi}{\partial t}}, \quad (3.16)$$

with the temperature dependent equilibrium fractionation factor  $\alpha$  from Eq. 2.16 to Eq. 2.19. This results in the isotopologue tendency

$$\frac{\partial\xi}{\partial t} = \frac{\partial\psi}{\partial t} \cdot \frac{\xi}{\alpha(T)\psi + \frac{\partial\psi}{\partial t}(1 - \alpha(T))}. \quad (3.17)$$

Kinetic fractionation requires the Rayleigh equation (Eq. 2.30). With

$$R = \frac{\xi - \frac{\partial\xi}{\partial t}}{\psi - \frac{\partial\psi}{\partial t}}, \quad (3.18)$$

$$R_0 = \frac{\xi}{\psi}, \quad (3.19)$$

$$N = \psi - \frac{\partial\psi}{\partial t} \quad \text{and} \quad (3.20)$$

$$N_0 = \psi, \quad (3.21)$$

the Rayleigh equation leads to

$$\frac{\xi - \frac{\partial \xi}{\partial t}}{\psi - \frac{\partial \psi}{\partial t}} = \frac{\xi}{\psi} \cdot \left( \frac{\psi - \frac{\partial \psi}{\partial t}}{\psi} \right)^{\tilde{\alpha}-1}. \quad (3.22)$$

Here the kinetic fractionation factor  $\alpha$  has to be replaced by  $\tilde{\alpha}$ , which represents an average of  $\alpha$  over the time step.  $\alpha$  is valid only for an infinitesimally short time. For the tendency of the isotopologue, this results in

$$\frac{\partial \xi}{\partial t} = \xi \cdot \left[ 1 - \left( 1 - \frac{\frac{\partial \psi}{\partial t}}{\psi} \right)^{\tilde{\alpha}} \right]. \quad (3.23)$$

For ‘normal’ water, respectively the HHO tracers, these calculations are performed in the same manner. Applying the value 1 for the fractionation factors leads to

$$\frac{\partial \xi}{\partial t} = \frac{\partial \psi}{\partial t} \cdot \frac{\xi}{\psi} \quad (3.24)$$

for all the calculations of the tendency. Considering that one has  $\xi = \psi$  for HHO, the tendency for the HHO tracer equals the tendency of the corresponding state variable ( $\partial \xi / \partial t = \partial \psi / \partial t$ ).

The EMAC model provides the possibility to use several different convection schemes. In this work, the H2OISO submodel has been equipped with only the three Tiedtke (“Tiedtke-Nordeng”, “Tiedtke” and “Tiedtke-Hybrid”) convection schemes (Tiedtke, 1989). In all the simulations conducted for this study the “Tiedtke-Nordeng” scheme was applied.

### 3.3.6 Methane oxidation

The EMAC model contains the submodel CH<sub>4</sub>, taking the water vapour production through methane oxidation (see Sect. 2.1.2) into account. It includes a tracer for methane (the CH<sub>4</sub> tracer), which experiences a source from the surface (here as lower boundary conditions from the submodel TNUDGE, see Sect. 3.4; alternatively as methane fluxes, provided by the submodel OFFEMIS (see Jöckel et al., 2010)) and a sink from methane oxidation. Solutions are calculated for the four oxidation reactions (Eq. 2.2 to Eq. 2.5). These are determined by the mixing ratios of the three oxidation partners chlorine (Cl), the hydroxyl radical (OH) and excited oxygen (O(<sup>1</sup>D)) and the photolysis rate. The photolysis rate  $j_{CH_4}$  ( $= r_{h\nu}$ ) is here calculated in the MESSy submodel JVAL (for details, see Landgraf and Crutzen, 1998) and passed on to CH<sub>4</sub> (alternatively it can be prescribed). The rates for the oxidation of methane with the reaction partners Cl, OH and O(<sup>1</sup>D) are calculated within CH<sub>4</sub>. Firstly, the first order reaction coefficients  $k_{OH}$  for OH,  $k_{Cl}$  for Cl and  $k_{O1D}$  for O(<sup>1</sup>D) are determined. While  $k_{O1D} = 1.75 \cdot 10^{-10} \text{ cm}^3/\text{s}$  is constant,  $k_{OH}$  and  $k_{Cl}$  (in  $\text{cm}^3/\text{s}$ ) are temperature ( $T$  in K) dependent and are computed by

$$k_{OH} = 1.85 \cdot 10^{-20} \cdot \exp \left( 2.82 \cdot \log(T) - \frac{987}{T} \right) \quad (3.25)$$



and

$$k_{Cl} = 6.6 \cdot 10^{-12} \cdot \exp\left(-\frac{1240}{T}\right). \quad (3.26)$$

Subsequently, the rates for the reactions with methane are

$$r_{O1D} = k_{O1D} \cdot c_{air} \cdot O(^1D) \quad (3.27)$$

$$r_{Cl} = k_{Cl} \cdot c_{air} \cdot Cl \quad (3.28)$$

$$r_{OH} = k_{OH} \cdot c_{air} \cdot OH, \quad (3.29)$$

with  $O(^1D)$ ,  $Cl$  and  $OH$  representing the mixing ratios (in  $mol/mol$ ) of the respective species and  $c_{air}$  the concentration of air (in  $cm^{-3}$ ), which is calculated by

$$c_{air} = \frac{N_A \cdot 10^{-6} \cdot p}{R_{gas} \cdot T \cdot \left[1 + \left(\frac{M_{air}}{M_{H_2O}} - 1\right) \cdot Q\right]}. \quad (3.30)$$

Here  $N_A$  denotes the Avogadro Constant ( $6.022045 \cdot 10^{23} \text{ mol}^{-1}$ ),  $p$  the pressure (in Pa),  $R_{gas}$  the universal gas constant ( $8.314409 \text{ J/K/mol}$ ),  $T$  the temperature (in K),  $M_{air}$  the molar mass of dry air ( $28.97 \text{ g/mol}$ ),  $M_{H_2O}$  the molar mass of water ( $18.02 \text{ g/mol}$ ) and  $Q$  the specific humidity (in  $kg/kg$ ).

The tendency for the methane tracer (in  $mol/mol/s$ ) is then given by

$$\frac{\partial(CH_4)}{\partial t} = -1 \cdot CH_4 \cdot (r_{O1D} + r_{Cl} + r_{OH} + r_{hv}), \quad (3.31)$$

where  $CH_4$  is the methane mixing ratio (in  $mol/mol$ ) of the previous time step and the  $-1$  accounts for the fact that this is a pure sink reaction for the methane tracer. To calculate the tendency for the specific humidity due to methane oxidation

$$\left. \frac{\partial Q}{\partial t} \right|_C = \frac{-2 \cdot \frac{\partial(CH_4)}{\partial t}}{\frac{M_{air}}{M_{H_2O}} \left(\frac{1}{1-Q}\right)^2} \quad (3.32)$$

is applied. The subscript  $C$  denotes, that this is the chemical tendency of  $Q$ . This division is to convert the tendency from  $mol/mol/s$  to  $kg/kg/s$ . The negative sign here accounts for the fact that methane oxidation is a source for water vapour and the factor 2 for the reaction of the four hydrogen atoms of one methane molecule into two water molecules.

Analogously, a parameterisation for the oxidation of the  $CH_3D$  molecule has been devised here.  $CH_3D$  can be seen as the isotopological counterpart in methane to HDO in water, containing one deuterium atom instead of one of the hydrogen atoms. Another tracer was included for this purpose, the  $CH_3D$  tracer. The methane oxidation reactions (Eq. 2.2 to Eq. 2.5) are modified simply by exchanging  $CH_4$  with  $CH_3D$  on the left hand side and  $H_2O$  with HDO on the right hand side. Additionally, fractionation is applied for

the calculation of the reaction rates. As mentioned above, fractionation processes in chemical reactions are treated as kinetic effects. Hence the Rayleigh equation (Eq. 2.33) has to be applied and transformed to the form of Eq. 3.23 for the implementation. Inserting the isotope ratios

$$R = \frac{CH_3D - \frac{\partial(CH_3D)}{\partial t}}{CH_4 - \frac{\partial(CH_4)}{\partial t}} \quad (3.33)$$

before and

$$R_0 = \frac{CH_3D}{CH_4} \quad (3.34)$$

after the reaction and the total mixing ratios

$$N = CH_4 - \frac{\partial(CH_4)}{\partial t} \quad \text{and} \quad (3.35)$$

$$N_0 = CH_4 \quad (3.36)$$

to Eq. 2.33, this leads to

$$\frac{CH_3D - \frac{\partial(CH_3D)}{\partial t}}{CH_4 - \frac{\partial(CH_4)}{\partial t}} = \frac{CH_3D}{CH_4} \left( \frac{CH_4 - \frac{\partial(CH_4)}{\partial t}}{CH_4} \right)^{\text{KIE}^{-1}-1} \quad (3.37)$$

and therefore the tendency for the  $\text{CH}_3\text{D}$  tracer through oxidation is

$$\frac{\partial(CH_3D)}{\partial t} = CH_3D \left[ 1 - \left( 1 - \frac{\partial(CH_4)}{\partial t} \right)^{\text{KIE}^{-1}} \right]. \quad (3.38)$$

Using Eq. 3.31 for  $\partial(CH_4)/\partial t$  and considering that the KIE is different for each of the reactions (see Sect. 2.1.2), the equation has to be split into four addends:

$$\frac{\partial(CH_3D)}{\partial t} = CH_3D \left[ \left( 1 - (1 + r_{OH})^{\text{KIE}_{OH}^{-1}} \right) + \left( 1 - (1 + r_{Cl})^{\text{KIE}_{Cl}^{-1}} \right) + \left( 1 - (1 + r_{O1D})^{\text{KIE}_{O1D}^{-1}} \right) + \left( 1 - (1 + r_{h\nu})^{\text{KIE}_{h\nu}^{-1}} \right) \right]. \quad (3.39)$$

In order to calculate the tendency of the HDO tracer from the tendency of the  $\text{CH}_3\text{D}$  tracer (i.e. the chemical tendency of HDO), analogously to Eq. 3.32,

$$\left. \frac{\partial(HDO)}{\partial t} \right|_C = \frac{-1 \cdot \frac{\partial(CH_3D)}{\partial t}}{\frac{M_{air}}{M_{HDO}} \left( \frac{1}{1 - HDO} \right)^2}, \quad (3.40)$$

is applied. With the differences to use the mixing ratio and the molar mass of HDO ( $M_{HDO} = 19.02$  g/mol) instead of Q and  $M_{H_2O}$  and  $-1$  instead of  $-2$ , because the oxidation of one  $CH_3D$  molecule can only produce one HDO molecule. Emissions of  $CH_3D$  could be defined with the aid of the isotope scheme of Gromov et al. (2010). However, this task goes beyond the scope of this study, which mainly focuses on stratospheric and upper tropospheric processes. This leads to another simplification: In accordance with Ridal and Siskind (2002) the isotopic ratio of methane was fixed to  $-68\%$  below 500 hPa. This is the climatological  $\delta D(CH_4)$  value (note, that  $\delta D(CH_4)$  here also bases on VSMOW), which methane possesses, when entering the stratosphere in the tropics.

Note, that this simple parameterisation neglects a number of effects that may be important for the chemical production of HDO: Firstly, the other, rather rare methane isotopologues  $CH_2D_2$ ,  $CHD_3$  and  $CD_4$ , as well as the reaction partner OD (an isotopologue of the hydroxyl radical) are not considered. Secondly, the entire cycle of molecular hydrogen and its isotopologue HD (see Sect. 2.2.4) are not taken into consideration. The intermediate reactions between  $CH_3D$  and HDO involving HD also include fractionation effects (see e.g. Röckmann et al., 2003; Rhee et al., 2006). Most of these, however, are poorly quantified (Zahn et al., 2006) and therefore neglected for this study. These simplifications have to be kept in mind when evaluating the isotope ratios in the stratosphere.

## 3.4 Setup of the model simulations

Two different EMAC model simulations with the H2OISO submodel in different resolutions and setups were carried out for this study. The setup of the simulation in low resolution, (T31L39MA) which is described in the next section, is only used for the evaluation of the model in the troposphere. It contains no stratospheric chemistry for water vapour and its isotopologues. In the subsequent section (Sect. 3.4.2), the setup of the simulation in high resolution (T42L90MA) is presented. The results of this simulation are used for the evaluation in the troposphere, in the stratosphere and furtheron for the analysis.

### 3.4.1 The T31L39MA simulation (FREE\_VAL) setup

The EMAC model simulation FREE\_VAL was conducted in the T31L39MA resolution. That corresponds to an approximate grid box size of  $3.75^\circ$  and 39 vertical layers, with middle atmosphere dynamics. The time step of the simulation was twelve minutes and the output was set to produce averaged values for each month. No explicit chemical production of water vapour and its isotopologues was activated for this simulation. Due to the very small mixing ratios of water vapour in the stratosphere, however, the chemical contribution is negligible when analysing tropospheric isotope ratios. The uppermost model layer was centred around 0.01 hPa. Additionally to the ECHAM5 basemodel and the H2OISO submodel, the MESSy submodels used for this simulation were: CLOUD, CONVECT, CVTRANS, GWAVE, RAD4ALL and TROPOP (for details, see Jöckel et al., 2010, and citations therein). As boundary condition, the monthly averages of the climatological sea surface temperatures and sea ice conditions (AMIP-II; Hurrell et al., 2008) of the period from 1987 to 2006 were used repeatedly for every year. This simulation was performed in “free running” mode, i.e., without Newtonian relaxation to meteorological reference data.

The simulation was started in the year 1998 for a 15 year period. The first five years are considered as the spin-up period and therefore not taken into account for the evaluation.

### 3.4.2 The T42L90MA simulation (SD\_REF) setup

For the EMAC model simulation SD\_REF, the T42L90MA resolution was chosen, which corresponds to an approximate grid box size of  $2.8^\circ$ , 90 vertical layers and explicitly resolved stratospheric dynamics. The uppermost model layer was centred around 0.01 hPa, as well. In this simulation, the H2OISO submodel plus the following MESSy submodels were used: CLOUD, CONVECT, CVTRANS, GWAVE, RAD4ALL, TROPOP, CH4, JVAL, ORBIT, SORBIT, TNUDGE (for details, see Jöckel et al., 2010, and citations therein). The time step of the simulation was twelve minutes and the output was set to produce instantaneous values with an interval of eleven hours. In this simulation, the chemistry parameterisation for HDO and CH<sub>3</sub>D, which was described in Sect. 3.3.6, was used. Before starting the actual simulation, a 20 year simulation, with “free running” conditions (as in the FREE\_VAL simulation) was carried out to obtain steady-state initial values for water, methane and their isotopologues. From these initial conditions, a simulation with specified dynamics (i.e. in nudged mode) was started. This implies a Newtonian relaxation of the divergence, the vorticity, the temperature and the logarithm of the surface pressure towards reference data. Here the relaxation was performed up to 1 hPa and the ERA-INTERIM reanalysis data (ECMWF Dee et al., 2011) was used for this purpose. This guarantees, that not only the climatic state, but also the meteorological situation of the model simulation corresponds to the actual dates. This allows a direct comparison of the model results with data sets, such as from satellite or in situ measurements. The simulation starts at the beginning of the year 1982 and terminates at the end of the year 2011. From the steady-state conditions, which are used for the initialisation, the model again needs several years to adjust to the conditions of the nudged mode. The first eight years are hence not considered for the analysis. Only the 21 years from 1990 until 2011 are evaluated. Transient greenhouse gas concentrations were prescribed throughout the atmosphere. Methane is prescribed at the lower boundary through the submodel TNUDGE, based on observations. The mixing ratios of OH, Cl, O(<sup>1</sup>D) are prescribed (monthly averages) from a previous “nudged”, transient EMAC simulation with full chemistry. The same applies for ozone, which is needed to calculate the photolysis rate in the submodel JVAL. The methane oxidation is calculated in the CH4 submodel, as described in Sect. 3.3.6.

# Chapter 4

## Evaluation of the H2OISO submodel

### 4.1 Correctness of the second hydrological cycle

Since the hydrological cycle within the EMAC H2OISO submodel is implemented independently from the actual hydrological cycle in the EMAC model, its correctness has to be guaranteed before applying it. To ensure this prerequisite the  $HHO_{vap}$ ,  $HHO_{liq}$  and  $HHO_{ice}$  tracers are used, since these represent 'normal' water and hence have to exactly reproduce the standard ECHAM variables  $Q$ ,  $XL$  and  $XI$ . The strategy to assure that all processes are computed identically for the three tracers and the three variables is presented in the next section. Due to the coding method, however, small numerical errors occur. Their origin is described. As these numerical errors eventually lead to divergence of the two hydrological cycles, a special error correction was introduced. In Sect. 4.1.2 an analysis of the numerical error is presented, which confirms that the numerical error is negligible for the calculation of the isotopologues.

#### 4.1.1 Correctness of individual processes and the numerical error

With the assistance of the TENDENCY submodel, a stepwise strategy could be applied to ensure the correctness of the second hydrological cycle. The processes that modify the variables  $Q$ ,  $XL$ ,  $XI$  in the EMAC model in the order of calling within a timestep are: ADVECT, VDIFF, CONVECT, CLOUD. It had to be assured that the difference of the individual process tendencies between  $Q$  and  $HHO_{vap}$ ,  $XL$  and  $HHO_{liq}$  and  $XI$  and  $HHO_{ice}$ , respectively, are zero. By testing this in the given order of processes starting at the first model time step, certainty about the correctness of each process in the hydrological cycle could be achieved. This test was performed for several time steps after initialising the model and also after a model restart.

Due to numerical issues, a small error, or rather difference, however, occurs in some parts of the model code. As described in Sect. 3.3 in the H2OISO submodel, the implementation of the HHO tracers is conducted alike the implementation of the water isotopologue tracers with a fractionation factor of one. Analytically, this always results in  $\Delta\xi_{HHO} = \Delta\psi$ , where  $\Delta\xi_{HHO}$  represents the tendencies of the HHO tracers ( $\xi_{HHO} \in \{HHO_{VAP}, HHO_{LIQ}, HHO_{ICE}\}$ ) and  $\Delta\psi$  the tendencies of the water vapour, liquid water and ice water contents ( $\psi \in \{Q, XL, XI\}$ ), respectively, of the actual hydrological cycle.

Numerically, however, this is not necessarily the case. Numerical rounding at the last decimal place during the individual calculations of the procedure can lead to small differences. The variables are then used for further calculations and also affect other grid boxes, thus the differences can accumulate thereafter.

To prevent the differences from becoming too large and hence the two hydrological cycles from diverging, a correction at the end of each timestep was introduced for the HHO tracers in the H2OISO submodel. For this, the additional tendency  $\Delta\xi_{numer}$  is calculated for the three HHO tracers. It is given by

$$\Delta\xi_{numer} = \Delta\psi - \Delta\xi_{HHO}. \quad (4.1)$$

This tendency is then added to the  $\Delta\xi_{HHO}$  via TENDENCY to equalise  $\Delta\psi$  and  $\Delta\xi_{HHO}$ .

#### 4.1.2 Analysis of the numerical error

Analysis of the numerical error can be made for each time step. The model simulation SD\_REF in T42L90MA resolution (details are given in Sect. 3.4.2) was used for this. The maximum values of the absolute errors  $A_E = |\Delta\xi_{numer}| = |\Delta\psi - \Delta\xi_{HHO}|$  per timestep for all grid boxes are at the order of  $10^{-20}$  kg/kg/s for water vapour and  $10^{-22}$  kg/kg/s for liquid water and ice.

The error correction can only be performed for the 'normal' water and not for the isotopologues, for the simple reason, that there is no "true" value for the tendency of the isotopologues, like there is for 'normal' water, with  $\Delta\psi$ . Since the tendencies of the isotopologues are very small, it is questionable if the numerical errors are still too large and can significantly deteriorate their results. The computation of a relative error has been introduced for this evaluation. Assuming that the error being made for the isotopologue HDO is comparable to the absolute numerical error  $A_E$  for 'normal' water ( $|\Delta\xi_{HDO} - \Delta\psi_{HDO}| \approx |\Delta\xi_{HHO} - \Delta\psi|$ , where  $\Delta\psi_{HDO}$  stands for the hypothetical correct tendency of HDO), which in fact overestimates the error by around three orders of magnitude, the equation

$$R_{E,\psi} = \frac{|\Delta\xi_{HHO} - \Delta\psi|}{|\Delta\xi_{HDO}|} \quad (4.2)$$

yields the relative error  $R_E$ . This provides a value to estimate the influence of the numerical error on the HDO tendency. The maximum values of the relative numerical error of all grid boxes for one year of the simulation after each time step is shown in Fig. 4.1. The maximum values of  $R_E$  for water vapour during that year are at the order of  $2 \cdot 10^{-4}\%$ ,  $3 \cdot 10^{-6}\%$  for liquid water and  $8 \cdot 10^{-6}\%$  for the solid phase of water. This certifies that the numerical error is negligible for the results of the isotopologue tendencies.

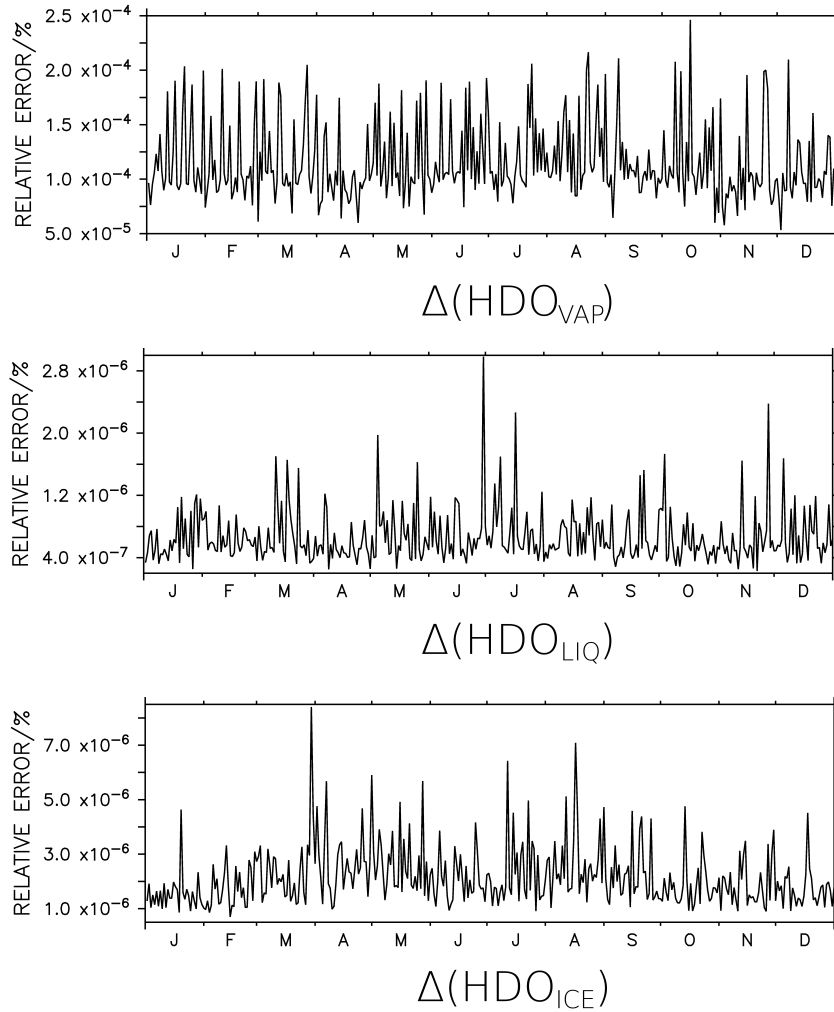


Figure 4.1: Relative numerical error in the water isotopologue HDO for vapour, liquid water and ice for one year of the SD-REF simulation.

## 4.2 Evaluation of tropospheric isotope quantities

Before applying the EMAC H2OISO submodel in the stratosphere an evaluation of the physical processes in the troposphere was conducted. As explained in Sect. 2.2.5 the isotopic composition in precipitation comprises the possibility to conclude various fractionation processes. Hence the representation of the isotope physics in the model can be evaluated by examining the isotope ratios in precipitation. The two model simulations, described in Sect. 3.4, were used for this evaluation. The GNIP (Global Network of Isotope in Precipitation) data set is used for comparison of the model results in Sect. 4.2.1 and results of the ECHAM5-wiso model are consulted in Sect. 4.2.2. Based on these comparisons, the conclusion, that the H2OISO submodel within the framework of the EMAC model is representing the state of the art of GCMs for stable water isotopologues in the tropospheric hydrological cycle, is drawn in Sect. 4.2.3.

### 4.2.1 Comparison with GNIP data

The International Atomic Energy Agency (IAEA) and the World Meteorological Organisation (WMO) started GNIP in 1961. Since its start, more than 800 meteorological stations in 101 countries have collected samples of the water isotopologues HDO and  $\text{H}_2^{18}\text{O}$  in precipitation (IAEA, 2009). Some of these stations provided monthly precipitation measurements for several decades, most of them, however, operated for a much shorter period, only. The data set is freely accessible from IAEA (2001) and serves as a basis for the evaluation of the simulated isotope ratios.

Fig. 4.2 shows the annual averages of  $\delta^{18}\text{O}(\text{H}_2\text{O})$  in precipitation from the FREE\_VAL (a) and the SD\_REF (b) simulations, the GNIP database (c), and the absolute differences between the respective simulation and the GNIP data (d and e). Panel c is taken from IAEA (2001), it was elaborately processed by using inter- and extrapolating methods for selected stations (for details see IAEA, 1992). For panel (d) and (e), the annual values of the entire GNIP database (from IAEA, 2001) were mapped to the respective model grid and subsequently the absolute value of the difference between the GNIP and the EMAC data was calculated. The same applies for panels (a) to (d) of Fig. 4.3, where the annual averages and absolute differences of  $\delta\text{D}(\text{H}_2\text{O})$  in precipitation are presented.

Apart from the much lower values of  $\delta\text{D}(\text{H}_2\text{O})$ , compared to  $\delta^{18}\text{O}(\text{H}_2\text{O})$ , which is due to the stronger fractionation in HDO (explained in Sect. 2.2.2.1), the panels (a) and (b) of Fig. 4.2 and Fig. 4.3 show the same patterns. A transition from high values of up to 0‰ in the tropics to low values below  $-230$ ‰ in  $\delta\text{D}(\text{H}_2\text{O})$  and  $-30$ ‰ in  $\delta^{18}\text{O}(\text{H}_2\text{O})$  in the Arctic regions, associated with stronger fractionation at lower temperatures can be seen in the panels (a) to (c) in both figures. The orographic effect is obvious, e.g., over the Rocky Mountains in North America and the continental effect is evident in Greenland and in the northeast of Siberia. Also, the amount effect can be seen in the tropical regions, for example at the west coast of South America. All these features correspond well between model and measurements. On the model grid, only small deviations can be observed between the two model simulations of different resolution in the panels (a) and (b).

Panels (d) and (e), in both figures, provide a more quantitative estimate of the differences between the simulations and the measurements. Large differences are obvious in certain regions. The northern regions of Canada and Greenland show considerable deviations. Here, a general discordance of the precipitation amount and the annual cycle, between model and reality (see Hagemann et al., 2005) can easily cause the deviations in the isotope ratios, because the general amount of precipitation is very low. Large deviations between EMAC and GNIP can also be observed in the Asian mountains. This can be explained by the poor representation of the model orography in the here applied horizontal resolutions. The altitude and also lee and luff effects can hence not be properly represented. Slight improvements in that respect can already be seen in the T42L90MA resolution compared to the T31L39MA resolution. Another large difference can be observed in South Africa, especially in  $\delta\text{D}(\text{H}_2\text{O})$ , a dynamic effect is not as easily attributable for this deviation. It, however, also improves with increased model resolution.



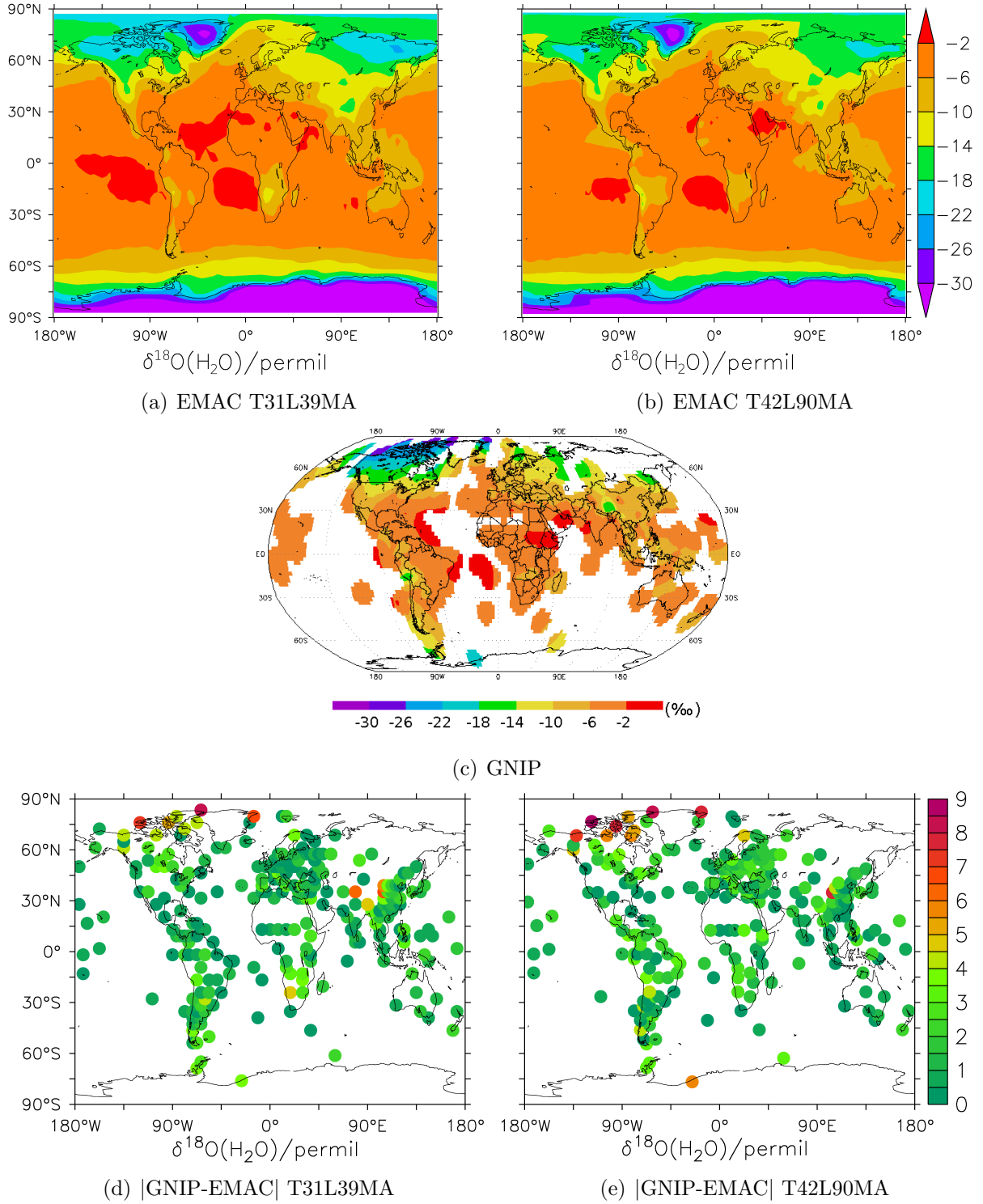


Figure 4.2:  $\delta^{18}\text{O}(\text{H}_2\text{O})$  in precipitation. EMAC, GNIP and the absolute values of GNIP minus EMAC. EMAC simulations are averaged over the entire available period of the FREE\_VAL (a) and the SD\_REF (b) simulation. The GNIP data image is taken from IAEA (2001). The absolute differences between GNIP and EMAC are shown in panel (d) for the FREE\_VAL and in panel (e) for the SD\_REF simulation.

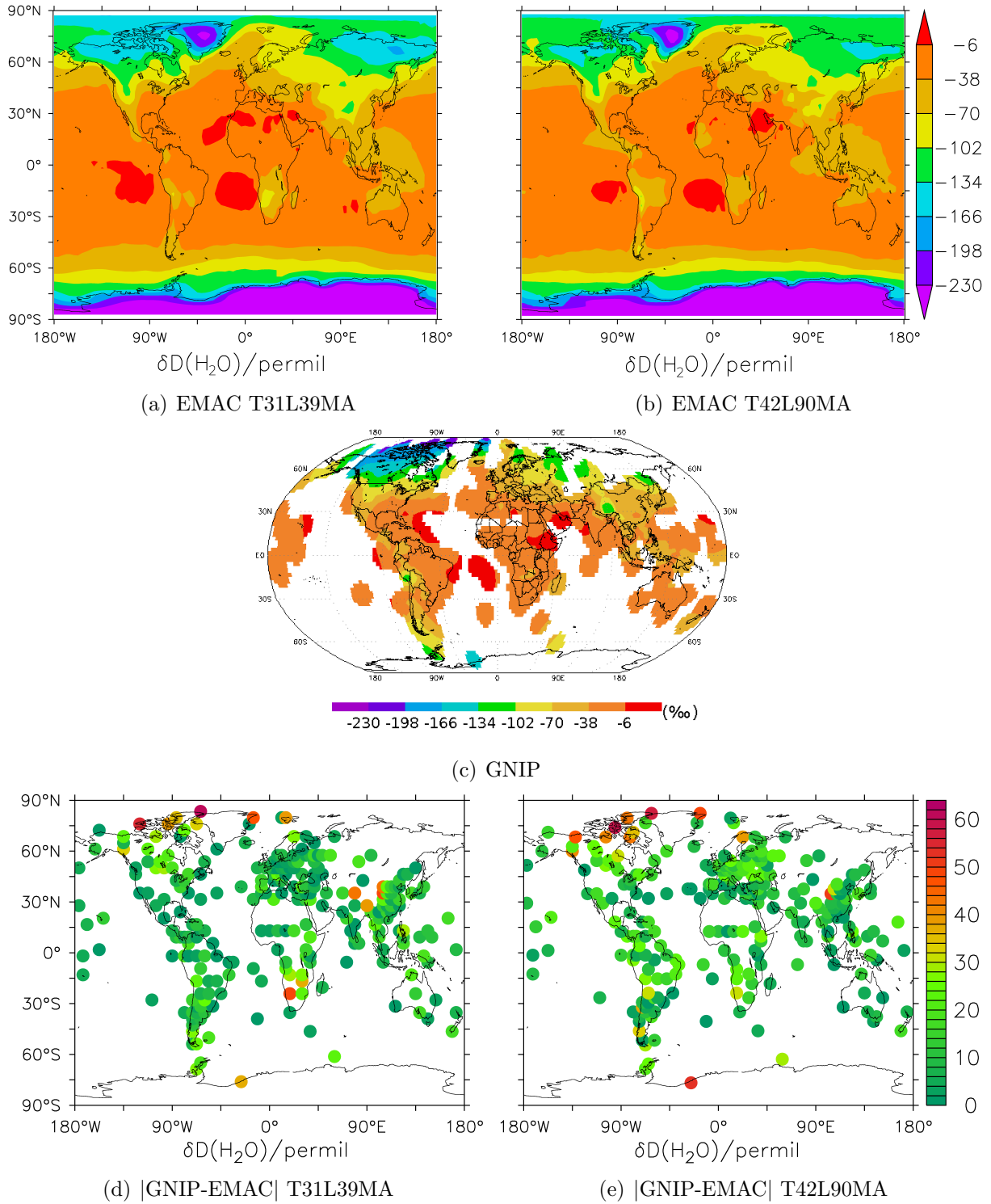


Figure 4.3:  $\delta D(H_2O)$  in precipitation. EMAC, GNIP and the absolute values of GNIP minus EMAC. EMAC simulations are averaged over the entire available period of the FREE\_VAL (a) and the SD\_REF (b) simulation. The GNIP data image is taken from IAEA (2001). The absolute differences between GNIP and EMAC are shown in panel (d) for the FREE\_VAL and in panel (e) for the SD\_REF simulation.

In order to provide an estimate of the representation of the seasonal cycle of  $\delta D(H_2O)$  in precipitation between the GNIP measurements and the EMAC model, the monthly averages of the respectively available periods are compared in Fig. 4.4. For that, particular regions of different climate zones have been defined, chosen to include as many GNIP stations as possible. The defined regions can be seen in the upper left panel of the figure, which also includes the absolute differences of  $\delta D(H_2O)$  in precipitation from Fig. 4.3(e). The regions are labeled with (A) for northern Canada and Greenland, (B) for the Caribbean and parts of Middle and South America, (C) for Patagonia, (D) for Central Europe, (E) for the Middle East, (F) for South Africa and (G) for the eastern parts of China. Additionally to the averages of the monthly averages, the interannual standard deviations are included for the two model simulations to provide an estimate of the variation of  $\delta D(H_2O)$ .

In general the seasonal cycles of the measurements and the simulations correlate well. Some of the regions, however, show large offsets, partly during the entire year, partly during specific seasons. In most cases, the simulation with higher resolution (T42L90MA, green) is closer to the GNIP data, some panels, though, show the opposite. This is likely to be due to the different climatic states of both simulations, since the overall temperatures in the T42L90MA simulation are slightly higher than in the T31L39MA simulation and the temperatures determine the strength of the fractionation.

The Arctic region (A), which shows the largest annual offsets, shows larger deviations in winter than in summer. This is when stronger fractionation occurs due to the lower temperatures and the increased occurrence of solid precipitation. Surprisingly, the deviations are higher for the simulation with higher horizontal resolution. Region (C), which is also situated at higher latitudes, shows too high values in the model simulation, as well. The tropical region shown in panel (B), exhibits considerable improvement with increased horizontal resolution. The here predominate convective precipitation depends strongly on the latter. The seasonal cycle of model and GNIP data agree well in Central Europe (D). The generally higher isotope ratios in the model in this region, may be the influence of the effect of the Alps, which is not properly represented in the model. The subtropical regions (E) and (F) feature better agreement between simulations and measurements during winter, when the general amount of precipitation is higher. During the rather dry summer month, also the variation in the simulations is considerably higher. Panel (G) shows a good agreement of the seasonal cycle between measurements and model simulations, with a constant offset in the low resolution simulation. This improvement with increasing resolution is likely to be due to the more realistic orography, since the selected region features a distinct relief.

Similar evaluations have been conducted, e.g., by Risi et al. (2010) for the LMDZ-iso model and by Werner et al. (2011) for the ECHAM5-wiso model, albeit, by comparing individual stations instead of regions. These results also feature a qualitative good agreement with quantitatively comparable deviations in certain climate zones.

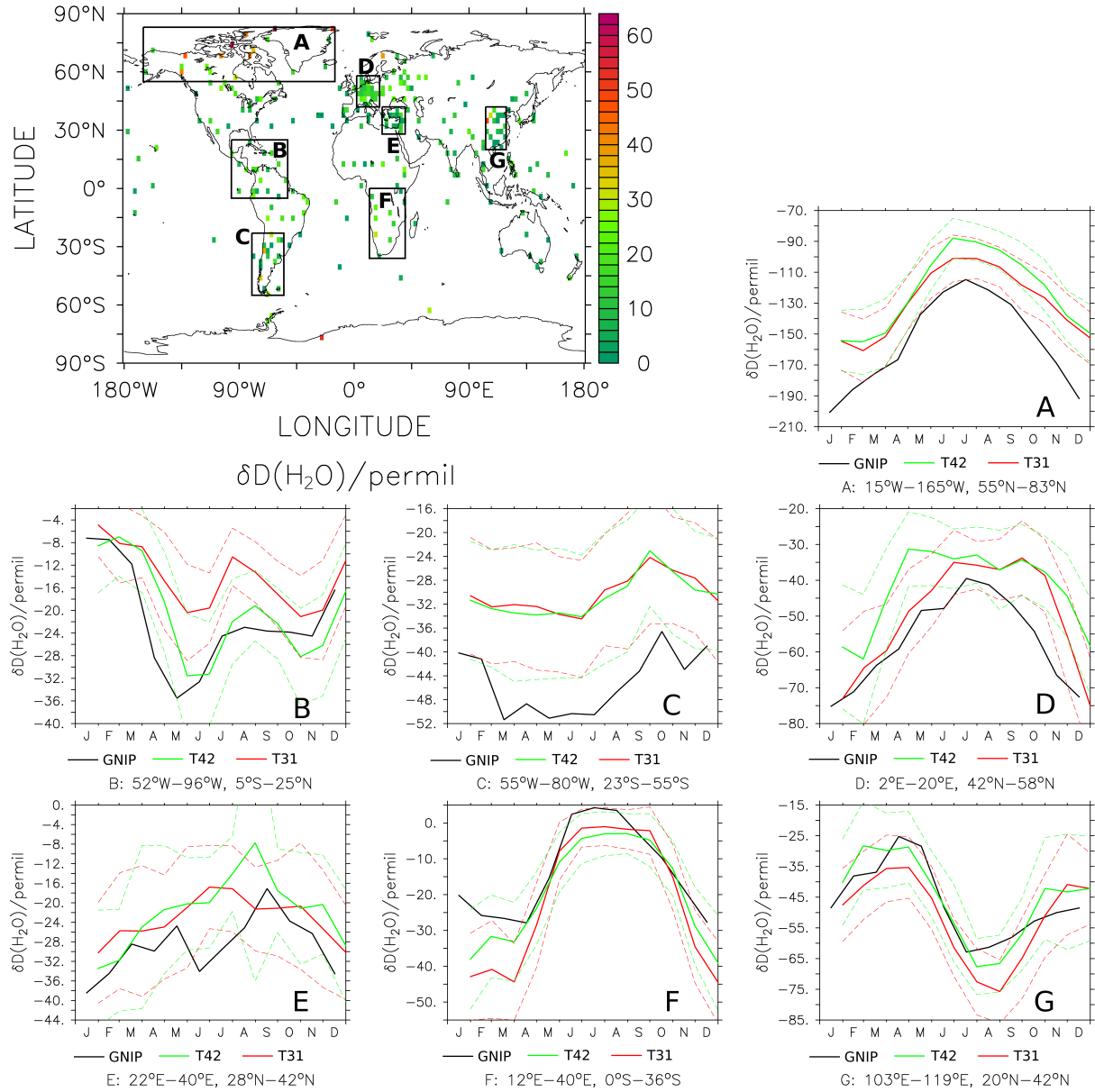


Figure 4.4: Comparison of the seasonal cycle of  $\delta D(H_2O)$  in precipitation between GNIP data and the two EMAC simulations (FREE\_VAL and SD\_REF) for selected regions. The map shows the difference between GNIP and EMAC from Fig. 4.3(e) and the selected regions (A to G), and the individual panels show averages of monthly averages of the three data sets and the interannual standard deviations (dashed lines) for the two model simulations.

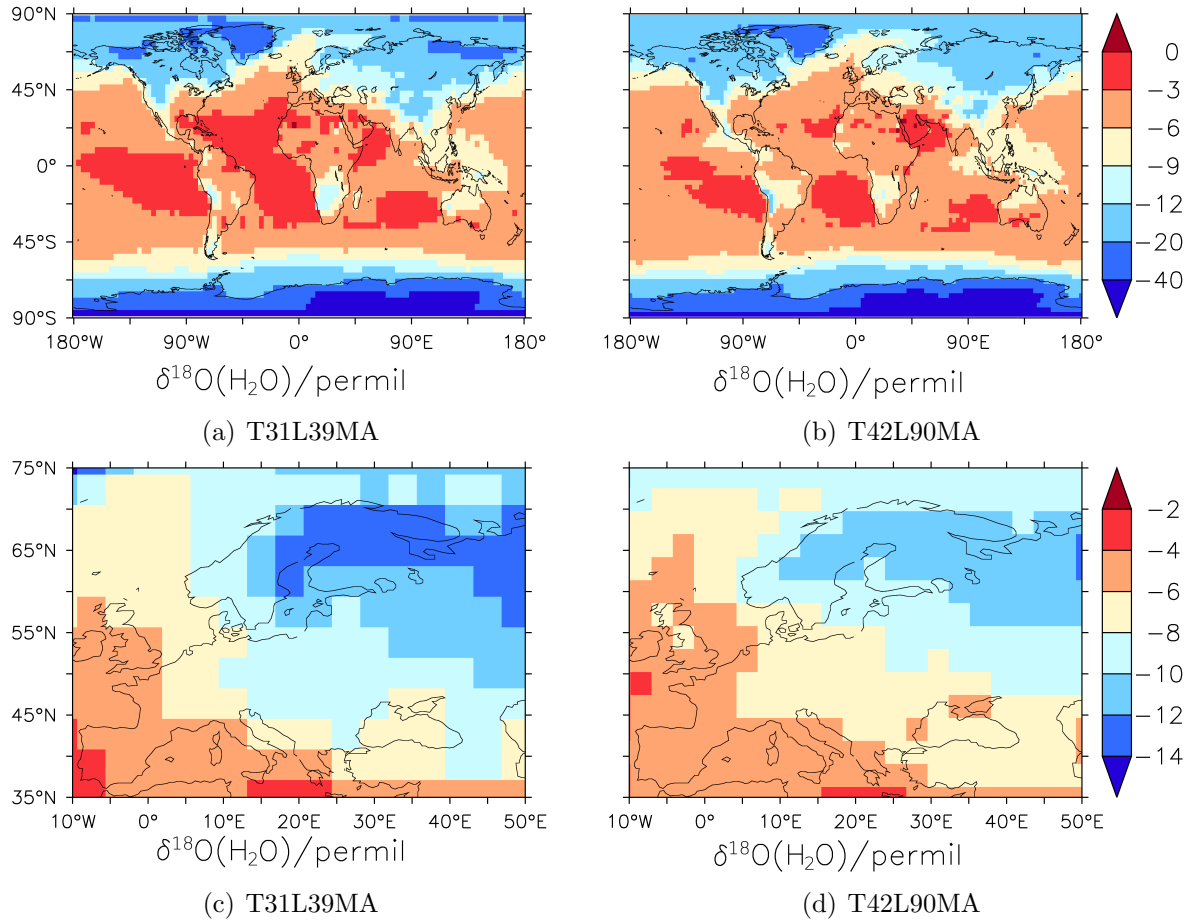


Figure 4.5: Annual  $\delta^{18}\text{O}(\text{H}_2\text{O})$  in precipitation for the entire available simulation period of FREE\_VAL (a and c) and SD\_REF (b and d), presented globally (a and b) and for Europe (c and d).

#### 4.2.2 Comparison with the ECHAM5-wiso model

As indicated in Tab. 3.2, a number of GCMs have been equipped with stable water isotopologues. One of the most recent and the most similar to H2OISO in EMAC is ECHAM5-wiso by Werner et al. (2011), which has been evaluated against GNIP data in the model resolutions T31L19, T63L31 and T159L31. The model resolutions, which were chosen for this study (T31L39MA and T42L90MA) compare best to the lowest resolution of Werner et al. (2011). Fig. 4.5 shows the annual averages of  $\delta^{18}\text{O}(\text{H}_2\text{O})$  in precipitation over the respectively available simulation period, globally in panel (a) for T31L39MA and (b) for T42L90MA and for Europe in panel (c) for T31L39MA and (d) for T42L90MA. The data is displayed identically to the figures of the study by Werner et al. (2011), which are displayed in Fig. 4.6.

The general patterns and values of the figures agree very well with the ECHAM5-wiso simulations. Especially the ECHAM5-wiso T31L19 simulation shows almost identical results as the FREE\_VAL simulation. As expected, for the isotope ratios in precipitation, the representation of the stratosphere and lower mesosphere has little effect, only. The small differences, however, originate mainly from the different boundary conditions, i.e.

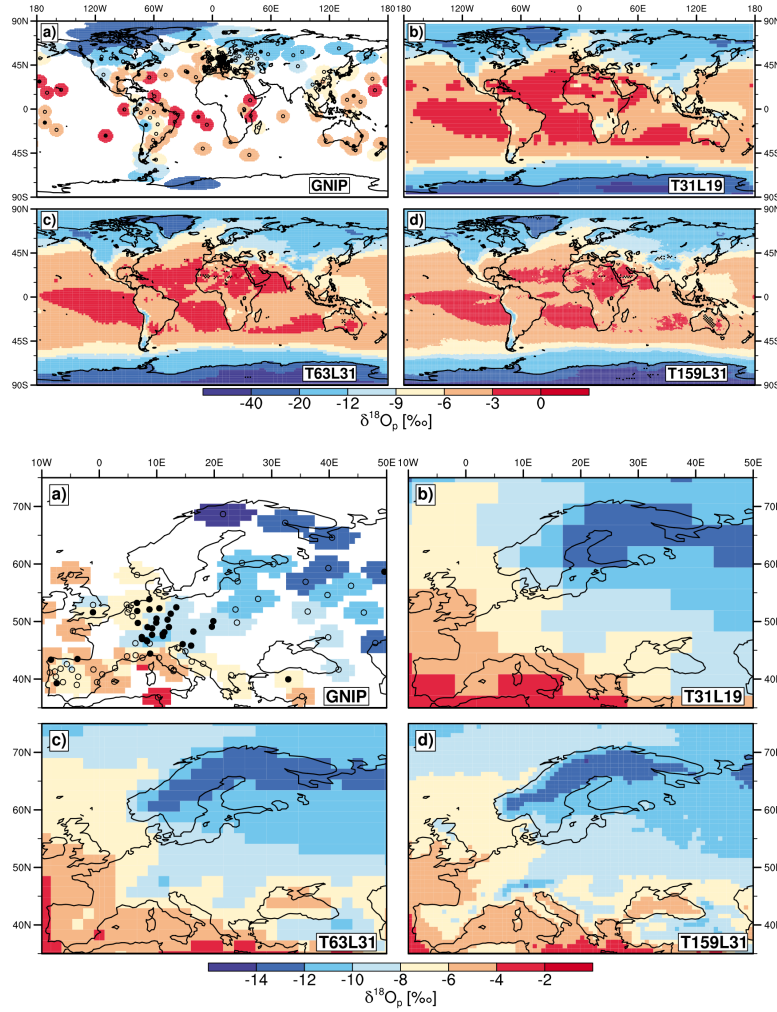


Figure 4.6: Measurements of selected GNIP stations (a) and ECHAM5-wiso results (b,c,d) of annual  $\text{H}_2^{18}\text{O}$  in precipitation in three different resolutions (T31L19, T63L31, T159L31) (Werner et al., 2011)

the sea surface temperatures (SSTs). The T42L90MA simulation of EMAC fits in, as an intermediate result between the T31L19 and the T63L31 simulations of ECHAM5-wiso. Some of the features, like the amount effect on the west coast of South America and the altitude effect on the Tibetan Plateau are already represented better than in the T31L19 resolution. However, the results of the ECHAM5-wiso simulations with T63L31 and T159L31 resolution in Werner et al. (2011) show these patterns even more pronounced. The zoom on Europe constitutes only little differences between the two EMAC simulations. The T42L90MA resolution is horizontally still not detailed enough to represent orographic features like the altitude effect in the Alps, which can be observed in the T63L31 and the T159L31 resolution of the ECHAM5-wiso study. The low  $\delta^{18}\text{O}(\text{H}_2\text{O})$  values in Scandinavia and western Russia can not be seen as pronounced anymore in the simulation with higher resolution. Since this feature becomes more distinct with higher resolution in the ECHAM5-wiso study, this is surprising, but can be explained with the generally warmer conditions in this region in the SD\_REF simulation. The general overestimation of the  $\delta^{18}\text{O}(\text{H}_2\text{O})$  values



of the model in northern Canada and Greenland, compared to the GNIP measurements is a feature in all the model simulations, including all the resolutions of the ECHAM5-wiso model. Hence, this may be associated with a general dynamical model discordance or a warm bias in this region.

The simulated averages of  $\delta D(H_2O)$  in precipitation in Antarctica of the SD\_REF simulation are compared with the results from the ECHAM5-wiso model (in T159L31 resolution) in Fig. 4.7. This is conducted in order to evaluate the fractionation effects at very low temperatures and in the ice phase, which will also become important when analysing the upper troposphere and the lower stratosphere.

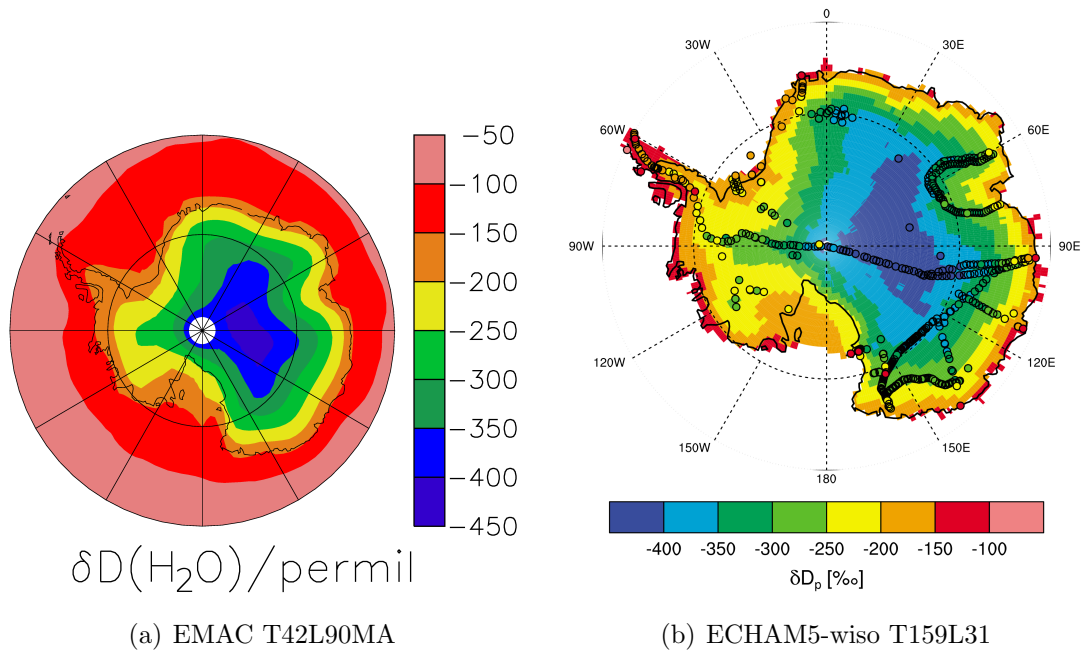


Figure 4.7: Comparison of the annual averages of  $\delta D(H_2O)$  in precipitation between EMAC T42L90MA and ECHAM5-wiso T159L31 in Antarctica. The image of panel (b) is taken from Werner et al. (2011).

Despite the differences in horizontal resolution,  $\delta D(H_2O)$  in precipitation agrees well in Antarctica between the two simulations. The lowest values can be found in the dry inner region of East Antarctica, with minimum values below  $-400\text{‰}$ . The coastal regions of Antarctica show values between  $-200$  and  $-100\text{‰}$ . The comparison of these results by Werner et al. (2011) with observations compiled by Masson-Delmotte et al. (2008) generally revealed a good agreement, as well. The  $\delta D(H_2O)$  values, however, are less depleted than the measurements. According to Werner et al. (2011), this is due to a warm bias over Antarctica, which has also been reported for other isotopologue-enabled GCMs, e.g., by Lee et al. (2007) and Risi et al. (2010). Since the dynamical core of EMAC bases on the ECHAM5 model, it is not surprising, that this bias is present in EMAC as well. Also postdepositional effects like wind erosion and the drifting of snow may contribute to local deviations between model and observations (Werner et al., 2011).

### 4.2.3 Discussion of the model results in the troposphere

The results of the isotope ratios in precipitation of the EMAC simulations FREE\_VAL and SD\_REF have been compared to observations from the GNIP measurement survey and the ECHAM5-wiso model in this section. The comparison with GNIP data generally shows a good agreement, considering the main characteristics, which can be observed in the isotopic composition in precipitation. These were already described by Dansgaard (1964) and in Sect. 2.2.5. In most of the regions also the values, the amplitude and the seasonal cycles compare well with the GNIP measurements. Some regions, though, show considerable differences between model and observations. These can partly be associated with the low (horizontal) resolution of the model, others, however, are not as easily explainable. The constant bias in the northern Canadian regions and Greenland, as well as the warm bias in Antarctica are likely to be general dynamical inaccuracies of the model. Since the isotopic composition of precipitation strongly depends on parameters like evaporation and condensation temperatures as well as the seasonal cycle and small scale features of precipitation, the isotope ratios are very sensitive to the climate conditions. An exact match between model and observations is hence not to be expected. Considering the inaccuracies of the model, but also the difficulties in compiling a representative data set out of partly sparse measurements, the deviations are in a reasonable range.

The simulations of the EMAC model and the ECHAM5-wiso (Werner et al., 2011) model agree very well. Since the hydrological cycles of the two models are basically equal, this was expected. The vertical resolution and the addition of the stratospheric chemistry in the SD\_REF have only little influence on the isotopic composition in precipitation, although according to Roeckner et al. (2006) a higher vertical resolution improves the general circulation patterns. Hence, the still given deviations mainly arise from the different SSTs, which are, apart from the specified dynamics in the SD\_REF simulation, the only substantial boundary condition in the simulations. The representation of the isotopologues in the hydrological cycle of the ECHAM5-wiso model bases on previous isotopologue-enabled GCMs like Joussaume et al. (1984) including ECHAM versions like the studies by Hoffmann et al. (1998) and Werner et al. (2001). Comprehensive GCM intercomparison studies for stable water isotopologues have been conducted in the SWING (Stable Water Isotope Intercomparison Group) project (Noone, 2006), where also the previous isotopologue-enabled ECHAM versions successfully participated. Hence the conclusion can be drawn, that the EMAC model with the H2OISO submodel represents the state of the art of GCMs with explicit representation of the water isotopologues HDO and  $\text{H}_2^{18}\text{O}$  in the troposphere. In addition to that, the modularity of the H2OISO submodel within the EMAC model and its applicability to other basemodels, makes it unique.

## 4.3 Evaluation of stratospheric isotope quantities

In order to obtain an assessment of EMAC for the representation of the isotopologues in the stratosphere, an evaluation of the results of the SD\_REF simulation in the stratosphere was carried out. Since measurements at these altitudes are mostly available for HDO only, and also there is no accounting for the much more complex chemical effects of  $\text{H}_2^{18}\text{O}$ , this evaluation is conducted only for HDO and  $\delta\text{D}(\text{H}_2\text{O})$ . Before evaluating the isotopic



composition of stratospheric water, however, at first its chemical precursor, the methane isotopologue  $\text{CH}_3\text{D}$  and  $\delta\text{D}(\text{CH}_4)$ , is evaluated. In this regard, the model results are tested against a chemical transport model in Sect. 4.3.1 and against measurements from high altitude radiosonde flights in Sect. 4.3.2. Successively the stratospheric water isotope ratios are compared with aircraft measurements in Sect. 4.3.3, and with recent satellite observations from several instruments (Envisat/MIPAS, SCISAT/ACE-FTS and Odin/SMR) in Sect. 4.3.4. In Sect. 4.3.5 qualitative good agreement between the model and the observational data is concluded for the newly included quantities. Regional quantitative deficits, however, have to be kept in mind for the analysis of the model simulations and require further development of the model.

### 4.3.1 Comparison of $\delta\text{D}(\text{CH}_4)$ with the CHEM2D model

First, the simulated  $\text{CH}_3\text{D}$  of the H2OISO submodel in EMAC is compared to results from the CHEM2D model by Ridal and Siskind (2002) and the CHEM1D model by Ridal et al. (2001). The CHEM2D model comprises an oxidation scheme, where  $\text{CH}_3\text{D}$  produces HDO through a number of chemical reactions. The oxidation scheme was adapted from Ridal et al. (2001) and extended for higher altitudes, as well as included into the Naval Research Laboratory two-dimensional chemical/dynamical model by Ridal and Siskind (2002). In Ridal (2002) and Ridal and Siskind (2002) the two chemical transport models have shown a good general agreement with measurements from the ATMOS (Atmospheric Trace Molecule Spectroscopy) instrument (Irion et al., 1996). ATMOS provides global data for  $\text{CH}_3\text{D}$  and HDO, however, with extremely large uncertainties. The equatorial values of  $\delta\text{D}(\text{CH}_4)$  (note that  $\delta\text{D}(\text{CH}_4)$  is also based on VSMOW) of the SD\_REF simulation of the EMAC model, the CHEM2D model and the CHEM1D model are presented in Fig. 4.8.

Since in all three models, the tropospheric values of  $\delta\text{D}(\text{CH}_4)$  are fixed to  $-68\text{‰}$ , they do not differ below the tropopause. Moreover, the overall dependence of  $\delta\text{D}(\text{CH}_4)$  from altitude agree in all the three model simulations. Between 20 and 50 km altitude, the methane isotope ratio increases from  $-68$  to around  $+120\text{‰}$  in the CHEM2D and CHEM1D models, and to around  $+130\text{‰}$  in EMAC. Especially the increase in the lower stratosphere is much stronger in EMAC. Between 50 and 60 km, both, the CHEM2D model and EMAC, show almost no change in  $\delta\text{D}(\text{CH}_4)$  with altitude, the CHEM1D model does not extend above 50 km. This is the transition region between the altitudes of the chemical and the photolytic methane dissociation. The photolysis, which becomes important above 60 km and increases continuously above, is much stronger in the CHEM2D model at first. This is somewhat surprising, because there is no fractionation included for the photolysis of  $\text{CH}_3\text{D}$  in the CHEM2D model. Even though the fractionation for photolysis in EMAC is very small, the photolysis of  $\text{CH}_3\text{D}$  is expected to be of similar strength as in CHEM2D. Hence, this is likely to be caused by the differences in the calculation of the photolysis rates in EMAC and CHEM2D. Since the mid of the uppermost layer of the EMAC model in the applied resolution is at 80 km, a comparison further above is not possible.

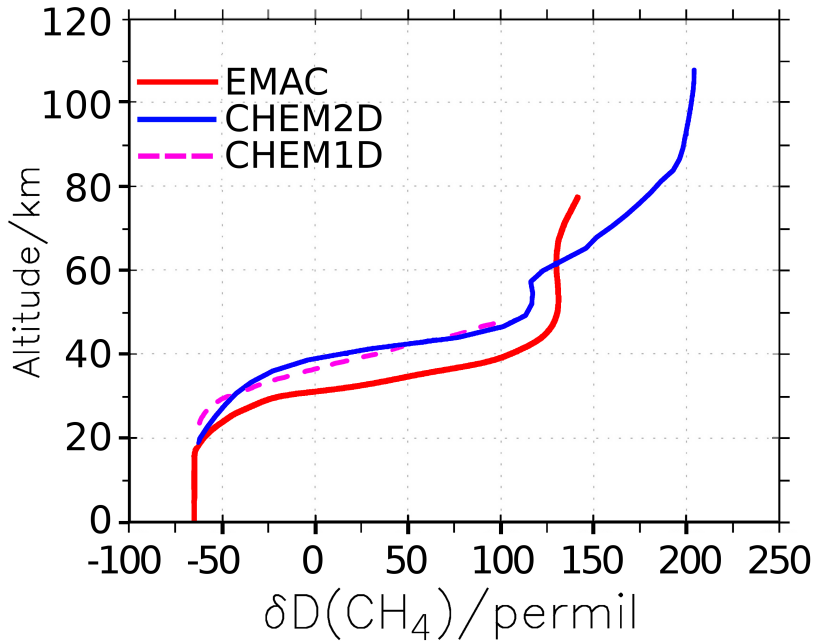


Figure 4.8: Comparison of equatorial averages of  $\delta D(\text{CH}_4)$  with altitude between the SD\_REF simulation (red), the CHEM2D model (blue) by Ridal and Siskind (2002) and the CHEM1D model (dashed purple) by Ridal et al. (2001).

#### 4.3.2 Comparison of $\delta D(\text{CH}_4)$ with balloon-borne observations

Measurements of  $\text{CH}_3\text{D}$  in the stratosphere are sparse. Röckmann et al. (2011), however, collected 13 samples from stratospheric balloon borne air measurements, which were provided by the Max-Planck Institute (MPI) for Solar System Research and by the Institute for Atmospheric and Environmental Sciences of the University of Frankfurt. The mixing ratios of  $\text{CH}_4$  and  $\text{CH}_3\text{D}$  were measured, using a high-precision continuous flow isotope ratio mass spectrometry system (Brass and Röckmann, 2010). Twelve of these balloon flights can be used for direct intercomparison with the data from the SD\_REF simulation. One flight (Flight ID: HYD-87-03) was conducted in 1987. Since the model results are considered to be in steady-state only from 1990 on, this sample is not taken into account for the evaluation.

In Fig. 4.9 twelve panels are presented, with the balloon borne data (red lines) and the data from the SD\_REF simulation (blue line) of  $\delta D(\text{CH}_4)$  with altitude, between 5 and 35 km. The flight IDs, included in the panels provide information about the location, the month and the year of the balloon flight (see caption). To provide an estimate about the average and the annual variability of  $\delta D(\text{CH}_4)$  in the model simulation, additionally the averages, maxima and minima of the 21 simulation years of the respective months at the location of the launch are included in the panels.

In general, good agreement can be observed between the measured and the simulated data. Both, simulation and measurements, show an increase of the methane isotope ratios from tropospheric values to values between  $-100$  and  $-200\text{‰}$  at 25 to 35 km in the Arctic

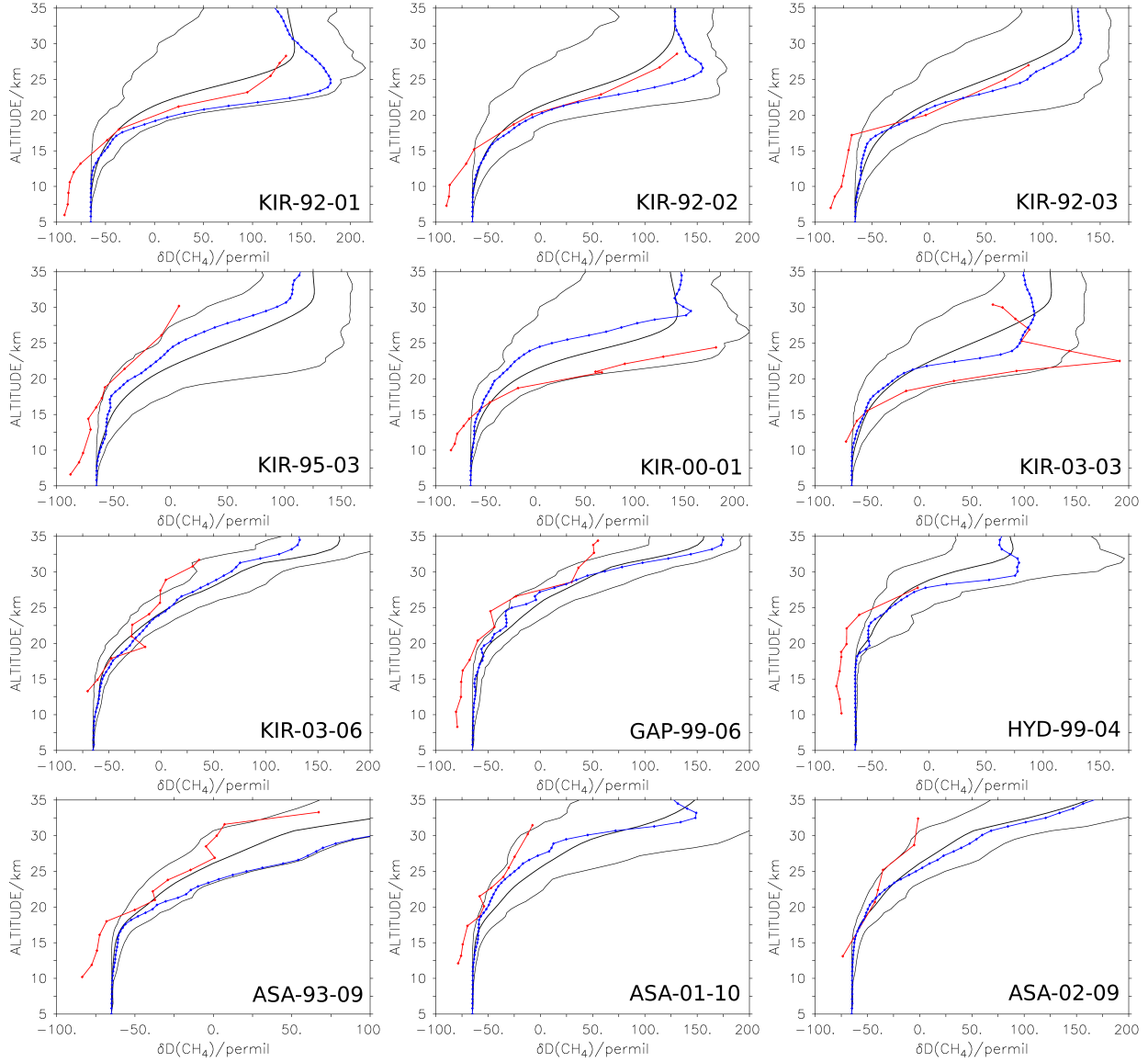


Figure 4.9: Comparison of  $\delta D(CH_4)$  vertical profiles between the SD-REF simulation and balloon borne data by Röckmann et al. (2011). The red line shows the observations and the blue line shows the EMAC data of the same day at the location of the balloon launch. The black lines represent simulated averages, minima and maxima of the 21 monthly averages of the respective month at the location of the balloon launch. The flight IDs, included in the panels denote the location, the year and the month of the balloon flight. KIR: Kiruna, Sweden ( $67.9^\circ N$ ,  $21.10^\circ E$ ); GAP: Gap, France ( $44.44^\circ N$ ,  $6.14^\circ E$ ); HYD: Hyderabad, India ( $17.5^\circ N$ ,  $78.60^\circ E$ ); ASA: Aire sur l'Adour, France ( $43.70^\circ N$ ,  $0.30^\circ W$ ).

region and to values between 0 and  $-100\text{‰}$  in the mid-latitude and tropical regions. The balloon borne samples are mostly lying within the extremes of the simulation and close to the simulated values from the same day and location. The measured values in the troposphere and lower stratosphere are, however, systematically lower than the simulated values. In contrast to the  $-68\text{‰}$  for stratospheric entry values of  $\delta\text{D}(\text{CH}_4)$ , suggested by Ridal and Siskind (2002), Röckmann et al. (2011) assess the typical tropospheric  $\delta\text{D}(\text{CH}_4)$  value to be  $-81\text{‰}$ . This explains the constant offset at lower altitudes between the two data sets and, it adjusted, could also reduce the differences at higher altitudes. Still, the simulated steep increase of  $\delta\text{D}(\text{CH}_4)$  above 25 to 30 km can only be seen in the measurements in the Arctic region (KIR). The mid-latitude (GAP and ASA) samples show considerable deviations here. The differences in the profiles of the KIR-00-01 and the KIR-03-03 samples between simulation and balloon flights are exceptional. Apart from the lower stratospheric regions (and the values above 25 km in sample KIR-03-03), the measured  $\delta\text{D}(\text{CH}_4)$  values are constantly higher than the simulated values. These samples are associated with special meteorological and thus chemical situations. The KIR-03-03 sample comprises a mesospheric enclosure and during the sampling of the KIR-00-01 data, a strong Arctic vortex was present (Röckmann et al., 2011). These phenomena can actually also be observed from the simulation. Due to the “nudging” these meteorological features and the associated chemical situations are broadly represented. However, sharp horizontal gradients can be observed in the isotopic composition of methane in the simulation around the site of the balloon launch. Small variations of the situation, but especially also the location of the balloons, which drift off the launching site while ascending, can easily cause deviations in that order.

Another method for evaluating the methane isotopologue chemistry is assessing the relation of  $\delta\text{D}(\text{CH}_4)$  to the  $\text{CH}_4$  mixing ratio. The  $\delta\text{D}(\text{CH}_4)$  values of the same data as in Fig. 4.9, from 5 to 35 km altitude, are plotted versus the  $\text{CH}_4$  mixing ratios in Fig. 4.10. The black lines represent the data from the model simulation and the red lines the balloon samples. The figure is divided into the launches in the polar region (KIR) in the left panel and the launches in middle (ASA, GAP) and tropical (HYD) latitudes in the right panel. Here also the HYD-87-03 sample, which was not considered in the previous figure, is included for completion (a simulated counterpart is not included).

Again a constant offset between the simulation and the measurements can be seen. Apart from a single outlier, the measurement from the HYD-99-04 sample (right panel), the simulated  $\delta\text{D}(\text{CH}_4)$  values are generally higher for the same methane mixing ratios. Changing the fixed tropospheric value from  $-68$  to  $-81\text{‰}$  is assumed to reduce this offset. The slope of increasing isotope ratios with decreasing methane mixing ratios is in very good agreement. Since these compact tracer-tracer correlations are generally found for trace gases whose life time is longer than the transport times (Plumb and Ko, 2004), it implies that the chemical removal of the  $\text{CH}_3\text{D}$  tracer in relation to the removal of the  $\text{CH}_4$  tracer, is well represented at these altitudes, despite the simplified chemistry parameterisation.

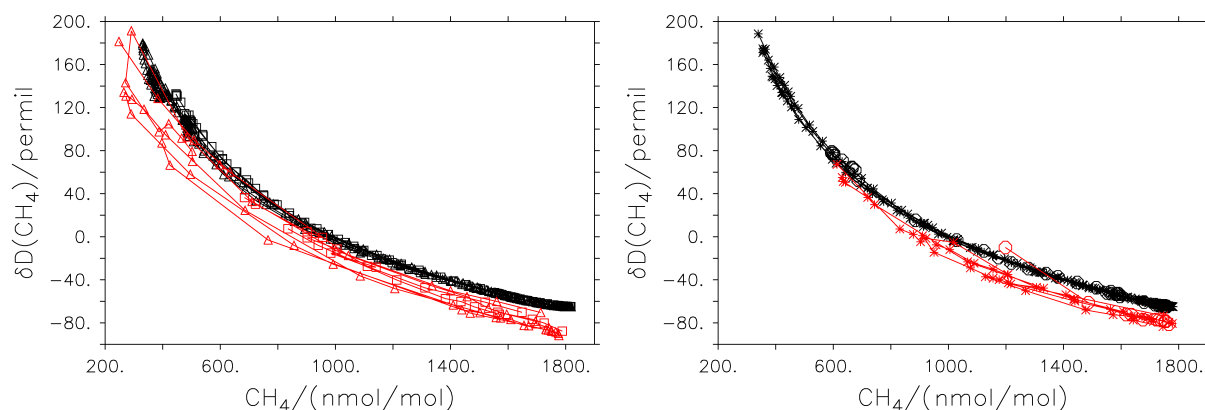


Figure 4.10: Comparison of the relations of  $\text{CH}_4$  to  $\delta\text{D}(\text{CH}_4)$  between the EMAC (black) SD\_REF simulation and balloon borne data (red; data as in Fig. 4.9). The left panel shows the arctic samples (KIR,  $\triangle$ : vortex,  $\square$ : non-vortex) and the right panel shows the mid-latitude ( $*$ ) and tropical samples ( $\circ$ ). The altitude range is 5 to 35 km.

### 4.3.3 Comparison of HDO with in situ observations

In situ observations of HDO are available from several measurement campaigns. Johnson et al. (2001b) analysed samples of HDO measured with the Smithsonian Astrophysical Observatory far-infrared spectrometer (FIRS-2) from seven balloon flights that took place between 1989 and 1997. By comparing these with the results of a photochemical model, they found that water vapour enters the stratosphere with a  $\delta\text{D}$  value of  $-679 \pm 20\text{‰}$ .

Balloon borne observations were also conducted with a solar occultation FTIR (Fourier transform infrared) spectrometer and evaluated by Notholt et al. (2010) up to 30 km. They found, that the seasonal variations in  $\text{H}_2\text{O}$  are mirrored in the variation of  $\delta\text{D}(\text{H}_2\text{O})$ . Recent aircraft observations were carried out by Coffey et al. (2006); Hanisco et al. (2007) and Sayres et al. (2010). They used different instruments, which base on principles like the infrared absorption of sunlight by the atmosphere or absorption spectroscopy. The measurements of these campaigns agree among themselves and with older in situ observations and reveal stratospheric  $\delta\text{D}(\text{H}_2\text{O})$  values between  $-600$  and  $-400\text{‰}$  (Hanisco et al., 2007). Sayres et al. (2010) find that water vapour at the lower part of the TTL is isotopically lighter in boreal winter with a mean  $\delta\text{D}(\text{H}_2\text{O})$  of  $-650\text{‰}$ . The upper part of the TTL is characterised by an increase in  $\delta\text{D}(\text{H}_2\text{O})$  with a mean of  $-500\text{‰}$ . The EMAC SD\_REF simulation qualitatively matches with these findings. In the simulation the isotopically most depleted stratospheric water vapour, however, shows  $\delta\text{D}(\text{H}_2\text{O})$  values down to  $-750\text{‰}$  and  $\delta\text{D}(\text{H}_2\text{O})$  values above  $-500\text{‰}$  can only be found above 25 km in the tropics.

In 2010 the CARIBIC (Civil Aircraft for the Regular Investigation of the atmosphere Based on an Instrument Container) project started to measure water isotopologues using the tunable diode-laser absorption spectrometer ISOWAT. Since CARIBIC regularly operates aboard a passenger aircraft during equator-crossing long-distance flights, climatologies of  $\delta\text{D}(\text{H}_2\text{O})$  are about to be compiled. These data are still being processed and therefore not available, yet. Available in situ measurements, however, are sparse in spatial and temporal coverage and hence are only suitable for the evaluation of a global climate model to

a small degree. The evaluation of HDO in the EMAC model will therefore focus on the comparison with satellite measurements, because of the better coverage of that data. This is presented in the next section.

#### 4.3.4 Comparison of HDO and $\delta D(H_2O)$ with satellite observations

During the first decade of the 21st century, three satellite missions collected data applicable for the retrieval of the water isotopologue HDO in the stratosphere. The MIPAS (Michelson Interferometer for Passive Atmospheric Sounding) instrument on Envisat (Environmental Satellite) allowed the retrieval of HDO by measuring the thermal emission in the mid-infrared. This high-resolution Fourier transform spectrometer measured at the atmospheric limb and provided HDO data in full spectral resolution from July 2002 to March 2004, roughly in the altitude range between 10 and 50 km. It orbits the Earth sun-synchronously 14 times a day and its vertical resolution for HDO is around 5 km (Steinwagner et al., 2007; Lossow et al., 2011). The Odin satellite also orbits the Earth sun-synchronously and carries the SMR (Sub-Millimetre Radiometer) instrument, among other purposes to passively measure HDO on the global scale, on roughly one day per week. It operates in the microwave range. Data has been retrieved from the start of the mission in 2001 until today, at altitudes between roughly 20 and 70 km with a vertical resolution of around 3 km (Urban et al., 2007). The ACE-FTS (Atmospheric Chemistry Experiment Fourier Transform Spectrometer) instrument circularly orbits the Earth on the SCISAT satellite and obtains Fourier transform absorption spectra from solar occultation measurements. It has a vertical resolution between 2 and 6 km and a comparably limited spatial sampling. In the tropics HDO can be retrieved only during the four months of February, April, August and October (Nassar et al., 2007; Randel et al., 2012).

Lossow et al. (2011) collected data of the three instruments for intercomparison and concluded a good consistency at altitudes above 20 km. Below this altitude, issues like different resolutions, cloud filtering and measurement techniques cause large deviations. In the stratosphere, the MIPAS and the ACE-FTS data agree favourably, the SMR data shows considerably dryer conditions, especially below 30 km.

These data were now also used to evaluate the HDO simulated by EMAC in the SD\_REF simulation in Fig. 4.11. Here, the tropical ( $15^\circ S$  to  $15^\circ N$ ) values of HDO of the three satellite instruments and the EMAC model are presented. Additionally to the data of MIPAS, SMR and version 2.2 of ACE-FTS shown by Lossow et al. (2011), here also version 3.0 of ACE-FTS is included, which reaches higher up in the stratosphere, compared to version 2.2. Since ACE-FTS only provides data for four months per year in this region, the panels show averages for February, April, August and October. Since the years of the satellite retrievals do not overlap, a direct intercomparison is not possible. Therefore, the averages, the minima and the maxima of the respective months have been taken from the 21 years of the EMAC simulation.

The EMAC data is generally dryer in HDO compared to the MIPAS and the ACE-FTS profiles in each of the presented months at all altitudes. Only between 30 and 35 km, the HDO profiles of EMAC increase stronger than in the satellite data and reach the level of MIPAS and ACE-FTS HDO mixing ratios. In the altitude range between 16 and 30 km, the

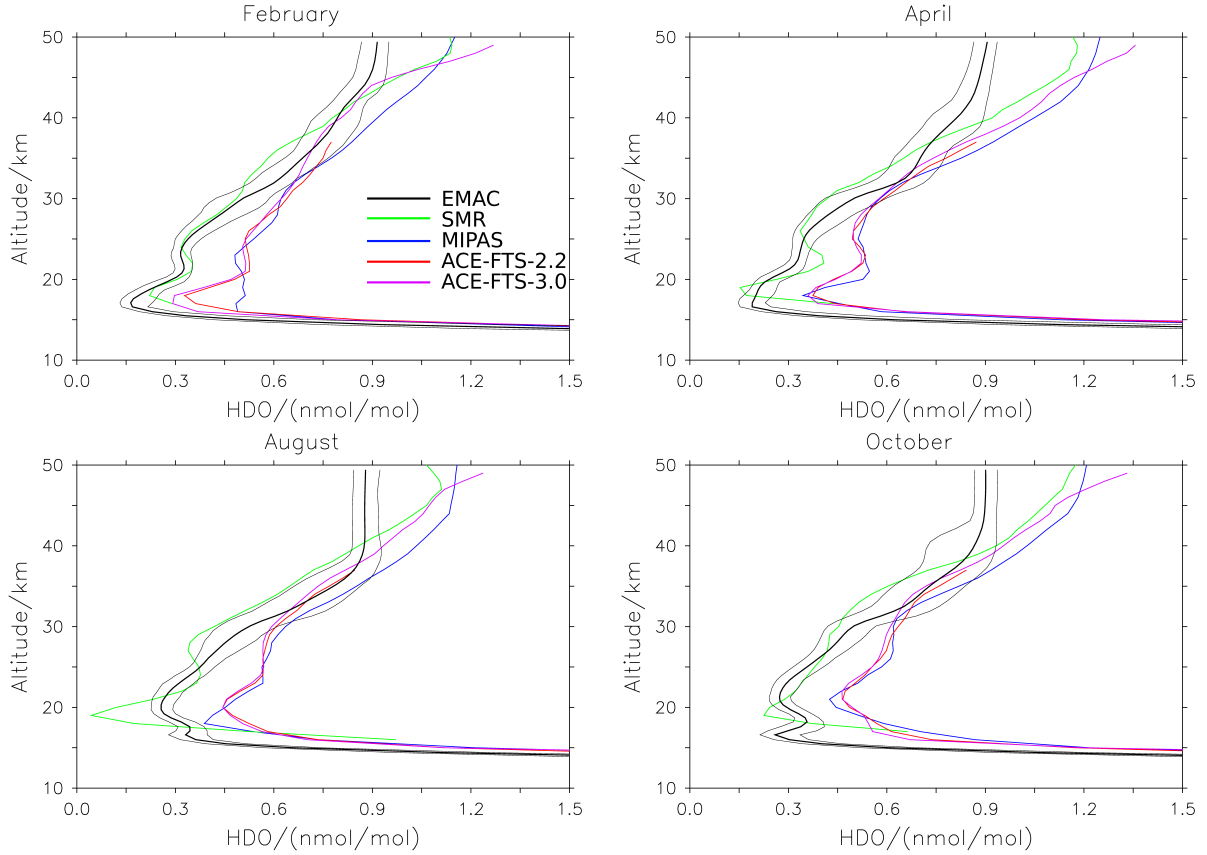


Figure 4.11: Comparison of HDO altitude profiles between EMAC and various satellite observations. Black: Averages, minima and maxima of the 21 monthly averages of the EMAC SD\_REF simulation for the respective months; green: Odin/SMR; blue: ENVISAT/MIPAS; red: SCISAT/ACE-FTS-2.2; purple: SCISAT/ACE-FTS-3.0.

EMAC simulation quantitatively corresponds well with the Odin retrieval. In this region also local maxima and minima, which can be seen in all four satellite profiles are reproduced qualitatively in EMAC. These reveal the seasonal cycle of HDO. However, especially for April and August, the local minimum between 25 and 30 km in the EMAC data is not as pronounced as in the satellite retrievals. Above 40 km, the HDO mixing ratios of all satellite profiles increase strongly with altitude to values around 1.1 nmol/mol at 50 km, while the EMAC simulation shows HDO mixing ratios of only 0.9 nmol/mol at this altitude. This may be due to the assumptions made in the chemistry parameterisation (see Sect. 3.3.6), which do not include the influence of the isotopic composition of molecular hydrogen on HDO. This effect seems to become important at these altitudes.

The MIPAS data is also used for evaluating the tape recorder signal of the EMAC model in  $\text{H}_2\text{O}$ , HDO and  $\delta\text{D}(\text{H}_2\text{O})$ . The satellite and the model data are compared in Fig. 4.12. The left panels show the EMAC results and the right panels show the MIPAS retrieval.

Overall, there is only a rather weak agreement between EMAC and MIPAS in all three quantities. A persistent (all altitudes, all seasons) dry bias in  $\text{H}_2\text{O}$  and HDO is visible in the

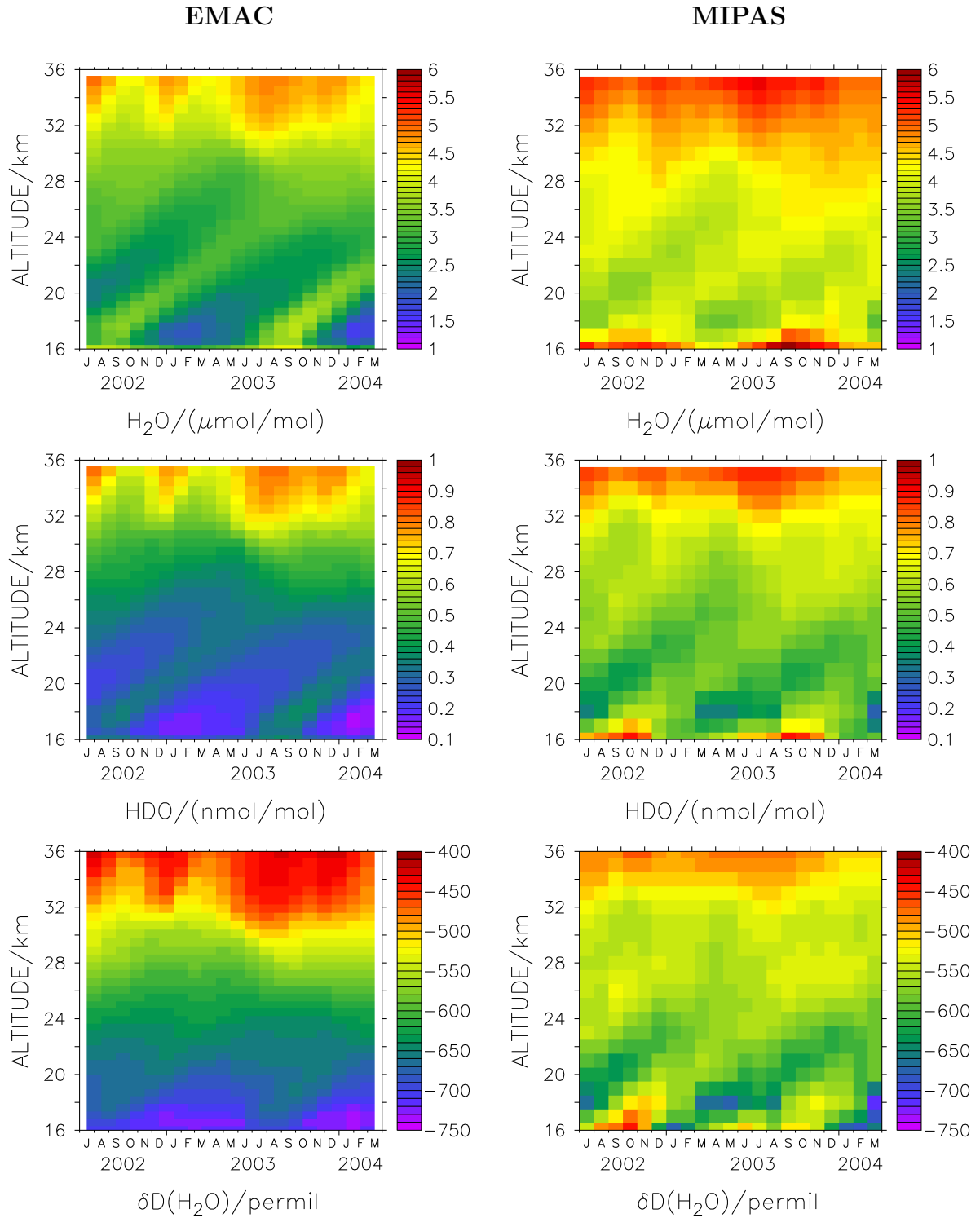


Figure 4.12: Altitude-time diagrams of tropical (15°S-15°N) H<sub>2</sub>O, HDO and δD(H<sub>2</sub>O). Left: EMAC SD\_REF simulation, right: MIPAS observations.



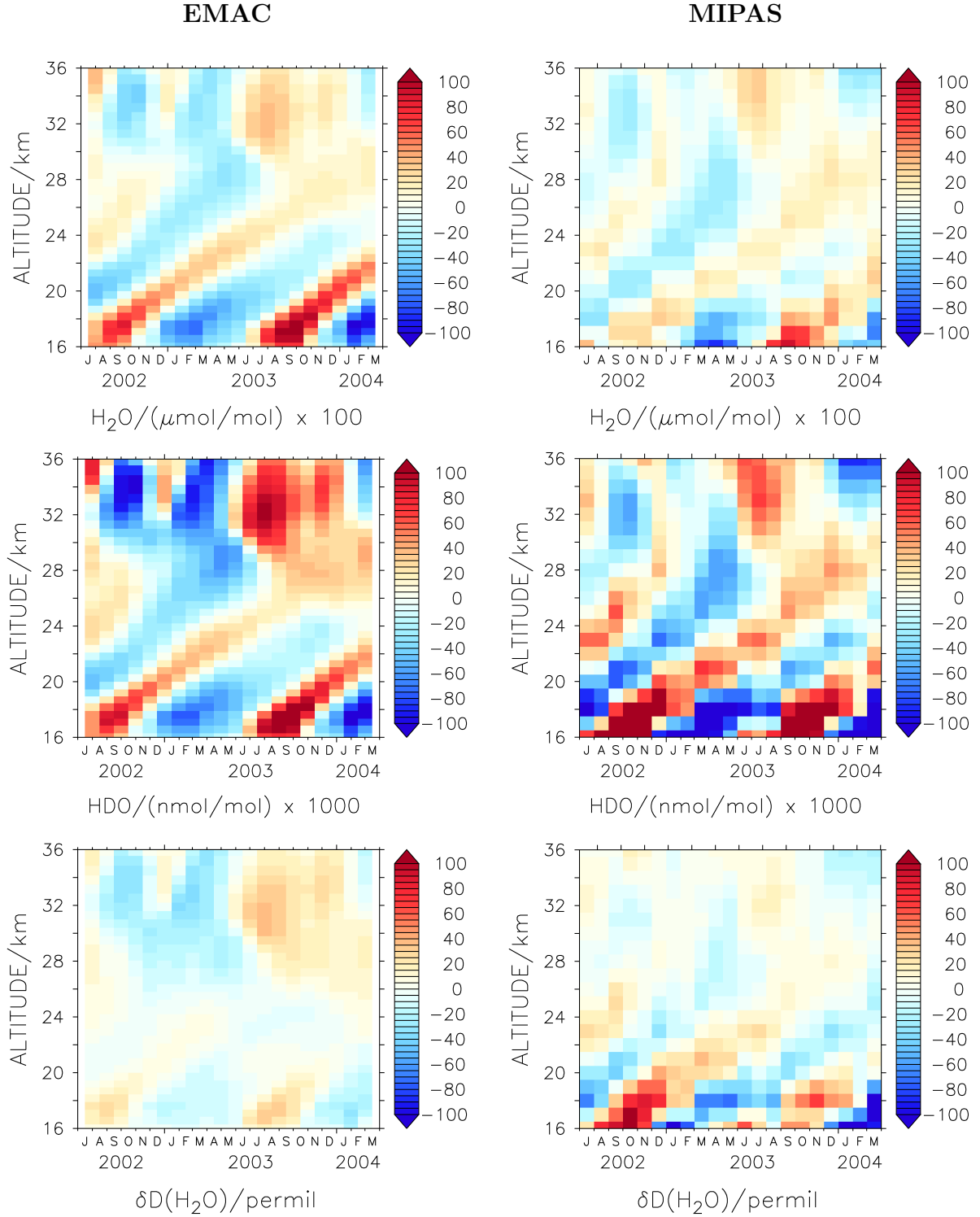


Figure 4.13: Altitude-time diagrams of the vertical profile of the anomaly of tropical ( $15^\circ\text{S}$ - $15^\circ\text{N}$ )  $\text{H}_2\text{O}$ , HDO and  $\delta\text{D}(\text{H}_2\text{O})$  to the average over the presented period. Left: EMAC SD\_REF simulation, right: MIPAS observations.

EMAC simulation.  $\delta D(H_2O)$  is slightly too high in the upper stratosphere and generally too low in the lower stratosphere. In the lower stratosphere, some of these differences can be explained with the coarse vertical resolution of the MIPAS retrieval, which smoothes the hygropause (see Steinwagner et al., 2007). The overestimation of  $\delta D(H_2O)$  in EMAC at around 35 km, corresponds to the altitudes ( $\sim 30$ -35 km) where HDO increases too strong in the simulation, as seen in Fig. 4.11. In the lower stratosphere, the strongest deviations in  $\delta D(H_2O)$  can be observed during NH summer, when MIPAS observations show  $\delta D(H_2O)$  values around  $-500\text{‰}$  and the  $\delta D(H_2O)$  values in EMAC do not exceed  $-600\text{‰}$ . A tape recorder signal can be seen in all three quantities for both, model and observations, although with different amplitudes and a phase shift of two to three months. While the maxima of the tape recorder in the lower stratosphere in EMAC are found during summer, the satellite data show them at the beginning of autumn. This can partly be an artefact of the MIPAS retrieval and its vertical sampling, but has to be kept in mind and compared with other data sets. The tape recorder signals in HDO and  $H_2O$  fade out at around 30 km in both, model and observations. The  $\delta D(H_2O)$  tape recorder signal in MIPAS reaches these altitudes as well, while the EMAC  $\delta D(H_2O)$  tape recorder, in contrast, fades out below 25 km already.

In order to provide a better insight into the amplitude of the tape recorder signal, Fig. 4.13 shows the deviations of HDO,  $H_2O$  and  $\delta D(H_2O)$  from their average of the sampled period, similar as they have been displayed by Steinwagner et al. (2010). Again the left panels show the EMAC SD\_REF simulation and the right panels show the MIPAS observations.

The amplitude of the tape recorder in EMAC is larger for  $H_2O$  and smaller for HDO and  $\delta D(H_2O)$ , respectively, compared to the MIPAS data. The lower fade-out of the  $\delta D(H_2O)$  tape recorder can be observed here as well. This illustration also shows, that the tape recorder above 25 km becomes overshadowed by a signal, which apparently propagates downwards over time from the upper stratosphere. Due to the length of its phase and its altitudes, this may well be connected with the quasi biannual circulation (QBO). According to S. Lossow (2014, personal communication) the tape recorder effect in  $\delta D(H_2O)$  can be amplified artificially by the offsets in vertical resolution between  $H_2O$  and HDO. A correction of this error is expected to reveal a  $\delta D(H_2O)$  tape recorder signal with smaller amplitude in the MIPAS retrieval. The Odin retrieval shows a less pronounced tape recorder signal (Lossow et al., 2011) as well, which matches to the estimation of a corrected and thus less pronounced MIPAS  $\delta D(H_2O)$  tape recorder and also is closer to the amplitude of the  $\delta D(H_2O)$  tape recorder in EMAC.

By analysing ACE-FTS data, Randel et al. (2012) found a tape recorder signal in  $H_2O$  and in HDO, but could not find a corresponding pattern in  $\delta D(H_2O)$  (see Fig. 4.14). The lower stratosphere shows distinct seasonally varying maxima and minima of  $\delta D(H_2O)$ . These, however, hardly propagate upwards in time. For comparison with the ACE-FTS data, the tropical  $H_2O$ , HDO and  $\delta D(H_2O)$  in the stratosphere of the SD\_REF simulation are displayed in Fig. 4.15 for the same period and altitudes as in Randel et al. (2012).

The left panels show the monthly averages of the respective values. Quantitatively these agree fairly well with the ACE-FTS observations by Randel et al. (2012). The increase of

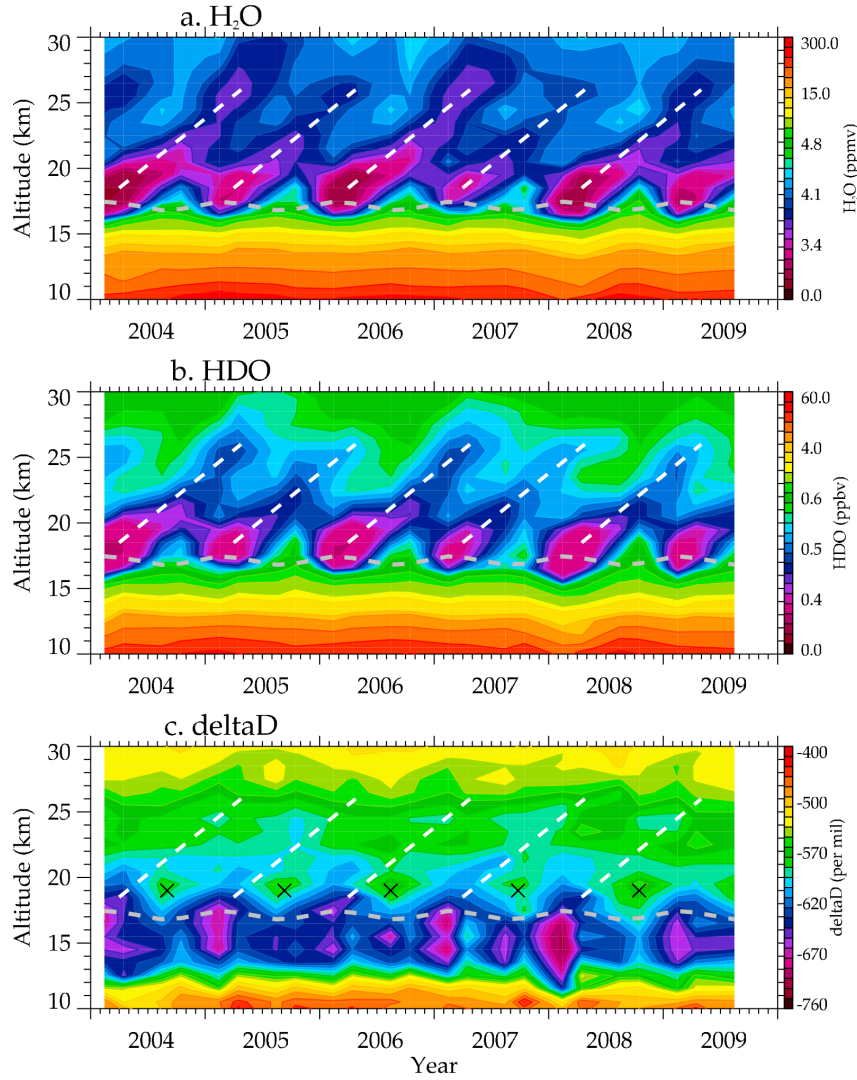


Figure 4.14: Altitude-time diagrams of H<sub>2</sub>O, HDO mixing ratios and  $\delta D(H_2O)$  in the tropics (15°N-15°S) derived from ACE-FTS observations during 2004-2009 (Randel et al., 2012).

the quantities with altitude in the stratosphere is represented well. At 30 km,  $\delta D(H_2O)$  exhibits values around  $-500\text{‰}$ , which matches with ACE-FTS data. Similarly to the comparison with the MIPAS retrieval, however, the lower stratosphere in EMAC is dryer, especially in HDO. Still, a clear tape recorder signal can be observed in all three panels, with minimum values in the lower stratosphere during boreal winter and maxima during boreal summer. These seasonal wave patterns propagate upwards in time and fade out between 25 and 30 km for H<sub>2</sub>O and HDO and somewhat lower for  $\delta D(H_2O)$ . As already stated before, the chemical effect overshadows the  $\delta D(H_2O)$  tape recorder above 25 km. This effect will be analysed in more detail in Sect. 5.2.

For the right panels, the EMAC data has been filtered, using only the four months (February, April, August and October), which are also available in the ACE-FTS retrieval, to estimate the influence of the sparse temporal sampling on the tape recorder signals.

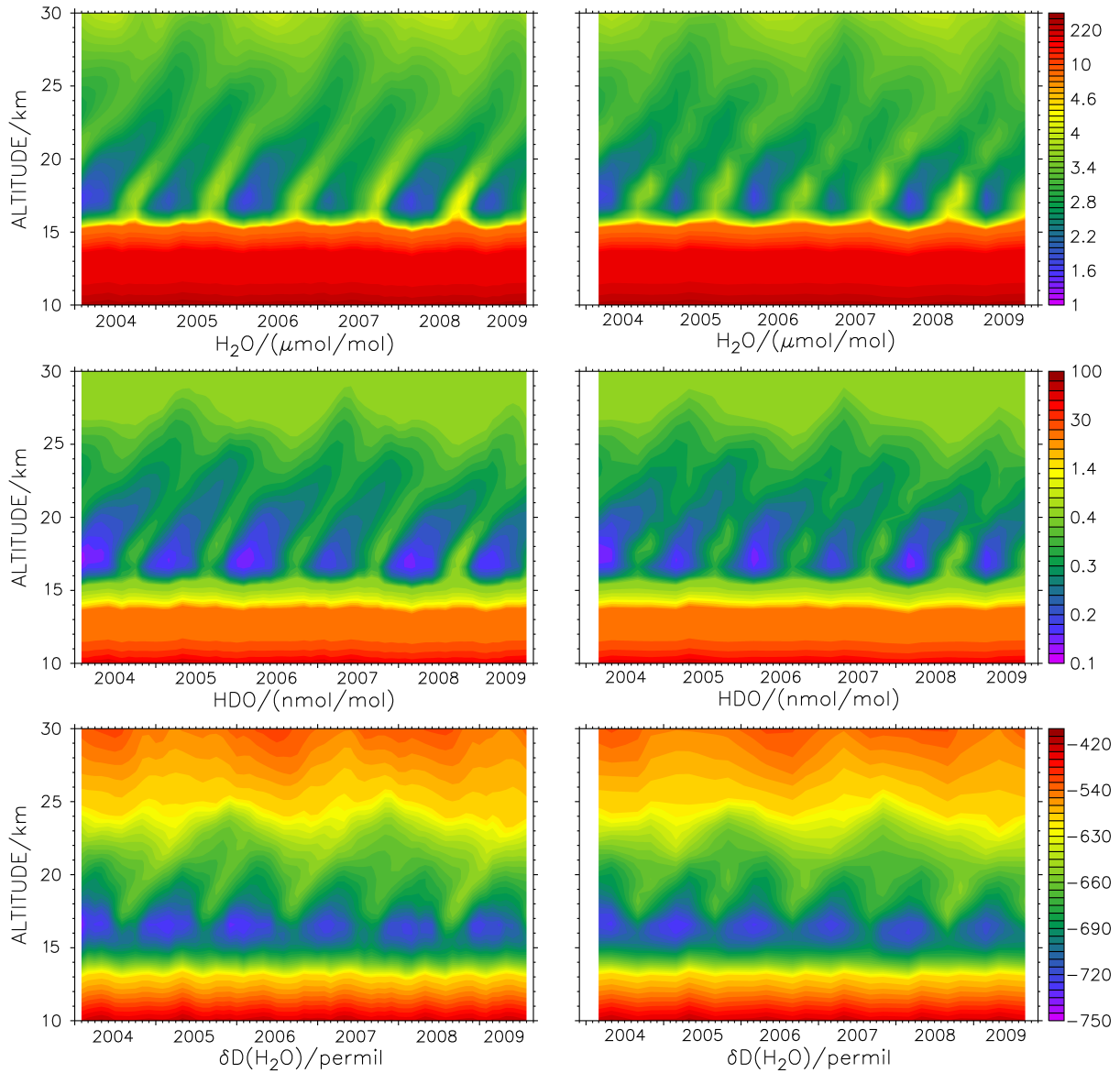


Figure 4.15: Altitude-time diagrams of tropical ( $15^{\circ}\text{S}$ - $15^{\circ}\text{N}$ )  $\text{H}_2\text{O}$ ,  $\text{HDO}$  and  $\delta\text{D}(\text{H}_2\text{O})$  of the EMAC SD\_REF simulation. Left: monthly averages; right: averages of only February, April, August and October, as in Randel et al. (2012). The plotting algorithm linearly interpolates between the available months.

This filtering somewhat blurs the tape recorder in all three panels, compared to the full data set. Especially the tape recorder in  $\delta\text{D}(\text{H}_2\text{O})$ , however, appears to lose some of its upward motion at around 20 km. Moreover, it fades out at even lower altitudes. In fact, as in Fig. 4.14, the signal is now hardly visible. Therefore, it can be assumed, that the sparse temporal sampling of ACE-FTS data is an issue in the evaluation of the  $\delta\text{D}(\text{H}_2\text{O})$  tape recorder and may well contribute to the indistinctness of the signal in the study by Randel et al. (2012).

### 4.3.5 Discussion of the model results in the stratosphere

The stratospheric distribution of the new EMAC tracers  $\text{CH}_3\text{D}$  and  $\text{HDO}$  have been evaluated in this section.  $\text{CH}_3\text{D}$  was compared to chemical transport models and to data from radiosonde flights. The EMAC model is able to reproduce the general stratospheric patterns of  $\text{CH}_3\text{D}$ , with some consistent deviations. Lower stratospheric  $\delta\text{D}(\text{CH}_4)$  in the tropics increases stronger with altitude in the EMAC model compared to the  $\text{CHEM1D}$  and the  $\text{CHEM2D}$  models (Ridal et al., 2001; Ridal and Siskind, 2002). The oxidation reactions of  $\text{CH}_4$  and  $\text{CH}_3\text{D}$  basically do not differ between the three models, the fractionation factors, albeit, do. The difference in the fractionation factors of Kaye (1987), which were used by Ridal et al. (2001) and Ridal and Siskind (2002) and those from Saueressig et al. (1996) and Saueressig et al. (2001) applied in the present study may cause these deviations. However, also dynamical differences, like a mismatch in the tropopause height can cause the discrepancy. The different behaviour of  $\delta\text{D}(\text{CH}_4)$  above 60 km, where photochemistry is determining, has to be associated with the different photolysis schemes, because fractionation is not decisive here. Due to a lack of observations, these inconsistencies can not be evaluated with measurements at these altitudes. However, the effect of this region on the processes in the UTLS are considered to be low.

A too strong increase in  $\delta\text{D}(\text{CH}_4)$  in the lower stratosphere can also be observed in the comparison of EMAC with balloon-borne measurements by Röckmann et al. (2011). Especially the mid-latitude profiles exhibit this offset. Apart from the isotope fractionation, also dynamical issues and the likewise inaccurate accounting for methane itself, can lead to discrepancies in these comparisons. The general behaviour of the tracer in the stratosphere is reproduced well and the correction of the fixed tropospheric value from  $-68\text{‰}$  to a lower value is expected to generate even more coinciding results. Furthermore, the good agreement between model results and observations in the slope of the relation between  $\text{CH}_4$  and  $\delta\text{D}(\text{CH}_4)$ , reveals that the sink reactions of the two species match. After all, better temporally and spatially covered observations are needed to work out the specific flaws of the model simulation.

In order to provide a more general picture of  $\delta\text{D}(\text{CH}_4)$  in the model, its seasonal averages of the  $\text{SD\_REF}$  simulation are shown in Fig. 4.16. The influence of the two driving mechanisms of this quantity, the oxidation of  $\text{CH}_4$  and  $\text{CH}_3\text{D}$  and the stratospheric dynamics, can be examined herewith.

Due to the longer lifetime of  $\text{CH}_3\text{D}$  compared to  $\text{CH}_4$ , the low tropospheric  $\delta\text{D}(\text{CH}_4)$  transitions into high values in the stratosphere. As expected, the low values reach the highest altitudes in the tropics. The highest  $\delta\text{D}(\text{CH}_4)$  can be found in the polar regions during the respective summers and autumns at altitudes between roughly 30 and 40 km. This is associated with strong photochemistry and hence high concentrations of the reactant species at that time. Note that high  $\delta\text{D}(\text{CH}_4)$  values in the polar region, in contrary, can be found at lower altitudes in wintertime. This is associated with strong downward motion within the polar vortices and explains the differences in the polar profiles outside and within the vortex of Fig. 4.9.

The evaluation of  $\text{HDO}$  focused mainly on the comparison of the EMAC simulation with satellite observations. Profiles of  $\text{HDO}$  of four different satellite retrievals (MIPAS, SMR, ACE-FTS-2.2 and ACE-FTS-3.0) were compared with the results from the EMAC

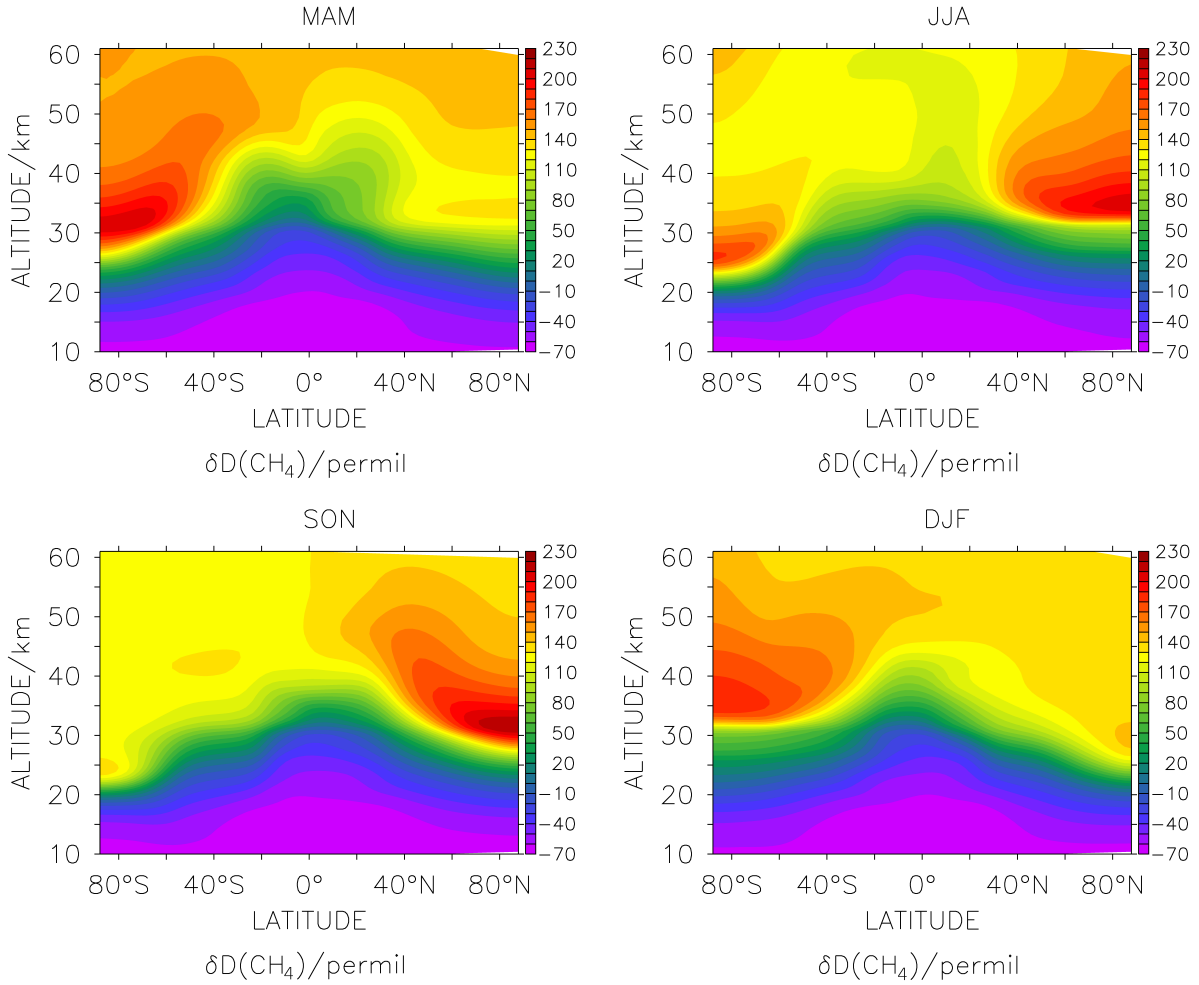


Figure 4.16: Zonally averaged seasonal  $\delta D(\text{CH}_4)$  averaged over the 21 years of the SD\_REF simulation.

model for four specific months (February, April, August, October). While the profiles of the MIPAS (Steinwagner et al., 2007, 2010) and the ACE-FTS (Nassar et al., 2007) retrievals exhibit higher HDO mixing ratios in the lower stratosphere than the EMAC model, the SMR profiles (Urban et al., 2007) and EMAC correspond well at these altitudes. The sampling of the MIPAS data has a rather coarse vertical resolution ( $\sim 5$  km), which can blur the hygropause (see e.g., Steinwagner et al., 2007). This can also be observed in the  $\text{H}_2\text{O}$  mixing ratio profiles. The somewhat better resolution of the ACE-FTS retrieval, however, does not change the results in this respect, except for the hygropause in February. The EMAC results are closest to the SMR data, which measures in the microwave spectrum, compared to the other two satellite instruments measuring in the infrared. Also different cloud filtering methods may generate discrepancies between the individual satellite observations (Lossow et al., 2011). Local maxima and minima are represented similarly in all the profiles, including the EMAC model, with only marginal differences. This confirms the representation of the seasonal cycle of the simulated HDO. Above 40 km the HDO mixing

ratios of the model simulation are much lower than all the satellite profiles. The incomplete representation of the chemical production of HDO in the stratosphere, neglecting the intermediate reactions with HD and the associated fractionation effects, is thought to be the reason for this offset.

The comparison of the tape recorder signals of H<sub>2</sub>O, HDO and  $\delta D(H_2O)$  between EMAC and MIPAS reveals similar conclusions. The dry bias in the lower stratosphere in the simulation can be seen in H<sub>2</sub>O and HDO, but is more pronounced in HDO. Between 30 and 35 km the increase of HDO is too strong in EMAC and hence  $\delta D(H_2O)$  exceeds the values of the MIPAS data. The effect of the chemistry is slightly too strong at these altitudes, which may be due to inaccuracies in the chemical fractionation coefficients. The underestimation of  $\delta D(H_2O)$  during NH summer in the lower stratosphere of EMAC may be associated with the model's representation of troposphere-stratosphere exchange processes, possibly ice-overshooting convection plays a role here. This will be investigated in more detail in the next chapter. The seasonal cycle exhibits comparability, although with a phase shift, differences in the amplitudes and a sooner fade-out of the  $\delta D(H_2O)$  tape recorder. In the lower stratosphere, the values differ the most during boreal summer, when ice overshooting convection is strongest. This is likely to be caused by deficiencies in the model's convection scheme.

Most of the deviations can be attributed to deficiencies in either the model or the satellite retrieval, which concludes that the overall representation of the processes is reasonable. The comparison of the tape recorder signal with the ACE-FTS observations underlines these conclusions. The tape recorder signals of EMAC and ACE-FTS agree well, and also the comparably weak  $\delta D(H_2O)$  tape recorder in EMAC matches, to a certain degree, with ACE-FTS observations. The illustration of the tape recorder compiled with data from only the four months of the ACE-FTS measurements, additionally, partly explains the discrepancies in the  $\delta D(H_2O)$  tape recorder signal between MIPAS (Steinwagner et al., 2010) and ACE-FTS (Randel et al., 2012) observations.

Due to the difficulties in the retrievals and the differences among the individual observations (see Lossow et al., 2011), an exact assessment of the EMAC model in the stratosphere is delicate. Consistent offsets between model and observations are found in the tropopause region and in the upper stratosphere. Still, in general the model can be considered to represent HDO and H<sub>2</sub>O well and thus the analysis of stratospheric  $\delta D(H_2O)$  simulated by the H2OISO submodel with EMAC is feasible. The physical and chemical deficiencies, however, have to be kept in mind at all times, when analysing the simulation. In terms of the model physics the results are most sensitive to the tropopause region, while the chemical deficits mostly concern altitudes above 40 km.





# Chapter 5

## Analysis of stratospheric water isotope ratios

### 5.1 Time series of stratospheric $\delta D(H_2O)$

Variations over time in stratospheric water vapour during the last decades have been observed consistently by various instrumentations. The reasons for these variations are much discussed (see e.g. Hurst et al., 2011; Dessler et al., 2013; Randel and Jensen, 2013). Before analysing these changes with the EMAC model using the newly implemented HDO, it has to be assured that the SD\_REF simulation features the main characteristics of the changes in stratospheric water vapour from 1990 to 2011. Therefore, the equatorial water vapour mixing ratios at 30 km altitude of the simulation are compared with a combined HALOE (HALogen Occultation Experiment) and MIPAS data set in Fig. 5.1. A two year running mean was calculated for both time series in order to make the trends more visible. Additionally, a third trend line (red) was included into the figure for the EMAC data, processed with a low pass filter, to smooth out some of the short term changes.

The combined HALOE/MIPAS observations show an increase in stratospheric water vapour in the first half of the 1990s and a plateau hereafter until the year 2000. The water vapour mixing ratio drops by around  $0.3 \mu\text{mol/mol}$  between 2000 and 2002 and stays at this lower level until the middle of the first decade of the 21st century. Hereafter, a slow increase can be observed until the end of the time series in 2012. This behaviour of stratospheric water vapour during the previous decades has been reported and discussed e.g., by Randel and Jensen (2013) analysing combined HALOE and MLS (Microwave Limb Sounder) data, and is strongly connected to tropopause temperatures.

The EMAC simulation generally reproduces these variations, although with a constant offset and a few differences. The drop around the year 2001 is preceded by a short increase in water vapour. This increase, however, is smoothed out when using the three year low pass filter. Moreover, in contrast to the satellite observations, the level of the water vapour mixing ratio after the drop does not fall below the level from before the increase in the early 1990s.

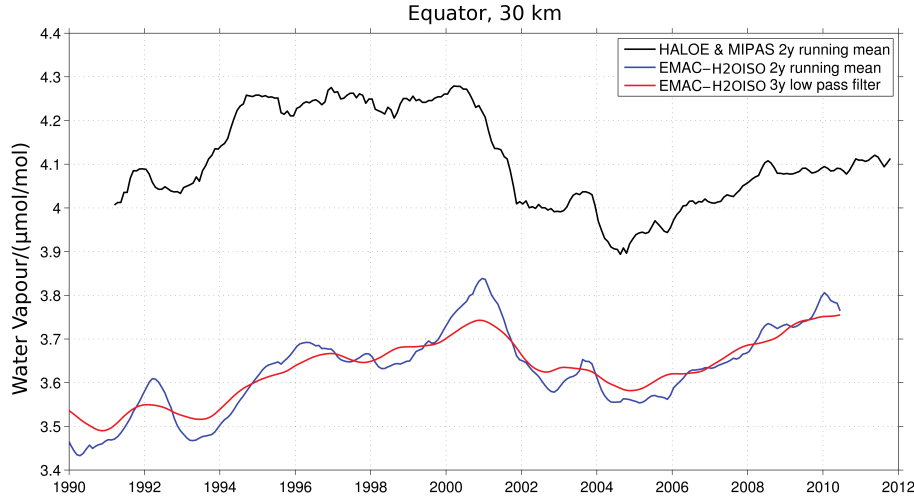


Figure 5.1: Time series of stratospheric water vapour at the equator at 30 km altitude. Combined HALOE and MIPAS data and the EMAC SD\_REF simulation. Created by S. Lossow (personal communication, 2014).

In order to estimate the correlation between the changes of water vapour and its isotopic composition, the anomalies of the tropical water vapour mixing ratio and  $\delta D(H_2O)$  are shown in Fig. 5.2 for the 21 years of the SD\_REF simulation in 18 km and in 30 km, respectively. The data was again processed with a two year running mean, in order to obtain a better visibility of the trends. The anomaly of  $\delta D(H_2O)$  is scaled with  $1/30$  for better comparability.

At 18 km altitude, the Pearson's correlation (see Sect. 5.3) between the two time series is 0.5755 and this correlation decreases to 0.2740 at 30 km. At 18 km altitude, the troposphere-stratosphere exchange processes are still determining for both quantities. At 30 km altitude, the chemical effects are dominating. A dependence of the two quantities can be observed at both altitudes, although, some developments of  $\delta D(H_2O)$  over time demonstrate that the two values react differently on certain changes. The drop around the year 2001 can be seen in water vapour and in  $\delta D(H_2O)$  at both altitudes. At 18 km, the more pronounced feature in  $\delta D(H_2O)$ , however, is the short increase before the drop. The amplitude of this increase in  $\delta D(H_2O)$  exceeds the amplitude of the drop almost by a factor of 2. Even though most of the time the variations of the two quantities are oriented similarly, the sign of the anomalies is sometimes opposing. At 18 km altitude,  $\delta D(H_2O)$  is generally at a lower level at the end of the 1990s compared to the early 2000s, after the drop. Especially the short term changes seem to be pronounced differently in the two quantities. This suggests, that the processes that control stratospheric  $\delta D(H_2O)$  are related, but not equal to those that control the stratospheric water vapour budget. The tropopause temperatures, methane oxidation, convective activity or other processes determining water vapour in the stratosphere are thus affecting stratospheric  $H_2O$  and  $\delta D(H_2O)$  with different strengths. Knowledge of this behaviour can therefore assist to address the origin of certain variations and trends to changes in specific processes. The next sections are therefore aiming on working out the influence of individual processes on stratospheric  $\delta D(H_2O)$ .

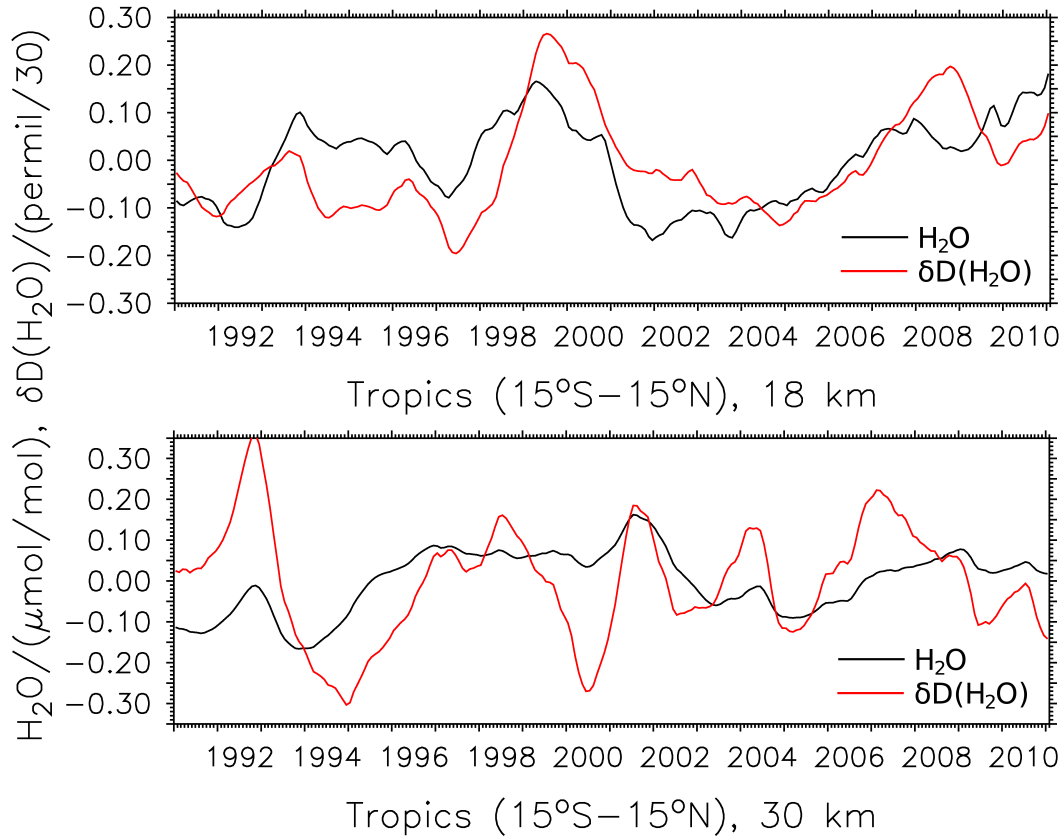


Figure 5.2: Time series of stratospheric water vapour (black) and  $\delta D(H_2O)$  (red) anomalies at 18 km and in 30 km altitude of the SD\_REF simulation, processed with a two year running mean.

## 5.2 The impact of methane oxidation on $\delta D(H_2O)$

As already indicated in Sect. 4.3.4, methane oxidation, besides its effect on the overall stratospheric budget of  $H_2O$  and  $HDO$ , also has an influence on the patterns of stratospheric  $\delta D(H_2O)$ . In order to analyse the impact of the contribution of  $CH_4$  and  $CH_3D$  oxidation on the  $\delta D(H_2O)$  tape recorder signal, an additional simulation (SD\_NOCD) was conducted with the EMAC model. The idea for this sensitivity simulation is an artificial deactivation of the chemical fractionation effects. From the SD\_REF simulation, which was described in Sect. 3.4.2, this simulation differs in only one point: The calculation of the chemical contribution to the tendency of  $HDO$  ( $\frac{\partial(HDO)}{\partial t}|_C$ ) was implemented in a modified manner. With the aim to suppress the influence of methane oxidation on  $\delta D(H_2O)$ , the following approach was introduced:

$$\delta D'_{ac}(H_2O) = \delta D_{bc}(H_2O). \quad (5.1)$$

Here  $\delta D'_{ac}(H_2O)$  represents the modified  $\delta D(H_2O)$  value after the addition of the chemical tendencies of  $HHO$  and  $HDO$  to their total tendencies and  $\delta D_{bc}(H_2O)$  stands for  $\delta D(H_2O)$  before this operation. In order to fulfil this condition, a modified calculation of the chemical

HDO tendency was implemented into the H2OISO submodel. Considering the  $\delta$ -notation from Eq. 2.14, Eq. 5.1 gives

$$\left[ \frac{\left( \frac{HDO + \frac{\partial(HDO)}{\partial t}|_T \cdot \Delta t + \frac{\partial(HDO)}{\partial t}|_{C'} \cdot \Delta t}{HHO + \frac{\partial(HHO)}{\partial t}|_T \cdot \Delta t + \frac{\partial(HHO)}{\partial t}|_C \cdot \Delta t} \right)}{R_{VSMOW}} - 1 \right] \cdot 1000 =$$

$$\left[ \frac{\left( \frac{HDO + \frac{\partial(HDO)}{\partial t}|_T \cdot \Delta t}{HHO + \frac{\partial(HHO)}{\partial t}|_T \cdot \Delta t} \right)}{R_{VSMOW}} - 1 \right] \cdot 1000, \quad (5.2)$$

with  $\frac{\partial(HDO)}{\partial t}|_T$  and  $\frac{\partial(HHO)}{\partial t}|_T$  denoting the total tendencies before the addition of the chemical tendencies for the HDO and the HHO tracer, respectively.  $\frac{\partial(HDO)}{\partial t}|_C$  stands for the chemical tendency of the HHO tracer and  $\frac{\partial(HDO)}{\partial t}|_{C'}$  for the modified chemical tendency of the HDO tracer.  $HDO$  and  $HHO$  represent the values of the respective tracers from the previous time step and  $\Delta t$  the time step. Solving Eq. 5.2 for  $\frac{\partial(HDO)}{\partial t}|_{C'} \cdot \Delta t$  leads to

$$\frac{\partial(HDO)}{\partial t}|_{C'} \cdot \Delta t = \frac{\left( HDO + \frac{\partial(HDO)}{\partial t}|_T \cdot \Delta t \right) \left( HHO + \frac{\partial(HHO)}{\partial t}|_T \cdot \Delta t + \frac{\partial(HHO)}{\partial t}|_C \cdot \Delta t \right)}{HHO + \frac{\partial(HHO)}{\partial t}|_T \cdot \Delta t}$$

$$- HDO - \frac{\partial(HDO)}{\partial t}|_T \cdot \Delta t \quad (5.3)$$

for the modified chemical tendency of HDO. This modified chemical HDO tendency is always consistent with the chemical tendency of HHO, but  $\delta D(H_2O)$  does not become influenced by methane oxidation. In other words, in this sensitivity simulation,  $CH_4$  and  $CH_3D$  have the same lifetimes. This calculation can provide an insight into the sensitivity of stratospheric  $\delta D(H_2O)$  on the oxidation of  $CH_4$  and  $CH_3D$ .

For the analysis of the impact of methane oxidation on the  $\delta D(H_2O)$  tape recorder signal, the SD\_NOCD simulation with the above described modified HDO tendency is compared with the SD\_REF simulation with regular methane isotope chemistry (see Sect. 3.3.6). The setup is the same for both simulations, as described in Sect. 3.4.2. Fig. 5.3 and Fig. 5.4 show the tropical tape recorder signal from 2004 to 2009 for the two simulations from 15 to 30 km. Please note, that for clarity, the images in this chapter are labelled with “H<sub>2</sub>O-vap” for water in the vapour phase and with “H<sub>2</sub>O-ice” for water as ice.

Between 15 and 20 km the  $\delta D(H_2O)$  values are similar in both figures. The tropical tropopause layer and the lower stratosphere are only weakly affected by the chemistry. From 20 km upwards, increasingly higher  $\delta D(H_2O)$  values can be observed in the SD\_REF simulation. The effect of the chemistry on  $\delta D(H_2O)$  increases with height in the stratosphere. This can be observed for the increased  $\delta D(H_2O)$  values, which emerge during northern hemispheric (NH) summer, as well as for the low  $\delta D(H_2O)$  values from the NH

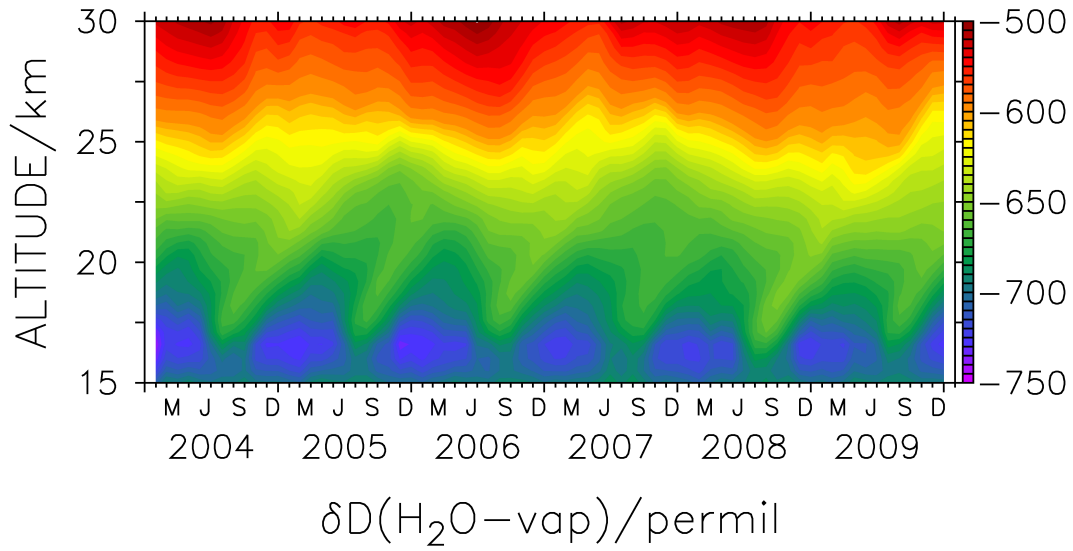


Figure 5.3: Tropical ( $15^{\circ}\text{S}$ - $15^{\circ}\text{N}$ )  $\delta D(H_2O)$  tape recorder signal from 2004 to 2009 in the SD\_REF simulation including the effect of methane oxidation on  $\delta D(H_2O)$ .

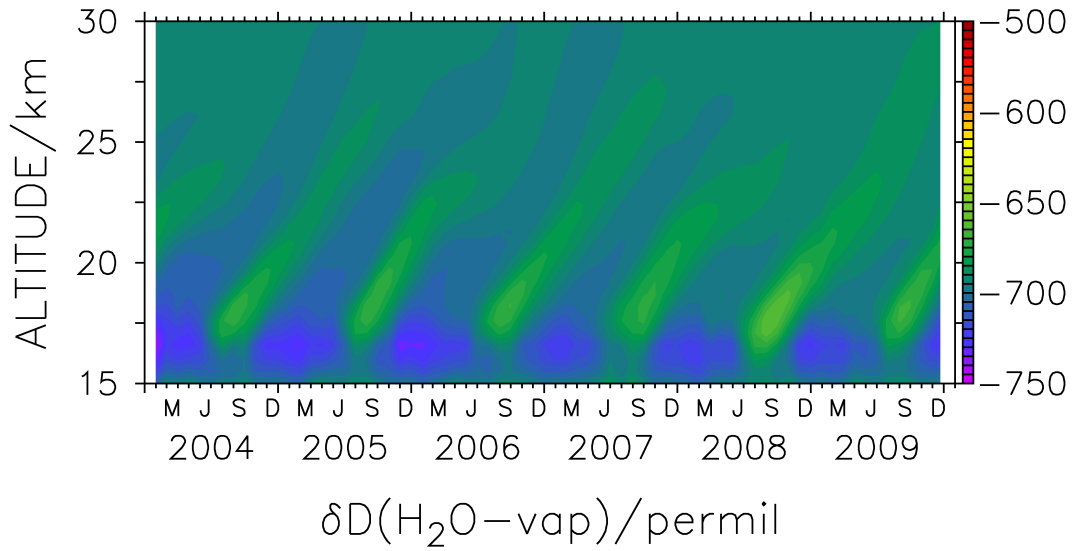


Figure 5.4: Tropical ( $15^{\circ}\text{S}$ - $15^{\circ}\text{N}$ )  $\delta D(H_2O)$  tape recorder signal from 2004 to 2009 in the SD\_NOCD simulation without the effect of methane oxidation on  $\delta D(H_2O)$ .

winter signal. The tape recorder signal in the SD\_NOCD simulation is stronger and reaches higher up than in the SD\_REF simulation. It is still present, although weak, at the top of the figure at around 30 km altitude. In the SD\_REF simulation the tape recorder signal above 25 km is entirely overshadowed by high  $\delta D(H_2O)$  values, which are generated by the isotope effects during methane oxidation. The upward propagating signatures fade out, or rather mix in with the high  $\delta D(H_2O)$  values. The chemical effect dominates at higher altitudes.

For a better quantification of the differences of the two tape recorder signals, Fig. 5.5 shows the result of the subtraction of  $\delta D(H_2O)$  of the SD\_NOCD from the SD\_REF simulation. For guidance, the  $\delta D(H_2O)$  tape recorder signal of the SD\_NOCD simulation is contoured over the colours with dashed lines.

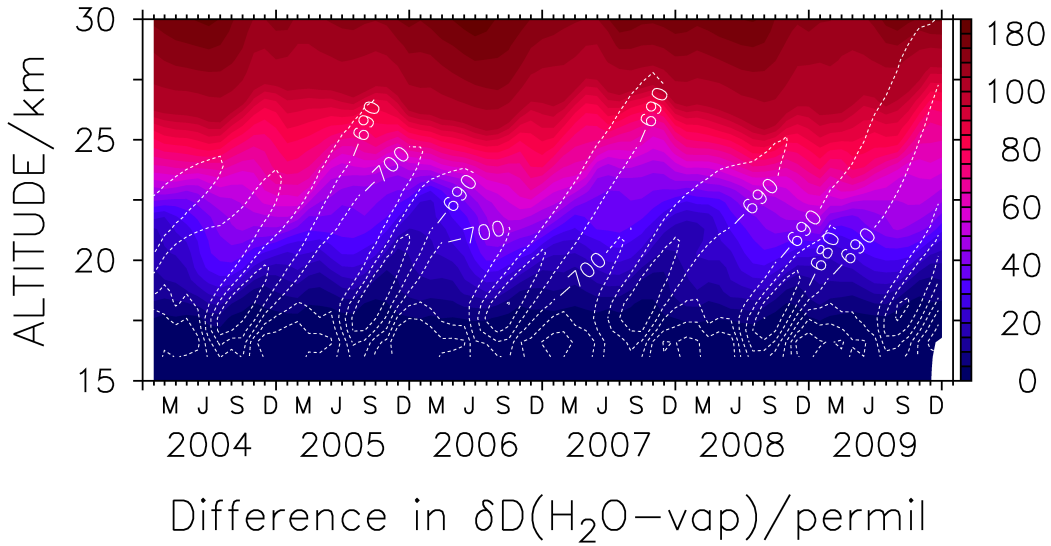


Figure 5.5: Differences in the tropical ( $15^{\circ}S-15^{\circ}N$ )  $\delta D(H_2O)$  values between the simulations with and without (SD\_REF minus SD\_NOCD) the effect of methane oxidation on  $\delta D(H_2O)$ . For guidance, the dashed contour lines show the tape recorder signal from the SD\_NOCD simulation from Fig. 5.4.

The difference in  $\delta D(H_2O)$  is increasing with altitude from 0‰ in 15 km to 180‰ at 30 km. Furthermore, the difference shows a wavy structure with the highest amplitude of the waves between 18 and 23 km. Below and above this region, the differences are thus fairly constant over time. Below 18 km, the methane oxidation is very weak and above 23 km, it is the dominating effect. Between 18 and 23 km, a concurrence between low differences and high  $\delta D(H_2O)$  values in the contour lines can be observed. The high values from the NH summer signal are not affected as strongly by methane oxidation as the low values from the NH winter signal. To explain this, constant temperatures, and hence fractionation factors, and a constant background  $\delta D(CH_4)$  are assumed, which is reasonable here. The isotope ratios of isotopically different reservoirs possess different sensitivities to the addition of a compound with a certain isotope ratio. This means that, the smaller the

differences between the  $\delta$  values are, the smaller is the alteration. Since the high  $\delta D(H_2O)$  values from the NH summer signal are closer to the  $\delta D(CH_4)$  values, which are around  $-50\text{‰}$  here, compared to the low  $\delta D(H_2O)$  values from NH winter, the summer signal is altered less. Additionally, also the water vapour mixing ratios are different here. The  $\delta D$  values of the low water vapour mixing ratios from the NH winter signal are therefore again affected stronger by the addition of (a similar amount of) isotopically enriched water vapour from methane oxidation. This concludes that the production of  $H_2O$  and  $HDO$  by the oxidation of  $CH_4$  and  $CH_3D$ , reduces the amplitude of the  $\delta D(H_2O)$  tape recorder and overshadows the upward propagation of the signal.

In order to illustrate this finding more quantitatively, Fig. 5.6 shows the averaged amplitudes of the  $\delta D(H_2O)$  tape recorder signals with altitude. The black line denotes the SD\_REF simulation and the red line the SD\_NOCD simulation.

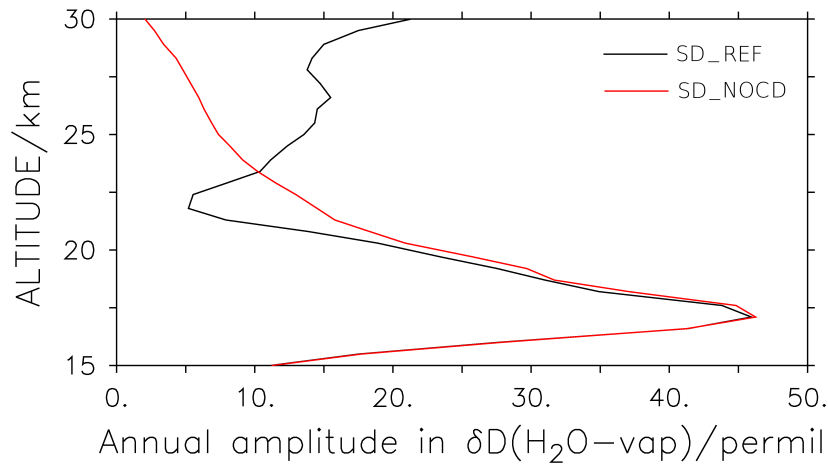


Figure 5.6: Averaged annual amplitudes of  $\delta D(H_2O)$  with altitude, with (black) and without (red) the effect of methane oxidation on  $\delta D(H_2O)$ .

The tape recorder amplitudes are equal up to the lower stratosphere. As expected, further above, the amplitude of the simulation with chemistry effect on  $\delta D(H_2O)$  decreases faster with altitude than the amplitude of the SD\_NOCD simulation. Above 23 km, the amplitude of the SD\_REF simulation exceeds the amplitude of the simulation without chemistry effect on  $\delta D(H_2O)$ . This, however, is not due to the tape recorder effect anymore. It is due to variations in the downward propagation of isotopically enriched water vapour from the upper stratosphere, possibly a consequence of the QBO.

### 5.3 The origin of the $\delta D(H_2O)$ tape recorder

In order to analyse the origin of the  $\delta D(H_2O)$  tape recorder signal, zonal and seasonal averages, averaged over the 21 years of the SD\_REF simulation are presented in Fig. 5.7 between 10 and 30 km. The black lines in the images show the tropopause height and the blue contour lines represent constant potential temperatures for MAM (March, April, May), JJA (June, July, August), SON (September, October, November) and DJF (December, January, February).

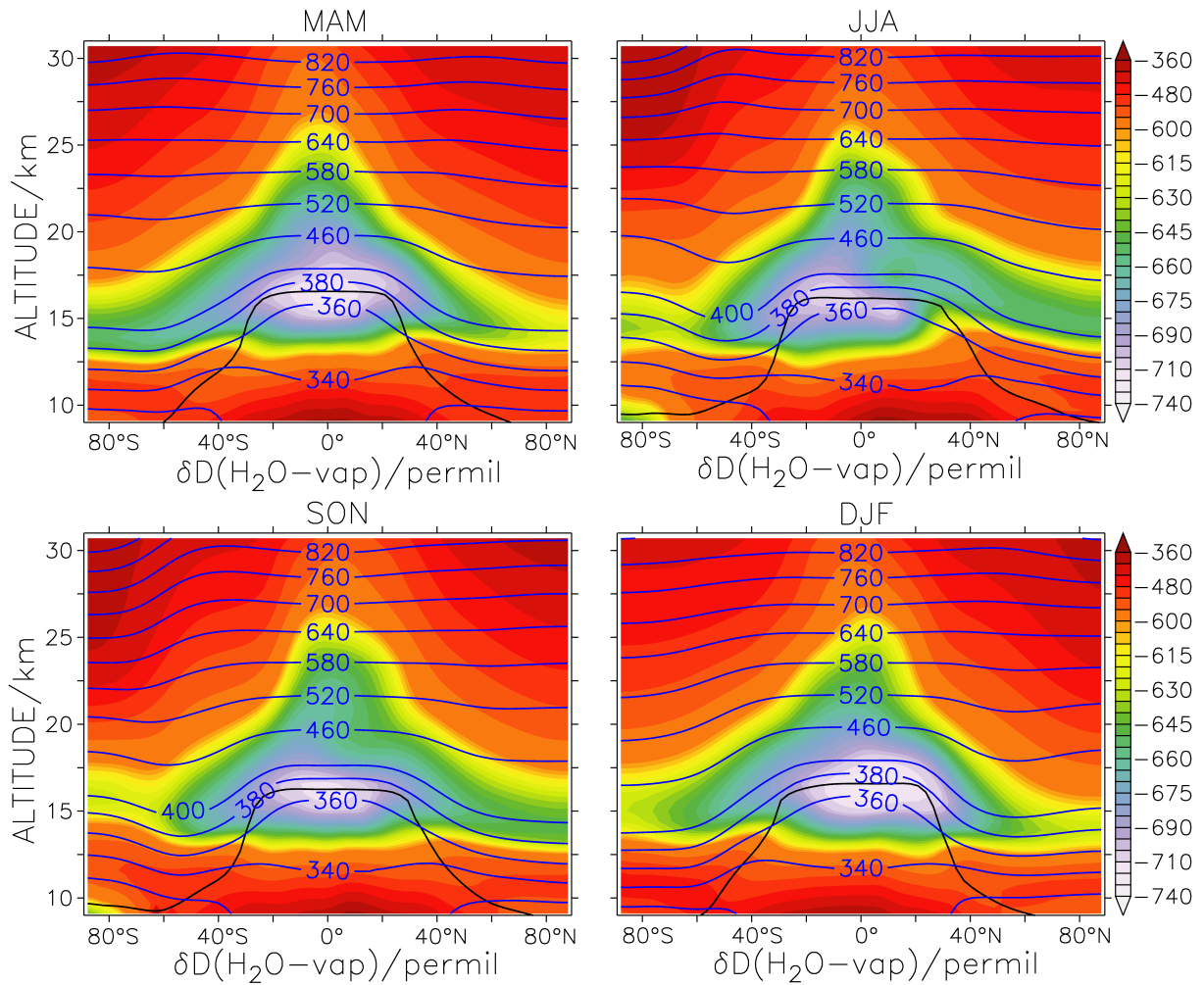


Figure 5.7: Zonally and seasonally averaged  $\delta D(H_2O)$  (coloured), tropopause height (black lines) and isentropes (blue contour lines) in K, averaged over the 21 years of the SD\_REF simulation.

A similar pattern with high  $\delta D(H_2O)$  values in the troposphere and a steep transition to isotopically depleted water vapour, between the 360 and the 380 K isentrope in the extratropics and between the 340 and the 360 K isentrope in the tropics, can be observed during all the seasons. Moreover, the minima  $\delta D(H_2O)$  are always found around the tropical tropopause, with the lowest values during DJF and MAM. The minima spread out to the



poles during the respective summers and autumns at around 15 km. Additionally, a local minimum can be seen during JJA and SON at around 15 km over the southern polar region, associated with the antarctic polar vortex. In the stratosphere, the water isotope ratios increase with altitude and latitude. The main drivers for that stratospheric distribution are the Brewer-Dobson Circulation (BDC) and the methane oxidation.

In the tropics a rather symmetric structure around the equator can be seen in MAM. In JJA, a lifted signal of high tropospheric isotope ratios can be observed around 40°N. At the edge of the tropical tropopause layer, this isotopically enriched water vapour penetrates along the isentropes, through the tropopause, into the tropical pipe. Upward motion in the tropics transports the maximum of this signal across the isentropes, from around 17 km in JJA to 19 km in SON and to 21 km in DJF, where it fades out and is only hardly visible. In JJA, slightly enhanced, slowly upward moving  $\delta D(H_2O)$  values can also be seen in the northern extratropics between 15 and 18 km. These, however, mix in with the chemically enhanced  $\delta D(H_2O)$  values much quicker than in the tropics and are already not visible anymore in SON.

In this illustration of the  $\delta D(H_2O)$  tape recorder, the origin of the enhanced isotope ratios in the tropical lower stratosphere during JJA, can clearly be associated with elevated isotopically enriched water vapour in the northern hemispheric troposphere. A similar lofting of isotopically rich, tropospheric air can also be observed during DJF at around 40°S. However, this signal is at considerably lower altitudes and does not penetrate into the tropical pipe.

When entering the lower stratosphere, air experiences rapid transport between the tropics and the mid-latitudes above the subtropical jets (Rosenlof et al., 1997). The region between the 380 and the 400 K isentrope is therefore crucial for the properties of stratospheric air. Fig. 5.8 shows the zonally and temporally averaged (over the 21 years of the simulation) annual cycle of  $\delta D(H_2O)$  between the 380 and the 400 K isentropes.

The tropical minimum in  $\delta D(H_2O)$  drifts from 15°N during NH winter to 15°S during NH summer, with the lowest values during NH winter. The signal of increased isotope ratios during NH summer, across the entire northern hemisphere, starts during NH spring in the mid-latitudes, reaches the equator in NH summer and fades out hereafter. In the southern hemisphere, the analogue signal is considerably weaker and does not reach the tropics. This seasonal cycle within the tropics represents the stratospheric  $\delta D(H_2O)$  tape recorder signal of the lower stratosphere.

To provide an insight into the dynamics of this region, the same values are shown in a latitude-longitude representation divided into the seasons of Fig. 5.9. Additionally, the horizontal wind vectors are included in the figures as arrows and the blue lines indicate the height of the tropopause.

In general, these figures feature a pattern with low  $\delta D(H_2O)$  in the tropics and increasing values with higher latitudes. In MAM and SON, the pattern is relatively symmetric around the equator, with higher  $\delta D(H_2O)$  in the high latitudes during spring. The southern polar region shows the isotopically most enriched water vapour during DJF, while in JJA  $\delta D(H_2O)$  is similar in both polar regions. In JJA, the high isotope ratios in the northern hemisphere reach further towards the tropics compared to those in DJF in the southern hemisphere. Moreover, in JJA, patterns can be observed, which are associated with the

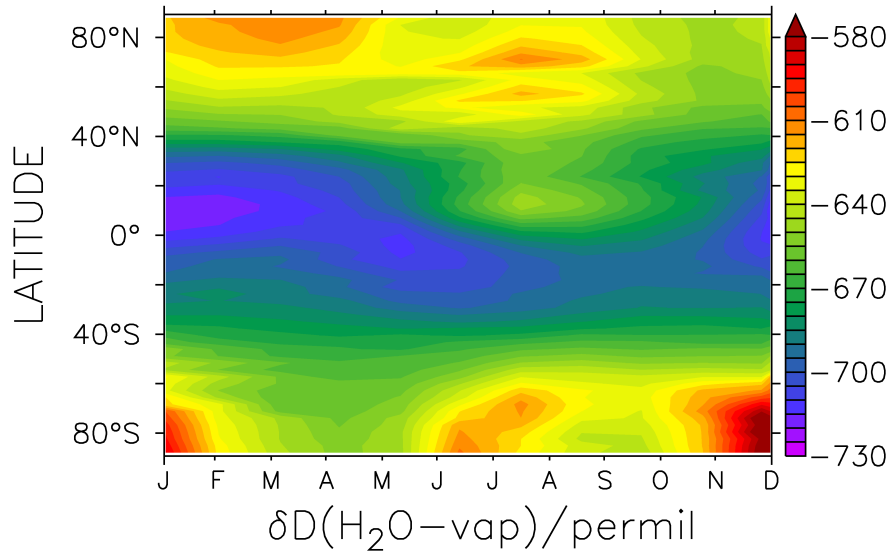


Figure 5.8: Zonal averages of monthly  $\delta D(H_2O)$ , averaged over the 21 years of the SD\_REF simulation, from the 380 to the 400 K isentrope.

Asian Summer Monsoon (ASM), as well as with the North American Monsoon (NAM). High  $\delta D(H_2O)$  values can be seen over the entire North American continent. Over southern Asia, in contrast, very low values are dominant. Around this isotopically depleted centre of the ASM anticyclone, the water vapour is isotopically enriched. Over the Western Pacific the wind vectors indicate a considerable southward component, which drags isotopically enriched air from the extratropics towards the tropics and westwards hereafter. This air originates from the westerly wind regime at around  $40^\circ N$  over the Asian continent, because a high potential vorticity gradient north of this region prevents meridional air mass exchange (see e.g. Plumb, 2002). In the western pacific region, furthermore, a lowering of the tropopause is evident. This is likely to be the region where water vapour can enter the stratosphere.

In order to identify the origin of the high  $\delta D(H_2O)$  values over the western pacific, a longitudinal cross section, averaged from  $30^\circ N$  to  $40^\circ N$  is presented in Fig. 5.10. Additionally, the tropopause (black line) and the isentropes (red lines) are included in the figure.

Here, the highest values can be found near the tropopause, at around  $100^\circ E$ , above the Himalaya mountains. Another, yet weaker, maximum lies at around  $100^\circ W$ , which is the location of the Mexican High Plateau and the NAM. A third, even weaker maximum at  $0^\circ E$  can be associated with the North African Monsoon. The lowest values are accompanied by the highest parts of the tropopause at around 16 km of height at  $50^\circ E$ . This is also where the temperatures are lowest (not shown). The tropopause height exhibits two minima, one at  $160^\circ W$  and one at  $10^\circ W$ . In these minima, the highest stratospheric  $\delta D(H_2O)$  values are found. The underlying westerly wind regime (shown in Fig. 5.9, JJA), connected with the tropopause-crossing isentropes in the subtropics, is thus confirming, that the enhanced stratospheric isotope ratios during JJA originate from monsoonal (Asian and American)

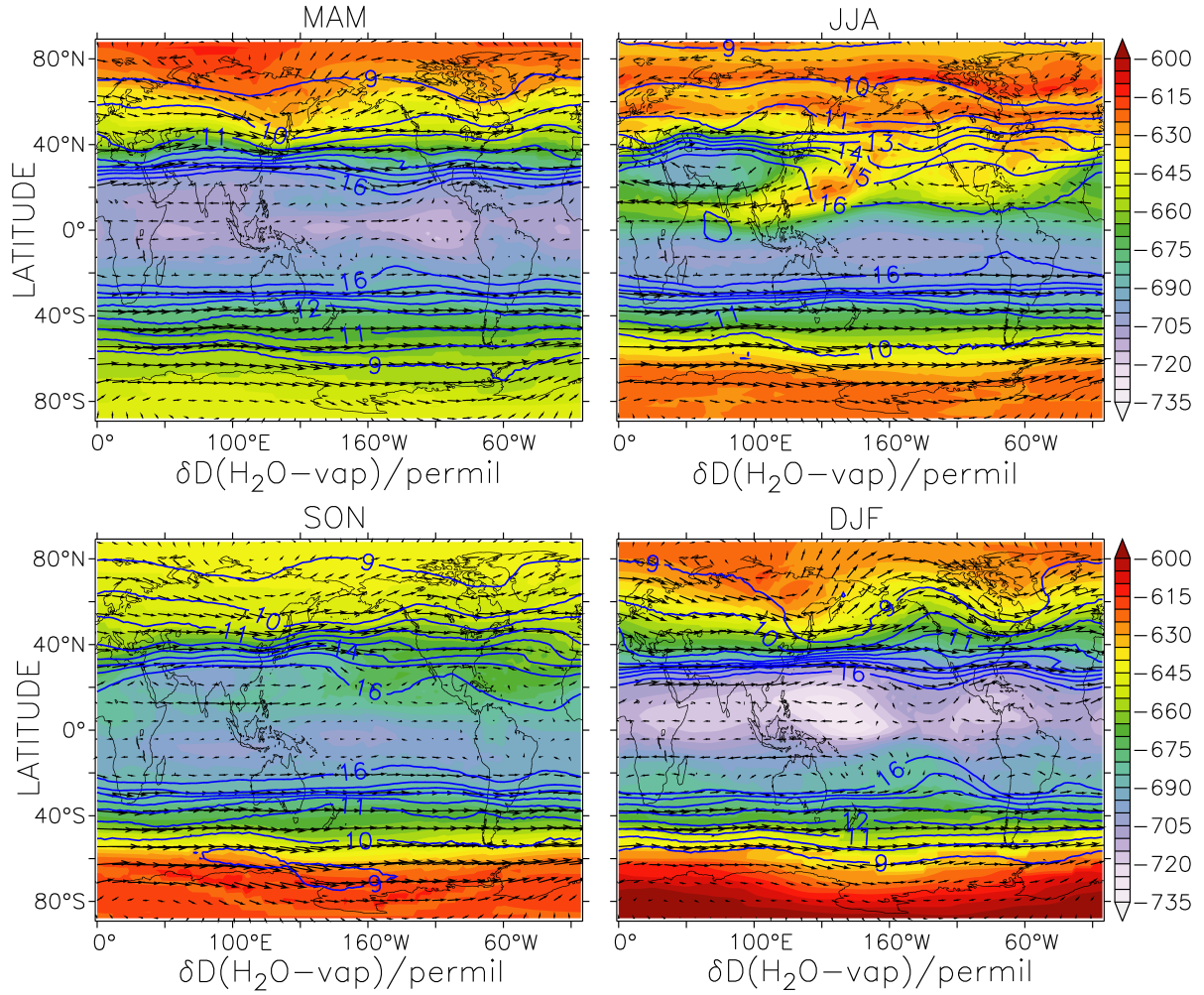


Figure 5.9: Seasonally averaged  $\delta D(H_2O)$  (colours), horizontal wind vectors (arrows) averaged from the 380 to the 400 K isentrope and the tropopause height (blue contour lines), averaged over the 21 years of the SD\_REF simulation.

activity. Isentrope-crossing upward motion of the isotopically enhanced water vapour in this region can be explained with strong gravity wave activity, taking place within the jetstreak at the forefront of the ASM anticyclone (see e.g., Reid and Gage, 1996).

These high  $\delta D(H_2O)$  values are much more pronounced for the ASM and referring to Fig. 5.9, only the Western Pacific region provides a strong enough northerly wind component, which can transport this isotopically enriched water vapour into the tropics. This suggests, that the JJA signal of the stratospheric tape recorder, which propagates upwards over time, is mainly generated by the ASM.

In order to confirm this assumption, Fig. 5.11 shows the difference in  $\delta D(H_2O)$  between the two main monsoon regions (a subtraction of the average of 140°W to 40°W from the average of 80°E to 180°E). In other words, the ASM region minus the NAM region. For guidance, the tropopause and the isentropes (averaged globally) are included here as

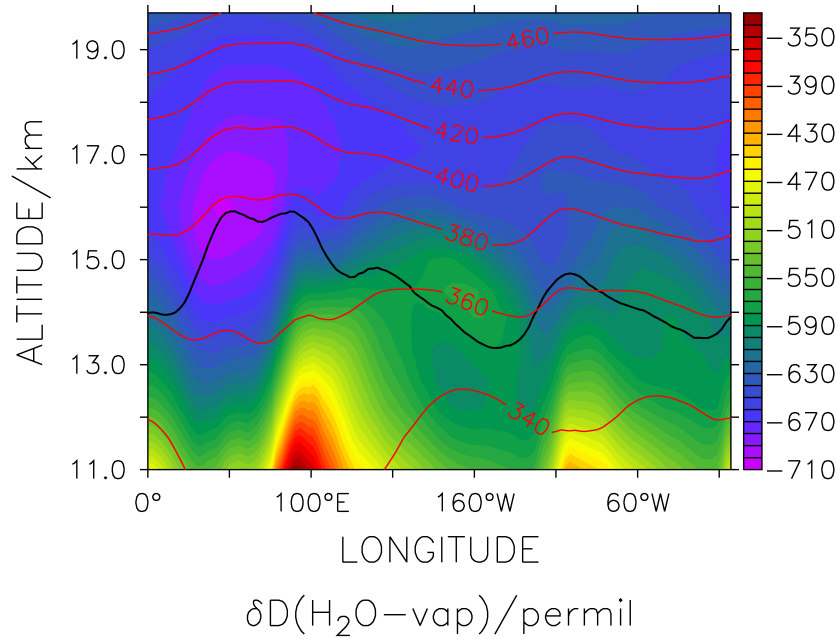


Figure 5.10: Zonal cross section of  $\delta D(H_2O)$ , averaged from 30°N to 40°N for JJA (averaged over the 21 years of the SD\_REF simulation). The black line denotes the tropopause height, the red contour lines indicate levels of constant potential temperatures (isentropes).

well. Positive values indicate higher  $\delta D(H_2O)$  in the Western Pacific, negative values show enhanced  $\delta D(H_2O)$  in the American region.

The most dominant feature of the figure is the patch of very high values in the northern TTL, between 12 km and the top of the tropopause. This indicates, that convective activity is much stronger in the Western Pacific region than in the American region. Another region with high values can be found above the tropical tropopause at around 17 km altitude. This confirms that the Western Pacific region is dominant for the emergence of high  $\delta D(H_2O)$  values in the tropical lower stratosphere during JJA. The patch with negative values between 30°N and 50°N and 15 and 17 km, suggests that the lack of the northerly wind component in the American region, leaves more isotopically enriched water vapour at the higher altitudes of the American extratropics.

In order to corroborate the hypothesis, that ASM activity is crucial for the enhanced  $\delta D(H_2O)$  of the tropical tape recorder signal in JJA, a correlation analysis was carried out. For that, the anomalies of the  $\delta D(H_2O)$  values between the 370 and the 390 K isentropes in the subtropical Western Pacific (15°N to 40°N and 120°E to 140°W) region and in the subtropical American and Western Atlantic region (15°N to 40°N and 120°W to 20°W) were correlated with the anomalies of the tropical tape recorder signal in the stratosphere for the 21 years of the SD\_REF simulation. Fig. 5.12 shows the  $\delta D(H_2O)$  values between the 370 and the 390 K averaged over the 21 years of the model simulation. The described regions are framed. The regions were selected to be north (15°N) of the tape recorder signal and below the altitude of its maximum, in order not to take the starting region of the tape recorder itself into account.

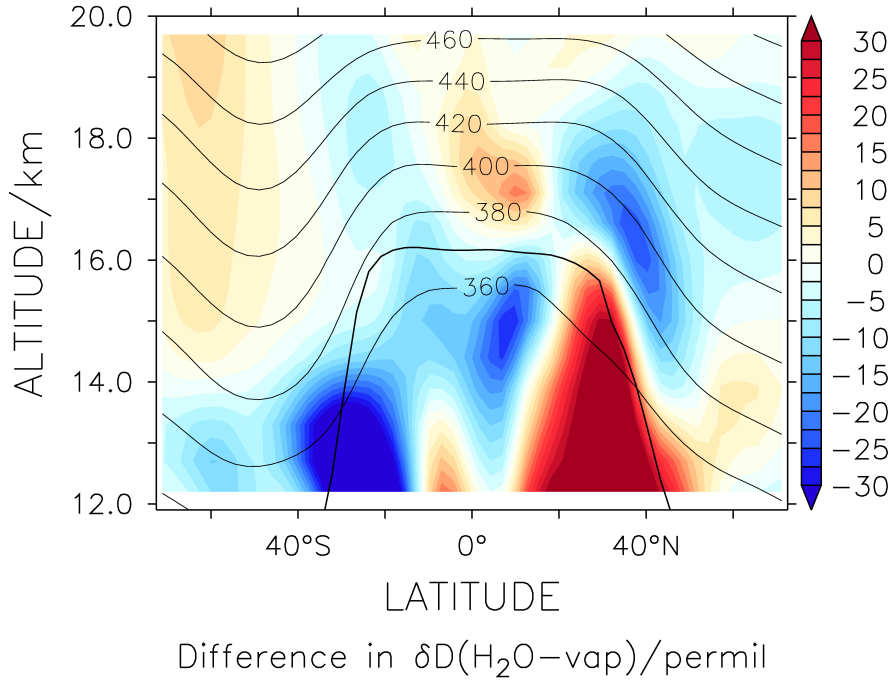


Figure 5.11: Difference in  $\delta D(H_2O)$  between the zonal average from  $80^\circ E$  to  $180^\circ E$  and from  $140^\circ W$  to  $40^\circ W$  for JJA (ASM minus NAM). The thick line shows the zonally averaged tropopause and the thin contour lines denote the isentropes (both globally averaged).

The correlations were calculated by using one  $\delta D(H_2O)$  value per year for the ASM activity (the average over JJA in the above described regions, hereafter called  $P$ ) and the  $\delta D(H_2O)$  value at every altitude level for each month separately per year (hereafter called  $Q$ ). For these values, the Pearson's correlation coefficient  $\rho(P, Q)$  is determined by

$$\rho(P, Q) = \frac{cov(P, Q)}{\sigma(P)\sigma(Q)} = \frac{E[(P - \mu(P))(Q - \mu(Q))]}{\sqrt{E[(P - \mu(P))^2]} \sqrt{E[(Q - \mu(Q))^2]}}, \quad (5.4)$$

where  $cov$  represents the covariance,  $\sigma$  the standard deviation,  $E$  the expectation and  $\mu$  the mean.

The results are shown in Fig. 5.13. Since the Monsoon signals for the correlation are taken from JJA, the time axes of the figures start in June. The tape recorder values for the correlation for the months of January to May are always taken from the subsequent year of the ASM signal.

The left panel of Fig. 5.13 shows a tape recorder signal in the correlation coefficients of the ASM with the tape recorder signal. While in general this correlation shows values between -0.2 and 0.2, a stripe from 18 km in July to 23 km in April exhibits enhanced correlation values. The highest values, which reach a correlation of up to 0.7 can be seen from July to September between 18 and 19 km. In the following months this “correlation tape recorder” signal weakens with ascent over time and fades out in spring. The right panel of Fig. 5.13 shows the correlation coefficients between the NAM and the tape recorder.

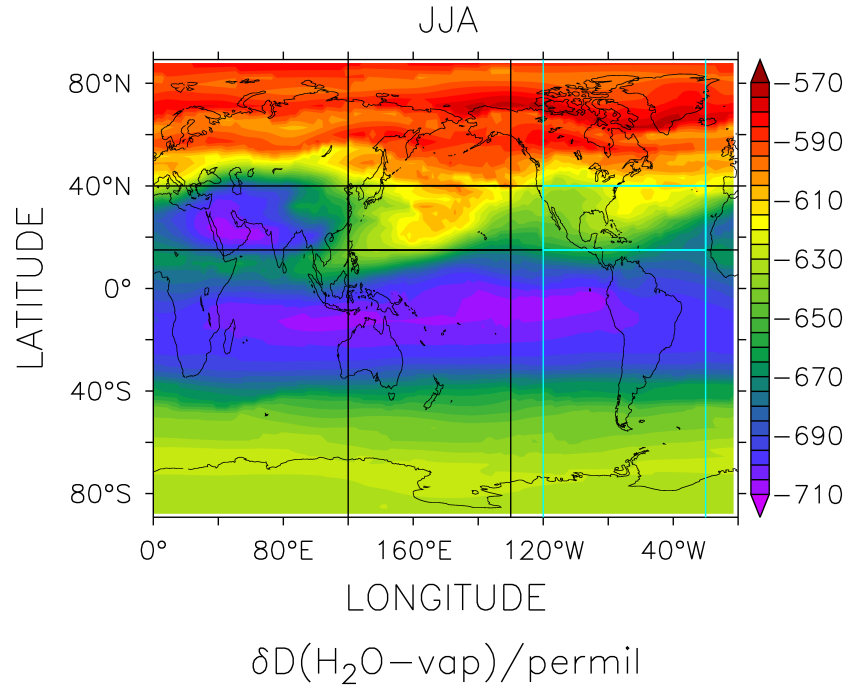


Figure 5.12:  $\delta D(H_2O)$  between the 370 and the 390 K isentropes for JJA, averaged over the 21 years of the SD\_REF simulation. The frame mark the applied regions (black: ASM, blue: NAM) for the correlation analysis with the tape recorder signal.

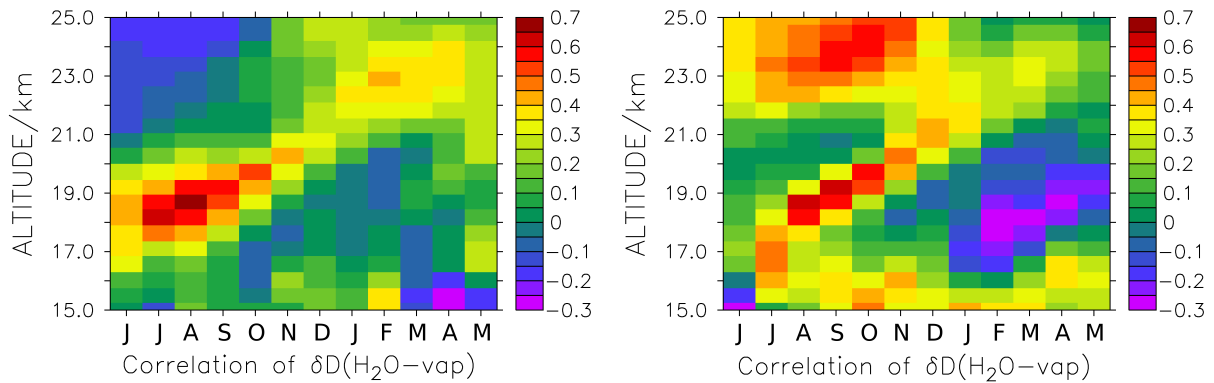


Figure 5.13: Pearson's correlation coefficient between the  $\delta D(H_2O)$  tropical tape recorder signal and the  $\delta D(H_2O)$  ASM (left) and the NAM (right) signal between the 370 and the 390 K isentropes for the 21 years of the SD\_REF simulation.

Here, too, a “correlation tape recorder” signal can be detected, however, with slightly lower correlation coefficients, an earlier fade-out and especially, a smaller region of high correlations during summer in the lower stratosphere. The spot between 22 and 25 km, with high correlation values is rather surprising and thought to be of different nature than the tape recorder signal. The ascent rates of the “correlation tape recorder” match with



the ascent rate of the actual  $\delta D(H_2O)$  tape recorder. This correlation analysis confirms the connection between the strength of the Monsoon systems and the stratospheric tape recorder in  $\delta D(H_2O)$  and corroborates that the ASM is closely related to the tropical  $\delta D(H_2O)$  signature and hence the major driver for the stratospheric  $\delta D(H_2O)$  tape recorder.

## 5.4 The impact of ice lofting on stratospheric $\delta D(H_2O)$

Both, the water vapour mixing ratio and  $\delta D(H_2O)$ , exhibit enhanced values in the lower stratosphere during JJA. The underlying processes for this, however, may differ in some ways for the two quantities. In order to demonstrate this, the water vapour mixing ratio and  $\delta D(H_2O)$  are shown in the upper troposphere, lower stratosphere region (UTLS) in JJA in Fig. 5.14.

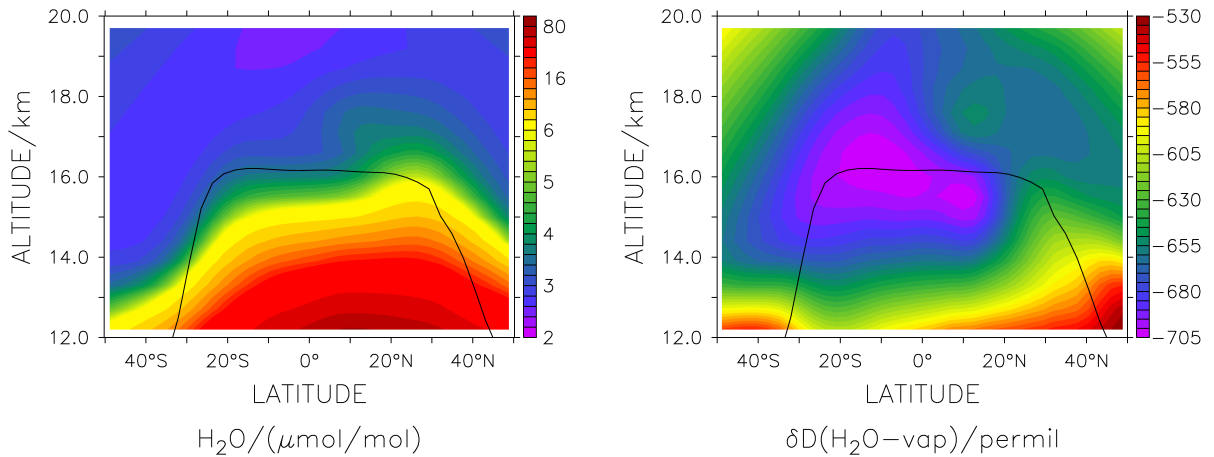


Figure 5.14:  $H_2O$  mixing ratio (left panel) and  $\delta D(H_2O)$  (right panel) in the UTLS in JJA and tropopause height (black line), averaged over the 21 years of the SD\_REF simulation.

Differences in the distribution of the enhanced values can be observed when comparing the two panels. In the left panel, enhanced  $H_2O$  mixing ratios can be seen within almost the entire TTL, however, decreasing with altitude and towards the southern latitudes. At the northern edge of the TTL the large  $H_2O$  values exceed the tropopause and penetrate into the stratosphere. Some water vapour, however, also intrudes into the stratosphere in the central and the southern TTL. Isotopically enhanced water vapour (right panel) exclusively enters the stratosphere at the northern edge of the TTL.  $\delta D(H_2O)$  values of around  $-600\text{‰}$  can be observed crossing the tropopause and entering the tropical pipe here. In the central and southern parts of the TTL, the water vapour is isotopically strongly depleted, exhibiting values below  $-700\text{‰}$ . Low  $\delta D(H_2O)$  can be observed down to 14 km altitude in the central and southern TTL, while enhanced water vapour mixing ratios reach up to almost 16 km altitude in this region.

This suggests that the processes, which elevate the water vapour in the respective regions differ. In order to elucidate this difference, the relation between the water vapour mixing

ratios and  $\delta D(H_2O)$  is presented in Fig. 5.15. The black crosses denote the relation in the northern region ( $10^\circ N$  and  $40^\circ N$ ) and the red crosses in the southern region ( $40^\circ S$  and  $10^\circ S$ ), both in JJA from 14 to 20 km.

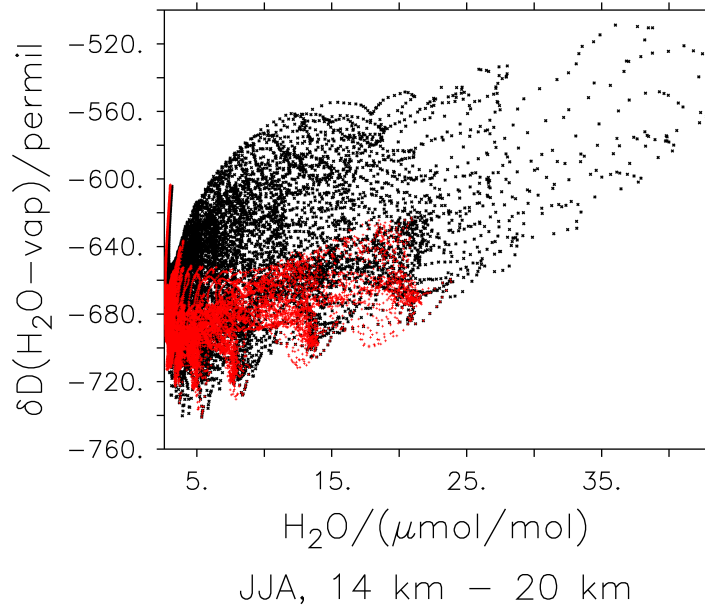


Figure 5.15: Relation between  $H_2O$  and  $\delta D(H_2O)$  from 14 to 20 km in JJA between  $10^\circ N$  and  $40^\circ N$  (black crosses) and between  $40^\circ S$  and  $10^\circ S$  (red crosses), averaged over the 21 years of the SD\_REF simulation.

The red crosses can be found in a  $\delta D(H_2O)$  range between roughly  $-720\text{‰}$  and  $-640\text{‰}$  with water vapour mixing ratios of up to  $20 \mu\text{mol/mol}$ . A slope of increasing  $\delta D(H_2O)$  with increasing water vapour mixing ratios is recognisable. The black crosses cover the range of the southern hemispheric relations as well, but also spread out to larger water vapour mixing ratios and larger  $\delta D(H_2O)$  values. Larger water vapour mixing ratios generally feature enhanced  $\delta D(H_2O)$  here as well, but for the same  $H_2O$  mixing ratios as in the SH, some of the water vapour in the NH is isotopically enriched. The dependencies of  $\delta D(H_2O)$  in water vapour suggests that this is due to different processes connected with clouds and convection in the respective hemispheres. In particular, the much discussed influence of convectively lofted ice crystals (see Sect. 2.1.1) is considered to be a major driver of these patterns.

The ice water content in the UTLS for JJA is shown in Fig. 5.16 in order to reveal interhemispheric differences. Additionally the  $\delta D(H_2O)$  of ice is contoured in the figure and the height of the tropopause is marked. The white regions denote for ice water mixing ratios below  $0.1 \mu\text{mol/mol}$ .

The ice water mixing ratios show two local maxima at altitude in this illustration. One in the inner tropics and another one between  $30^\circ N$  and  $35^\circ N$ . The latter maximum additionally features high  $\delta D(H_2O)$  in ice at high altitudes up to the tropopause. The ice features  $\delta D(H_2O)$  values of up to  $-300\text{‰}$  in these areas, while the isotope ratios of water



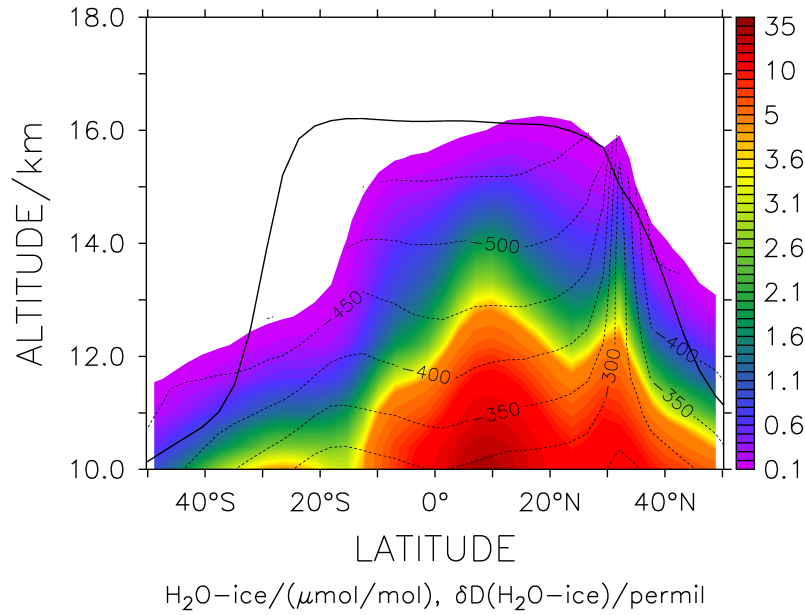


Figure 5.16: Ice water content (colours) and  $\delta D(H_2O)$  in ice (dashed contour lines) in the UTLS in JJA and tropopause height (solid black line), averaged over the 21 years of the SD\_REF simulation.

vapour in this area lie around  $-600\text{‰}$  (see Fig. 5.14). Convectively lofted ice, which re-sublimates here, is therefore likely to be responsible for the isotopical enrichment of water vapour in this region of the TTL. This water vapour hereafter intrudes into the tropical stratosphere and generates the  $\delta D(H_2O)$  tape recorder signal of JJA.

Regarding the analysis of the origin of the tape recorder signal, the corresponding region where the ice lofting takes place is crucial. For this, the ice water content (left panel) and  $\delta D(H_2O)$  (right panel) in ice in JJA at 14 km altitude are shown in Fig. 5.17. The altitude of 14 km was chosen because, as can be seen in Fig. 5.16, at this altitude the inner tropical and the northern subtropical altitude maxima of  $\delta D(H_2O)$  in ice are still pronounced. Regions with ice water mixing ratios below  $0.1 \mu\text{mol/mol}$  are again not taken into account.

The left panel shows several spots of enhanced ice water content around the convective zones in the tropics. Especially high ice water mixing ratios can be seen in Southeast Asia and Middle America, but by far the highest values are found over the Tibetan Plateau.  $\delta D(H_2O)$  in ice exhibits a rather uniform picture around the tropics, with values mostly between  $-500\text{‰}$  and  $-400\text{‰}$ . Only one single spot with isotopically enriched ice water above the Tibetan plateau with values above  $-200\text{‰}$  strikes the eye. This corresponds with the latitude of the altitude maximum in Fig. 5.16 and leads back to Sect. 5.3, where the origin of the JJA signal of the stratospheric tape recorder was traced back to the ASM. Convective activity over the Tibetan Plateau, associated with exceptionally strong ice lofting and thus resulting isotopic enrichment of the upper troposphere can therefore be understood as the starting point of the stratospheric  $\delta D(H_2O)$  tape recorder in the EMAC simulation.

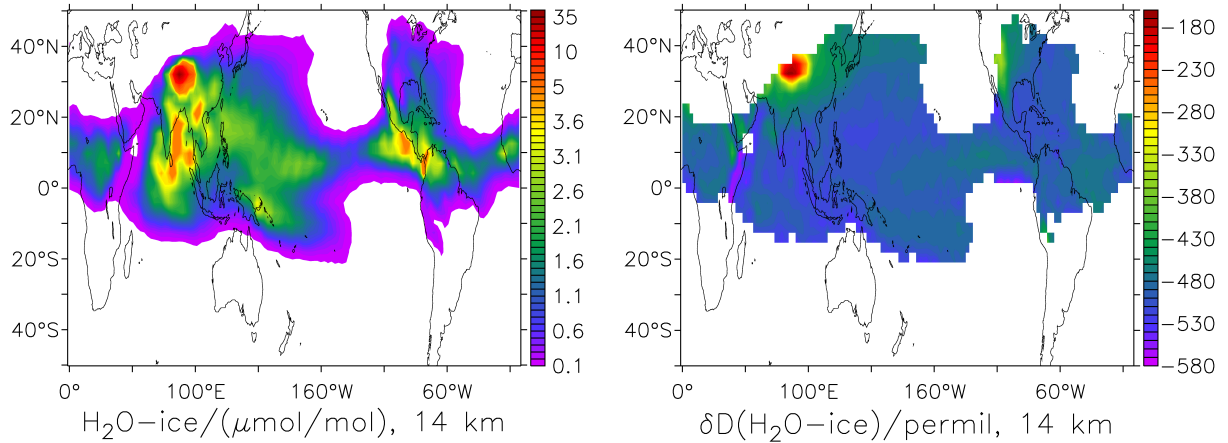


Figure 5.17: Ice water content (left) and  $\delta D(H_2O)$  in ice (right) at 14 km altitude in JJA, averaged over the 21 years of the SD\_REF simulation.

## 5.5 Discussion of the analysis

The comparison of the variations of stratospheric water vapour mixing ratios from 1990 to 2011 between the EMAC SD\_REF simulation and satellite observations have shown that the main characteristics of the changes are reproduced by the model simulation. The time series of  $\delta D(H_2O)$  shows similarities with  $H_2O$ , differs however, mainly regarding short term changes. This suggests that the processes controlling these two quantities coincide, but their effect on the respective value is of different quantity. The changes of stratospheric  $\delta D(H_2O)$  can assist to understand the often discussed reasons for the trends and variations in stratospheric water vapour (see i.e. Hurst et al., 2011). Beforehand, this requires an understanding and quantification of the influence of the individual processes, that are responsible for the development of  $\delta D(H_2O)$  in the stratosphere.

Like water vapour, stratospheric  $\delta D(H_2O)$  is controlled by methane oxidation and the intrusion of water vapour through the tropical tropopause. These two processes were investigated in this study, with a special regard on the stratospheric tape recorder, since the characteristics of this signal are crucial for the stratospheric water vapour budget and hence also for  $\delta D(H_2O)$ . The strong dehydration of the lower stratosphere during DJF and MAM can, to a large extent, be explained by the tropopause temperatures (Randel and Jensen, 2013). Since this freeze drying effect affects HDO even more than  $H_2O$ , also the isotopically depleted water vapour in the lower stratosphere at these times of the year can mainly be attributed to temperature variations. The enhanced water vapour mixing ratios, as well as the high  $\delta D(H_2O)$  values during JJA and SON, have yet several factors of influence. Those have not been quantified sufficiently before and hence are investigated in this study.

The impact of methane oxidation on the stratospheric  $\delta D(H_2O)$  tape recorder signal was tested by comparing the SD\_REF simulation with an additional simulation (SD\_NOCD), with a suppressed chemical effect on  $\delta D(H_2O)$ . The chemistry mainly affects water vapour and its isotopic signature above 25 km, where the  $\delta D(H_2O)$  tape recorder signal fades out faster through this chemical effect. Additionally, the amplitude of the tape recorder is

reduced because methane oxidation influences the low  $\delta D(H_2O)$  values and the low water vapour mixing ratios stronger than the higher ones. This result is not surprising, however, it reveals the impact of the isotope chemistry on the tape recorder.

Randel et al. (2012) also applied a correction for the methane effect on  $\delta D(H_2O)$  to the ACE-FTS satellite retrieval. This lead to the removal of the increase in  $\delta D(H_2O)$  with altitude in the stratosphere as well. Moreover it generated enhanced isotope ratios in the lower stratosphere during JJA and SON, compared to without the methane correction. A tape recorder similar pattern as in the EMAC simulations, however, is still hardly visible.

The signal of enhanced  $\delta D(H_2O)$  during JJA in the lower stratosphere was traced back to its originating region and its determining process in the SD\_REF simulation. The origin of the isotopically enriched water vapour during JJA in the lower stratosphere could be associated with the ASM. This water vapour originates from the Tibetan Plateau, crosses the tropopause over the Western Pacific and there experiences southward transport at the forefront of the ASM anticyclone. The analysis of the correlation coefficient between the anomalies of the  $\delta D(H_2O)$  values in the Monsoon regions and the tape recorder signal in  $\delta D(H_2O)$  corroborated this association. Furthermore it supports the assumption, that the effect of the NAM on the tape recorder is smaller compared to the effect of the ASM. A link between the ASM and the tropical tape recorder in water vapour has already been found by Dethof et al. (1999). The southern flank of the anticyclone moistens the UTLS during JJA and contributes significantly to the stratospheric water vapour budget (Bannister et al., 2004; Gettelman and Kinnison, 2004; Lelieveld et al., 2007; James et al., 2008). Also according to Füglistaler et al. (2004) this side-ways transport into the tropics from the ASM complements the transport through the tropopause throughout the year.

This also suggests a connection between the ASM and the  $\delta D(H_2O)$  tape recorder, however, Randel et al. (2012) present a different behaviour of  $\delta D(H_2O)$  in the UTLS by analysing ACE-FTS satellite data. In these measurements, enriched  $\delta D(H_2O)$  at 16.5 km altitude can be found only over America and the patch of high  $\delta D(H_2O)$  associated with the ASM, as seen in the EMAC data is entirely lacking. This discrepancy between model and observations may be due to the underrepresentation of convective ice overshooting in the model's convection scheme.

Augmented convective ice lofting during the ASM season over the Himalaya mountains has been shown to isotopically enrich the water vapour in this region. Later on this enriched water vapour contributes significantly to the  $\delta D(H_2O)$  tape recorder in the EMAC simulation. Convective ice overshooting is under discussion as to whether having a significant effect on the stratospheric water vapour budget (see i.e. Khaykin et al., 2009). According to Dessler et al. (2007) and Bolot et al. (2013), however, it has a substantial effect on the  $\delta D(H_2O)$  signature in the UTLS. This ice overshooting effect performs mostly in the inner tropics and has the potential to isotopically enrich the tropical lower stratosphere. However, the NAM is also associated with strong convective ice overshooting (Uma et al., 2014). The direct intrusion of ice crystals into the stratosphere, though, is known to be represented rather sparsely by the here applied convection scheme from Tiedtke (1989). The outstanding high isotopic signature in ice over Asia may hence be an artefact of the underrepresented ice overshooting. The NAM region as well as the inner tropics may posses

comparably high  $\delta D(H_2O)$  values in the UTLS in ice. The estimate of the effect of the ASM region on stratospheric  $\delta D(H_2O)$  may hence be distorted. Moreover, this is most likely also the cause for the too low  $\delta D(H_2O)$  values in the lower tropical stratosphere in EMAC compared to satellite observations during NH summer.

# Chapter 6

## Conclusions and Outlook

### 6.1 Summary

Water vapour is the most important greenhouse gas. Variations of stratospheric water vapour alter the radiative heat budget (Forster and Shine, 1999) and the ozone mixing ratios (Shindell, 2001) in the stratosphere. The reasons for the recent trends and variations in stratospheric water vapour, however, are not well understood (IPCC, 2007). In order to study and quantify the processes determining the intrusion of water vapour into the stratosphere, water isotopologues have been included into the global climate chemistry model EMAC. For this, the new MESSy submodel H2OISO was developed, which contains an additional hydrological cycle including the water isotopologues HDO and H<sub>2</sub><sup>18</sup>O, and an accounting for the effect of methane oxidation on the budget of HDO.

As preparatory work for the implementation of the water isotopologues, the generic submodel TENDENCY was developed for accessing process-based tendencies of state variables (including tracers) in a well structured manner, with minimum memory requirements and maximum flexibility. Implemented in the EMAC model, this allows diagnosis and usage of these process tendencies and thus simplifies the analyses of mechanisms, as well as the computation of dependent processes.

The implementation allows a record of all the process - variable tendency pairs to be kept directly and to output and transfer tailor-made subsets for diagnostics and further analyses. This generalised approach is less error-prone and more user-friendly, because no recoding is required to set up specific tendency diagnostics. New submodels can easily be equipped with the TENDENCY feature by following a simple recipe and it is also applicable to other basemodels.

With a computing time overhead, due to the additional subroutine calls, of less than 2% on average, for a setup without atmospheric chemistry of the EMAC model a computationally light implementation of the additional tool was achieved. Exemplary results from a three year model simulation show the individual process tendencies of water vapour in the stratosphere. The chemical and the advection tendencies are identified, to control the dissipation of the tropical tape recorder.

With the assistance of the TENDENCY submodel, the separate hydrological cycle of the H2OISO submodel was tested to be correct. The occurring small numerical errors are corrected at the end of each time step, to guarantee equality between the two hydrological cycles and thus to prevent them from diverging. The analysis of the numerical errors assured, that these errors are irrelevant for the results of the water isotopologues.

While the structural implementation of the H2OISO submodel within the EMAC model follows the MESSy recipe and therewith a modular approach, the physical representation of the isotopologues was oriented on previous studies. Pioneering work from Joussaume et al. (1984) was, under constant development, integrated into several ECHAM versions, e.g. by Hoffmann et al. (1998, 2000) and Werner et al. (2001) and included into ECHAM5 by Werner et al. (2011). This well established code could largely be adopted for the physical part of the H2OISO submodel in EMAC.

The results of the EMAC simulations were first assessed with respect to the isotopic ratios in precipitation, in order to ensure the correct representation of the physical processes in the troposphere. Good agreement was achieved between the results of two different model simulations and data from the GNIP measurement survey (IAEA, 2009). In addition to that, the simulations were successfully compared with results from the ECHAM5-wiso model by Werner et al. (2011). Deficits in the reproduction of certain observations by the model can be associated with specific issues in the model system and were mostly already revealed in other studies. The modular manner of the H2OISO submodel, following the MESSy coding requirements, also provides the opportunity to extend the system to additional optional processes like a variety of convection schemes. Moreover, the applicability to other basemodels, global or regional, is given.

Based on the MESSy submodels CH4 and JVAL, a parameterisation of the oxidation of CH<sub>3</sub>D was included to the H2OISO submodel. The sink reactions of CH<sub>3</sub>D, which include reaction- and partly temperature-dependent kinetic fractionation effects, take the production of HDO into account. For the HDO budget, this is mainly important in the stratosphere, and hence also relevant for stratospheric  $\delta D(H_2O)$ .

Below 500 hPa, the CH<sub>3</sub>D tracer was kept at a fixed relation to CH<sub>4</sub>, since its exact determination for the various sources goes beyond the scope of this study. The climatological  $\delta D(CH_4)$  value of  $-68\text{‰}$  from Ridal and Siskind (2002) was prescribed for this purpose. The evaluation of the methane isotope ratio  $\delta D(CH_4)$  in the stratosphere, nevertheless, shows a good qualitative agreement with the chemically elaborate transport models by Ridal et al. (2001) and Ridal and Siskind (2002), as well as with radiosonde flights from Röckmann et al. (2011). As desired by Röckmann et al. (2011), it can assist for further studies, especially concerning the investigation of the chemical sink reactions of methane isotopologues in the stratosphere. Quantitative differences can merely be speculated about. Differences in the model dynamics as well as in the fractionation coefficients can play a role in the model-model intercomparison. The climatological value for stratospheric entry values of  $\delta D(CH_4)$ , the possible drift of the balloon and associated local meteorological features and especially the sparsity of the measurements, are the main issues in the comparison of  $\delta D(CH_4)$  in EMAC with observations. Anyhow, more extensive measurements are desired for further evaluation of the methane isotope ratios in the stratosphere.

The comparison of stratospheric HDO profiles with satellite observations reveals good qualitative agreement, as well. Inconsistencies between the individual satellite retrievals (see Lossow et al., 2011) make it delicate to define a distinct result. Different cloud filtering approaches and measurement techniques in the individual retrievals lead to these differences (see Lossow et al., 2011). Nevertheless, the UTLS appears to be too dry in HDO in the EMAC model compared to the ACE-FTS and the MIPAS satellite profiles. A possible explanation for this is the lack of the representation of ice overshooting convection in the here applied convection scheme (Tiedtke-Nordeng, Tiedtke, 1989). According to Dessler et al. (2007), a more complete representation of this effect can enhance the mixing ratios of HDO, while  $\text{H}_2\text{O}$  is not significantly affected. The rather low vertical resolution of the satellite observations on the other hand, are thought to blur the hygropause. Hence the HDO mixing ratios at the tropopause can be overestimated (see e.g., Steinwagner et al., 2007). Between 30 and 35 km the simulated HDO increases stronger with altitude than the satellite observations show. This is most likely to be a chemical effect, since it is obvious during all the four months where observations of ACE-FTS are available. It is probably linked to the fractionation factors in the sink reaction of  $\text{CH}_3\text{D}$ , because also  $\delta\text{D}(\text{CH}_4)$  is overestimated at these altitudes, especially in the tropical and mid-latitude profiles. A revision of the applied kinetic fractionation parameters and their temperature dependence, which were taken from Röckmann et al. (2011), is necessary to analyse this offset. The HDO mixing ratios above 40 km are underestimated by the EMAC model. This is attributable to the lack of the intermediate reactions containing HD in the  $\text{CH}_3\text{D}$  oxidation chain in the model, which include isotope effects. As has been shown by Röckmann et al. (2003), stratospheric  $\delta\text{D}(\text{H}_2)$  increases with altitude, while the mixing ratio of molecular hydrogen is rather constant. Additionally, the influence of the oxidation of  $\text{CH}_3\text{D}$  itself also increases with altitude. This implies that the here not implemented effect of the intermediate reaction with HD on HDO, increases with altitude, too. That simplification can therefore explain the offset in HDO mixing ratios between the EMAC simulation and the satellite retrievals above 40 km.

In future studies, the chemical deficiencies of the H2OISO submodel can be reduced, by including a representation of HD to take into account the intermediate reactions from  $\text{CH}_3\text{D}$  to  $\text{H}_2\text{O}$ . However, according to Zahn et al. (2006) the reaction rates of HD and especially the fractionation effects of these reactions are poorly quantified and hence can be subject of large uncertainties. As an alternative, however more sophisticated modelling approach, the water isotopologues can be included to the isotope scheme by Gromov et al. (2010), which features a number of isotopic species and reactions, which also affect the hydrogen reactions. Furthermore, the usage of other convection schemes may generate more suitable results of HDO in the UTLS. This, however, requires the implementation of the water isotopologues into the alternative convection schemes.

The comparison of the stratospheric tape recorder signal in  $\text{H}_2\text{O}$ , HDO and  $\delta\text{D}(\text{H}_2\text{O})$  between EMAC and satellite observations is difficult. In the lower stratosphere, EMAC and MIPAS (see Steinwagner et al., 2007, 2010) are closest during winter, where the differences can mostly be explained with the low vertical resolution of the MIPAS observations. The summer months, however, show much stronger deviations between model and observations, with too low values in all quantities in the simulation. This suggests deficiencies in the

model physics, most likely the underrepresentation of overshooting convection. Furthermore, a hardly explainable phase shift and, especially in  $\delta D(H_2O)$ , inconsistent amplitudes and vertical propagations between the tape recorder signals are observed. According to S. Lossow (personal communication, 2014), however, the inconsistent vertical resolutions between  $H_2O$  and  $HDO$  in the MIPAS retrieval can be the reason of an amplification of the  $\delta D(H_2O)$  tape recorder signal in the retrieval. The correction of this artefact in the MIPAS data is subject of current analyses.

The seasonal cycle of lower stratospheric  $\delta D(H_2O)$  in the ACE-FTS retrieval (see Randel et al., 2012) shows a different behaviour than that of the MIPAS retrieval and the EMAC simulation. The too low  $HDO$  mixing ratios in EMAC compared to ACE-FTS, especially during summer, are consistent, however, Randel et al. (2012) can not find the tape recorder signal in  $\delta D(H_2O)$ . The  $\delta D(H_2O)$  tape recorder signal in EMAC is weaker than the corresponding signals in  $H_2O$  and  $HDO$ . This is due to an overshadowing effect from high  $\delta D(H_2O)$  values in the upper parts of the stratosphere, evoked by different lifetimes of  $H_2O$  and  $HDO$ . Still the pattern is clearly recognisable in the lower stratosphere. A possible reason for the lack of the upward propagation of the seasonal cycle of  $\delta D(H_2O)$  in the ACE-FTS retrieval is the sparse temporal resolution of the instrument. In the tropics ACE-FTS measures only during four months per year. A corresponding filtering of the EMAC data reduces the apparent temporal upward motion of the  $\delta D(H_2O)$  tape recorder in the lower stratosphere and the signal fades out at even lower altitudes. In fact, this filtering makes the  $\delta D(H_2O)$  tape recorder hardly recognisable and therewith more similar to the ACE-FTS retrieval.

However, extended analyses have to be conducted to achieve a comprehensive and conclusive picture. In order to constitute more quantitative comparisons between models and observations, more sophisticated methods have to be applied in future evaluations. The model results can be made congruent in time and space to the satellite results by sampling them at the locations of the satellite overpasses. The MESSy submodel SORBIT (see Jöckel et al., 2010) provides this opportunity for arbitrary sun-synchronous satellite orbits. Moreover, the vertical resolution of the EMAC data can be transformed to the resolution of the respective satellite retrieval using their averaging kernel. Also, the cloud filtering methods used for the satellite data can be applied onto the model data. This elaborate evaluation can possibly assist to reduce the discrepancies between model results and observations. Hence it can reveal the model's and the measurement's insufficiencies more precisely and contribute to an improved understanding of the  $\delta D(H_2O)$  tape recorder.

As a first application of the new H2OISO submodel within the EMAC model, stratospheric water vapour isotope ratios were investigated. The time series of water vapour in the here applied EMAC simulation reproduces the major variations of the previous decades. This is assured by comparison with a combined MIPAS and HALOE satellite data set (S. Lossow, personal communication, 2014) and can also be seen when comparing it e.g., with the combined HALOE and MLS data set shown by Randel and Jensen (2013). The changes in stratospheric  $\delta D(H_2O)$  reveal connections to the water vapour variations, however, show different behaviour concerning the amplitude of certain changes. This suggests, that the processes controlling the two quantities are similar, although, influence them with different strengths.



In order to gain an understanding of the processes controlling stratospheric  $\delta D(H_2O)$ , at first, the impact of methane oxidation on the  $\delta D(H_2O)$  tape recorder signal was investigated. A sensitivity study evaluating the influence of a modified  $CH_3D$  oxidation, which does not affect  $\delta D(H_2O)$ , revealed that the isotope effects of methane oxidation blur the  $\delta D(H_2O)$  tape recorder signal, by damping its amplitude and overshadowing it at higher altitudes. These results are in agreement with a study by Randel et al. (2012), who introduced a methane correction to an ACE-FTS retrieval and contribute to a better understanding of the influence of methane oxidation on stratospheric  $\delta D(H_2O)$ .

The origin of enhanced  $\delta D(H_2O)$  in the lower stratosphere during NH summer in the EMAC model simulation was traced back to the Asian Summer Monsoon (ASM). The isotopic enrichment of water vapour in this region is associated with strong convective ice lofting over the Tibetan Plateau into the upper troposphere and further transport into the tropical stratosphere. On the one hand, this is consistent with studies, e.g. by Dethof et al. (1999); Bannister et al. (2004); Gettelman and Kinnison (2004); Lelieveld et al. (2007) and James et al. (2008), who also find the ASM to be a major driver for stratospheric water vapour mixing ratios during summer. On the other hand, the analysis of ACE-FTS measurements by Randel et al. (2012) suggest the North American Monsoon (NAM) to be the major source for isotopically enriched water vapour in the upper troposphere during JJA. No enhanced isotope ratios at these altitudes are connected with the ASM in this study.

For now, the reason for this discrepancy is open for speculation. A possible explanation is again the lack of the representation of ice overshooting convection in the here applied convection scheme. The NAM is associated with strong ice overshooting convection (Uma et al., 2014). The underrepresentation of this process in EMAC can be the reason for the too low  $\delta D(H_2O)$  values in the UTLS over North America and the inner tropics. The  $\delta D(H_2O)$  signal of the ASM would then not be as outstanding as it appears in the present simulation, its signature would rather be of similar or even lower strength compared to the other convective systems. At the same time, this would reduce the model's underrepresentation of  $\delta D(H_2O)$  in the lower stratosphere during summer. A trajectory model study by Dessler et al. (2007), which shows strong impact of convective overshooting on the isotopic composition of water vapour in the TTL supports this assumption. Evaluation of this effect could be conducted through the implementation and application of water isotopologues in other convection schemes of EMAC. Future sensitivity studies can then also resolve the robustness of the here discovered patterns and possibly explain the differences between model results and observations.

## 6.2 Conclusions

For the sake of the advancement of knowledge about the stratospheric water vapour budget, this study provides an extensive approach to the simulation of water isotopologues in a chemistry climate model and its evaluation and analysis in the stratosphere. The results, achieved with the new developments for the EMAC model system, now allow to answer the questions, which lead to this study.

- *What processes control the water vapour tape recorder in the stratosphere?*

The development of the TENDENCY submodel for EMAC enables process-based analyses of the tendencies of state variables. This has been applied to study the tropical water vapour tape recorder in the stratosphere. The investigation showed, that the chemical and the advection tendencies control the dissipation of the tropical tape recorder signal with height over time.

- *Are the observed patterns of the deuterium water vapour isotope composition in the stratosphere reproducible with a global climate chemistry model and can the reasons for the discrepancies between the observations be solved?*

A prerequisite for answering this question was the correct representation of the water isotopologues in the troposphere. The good agreement of the EMAC simulations with GNIP data and the almost identical results between EMAC and ECHAM5-wiso lead to the conclusion, that the physical processes and fractionation effects of the water isotopologues in the hydrological cycle of EMAC are represented satisfactorily. Hence the H2OISO submodel within the EMAC model represents the state of the art of water isotopologue-enabled GCMs.

Moreover, the chemical HDO precursor  $\text{CH}_3\text{D}$  was developed and evaluated for this purpose. This rather simple parameterisation of the methane isotopologue showed good results in a comparison with other models and in situ observations in the stratosphere and can be applied for further investigations.

The simulated HDO mixing ratios in the stratosphere agree qualitatively well with satellite observations. Discrepancies in the tropical tropopause layer revealed difficulties of the model physics to correctly represent the determining processes. Moreover, the lack of chemical isotope effects, concerning molecular hydrogen, was found to become important above 40 km altitude

Considering all the difficulties in the measurements and in the model, the overall representations of the tape recorder signals in EMAC are reasonable. The  $\delta\text{D}(\text{H}_2\text{O})$  tape recorder simulated by EMAC at least partly resolves the discrepancies between the divergent conclusions from the two satellite observations. The EMAC  $\delta\text{D}(\text{H}_2\text{O})$  tape recorder ranges between the pronounced tape recorder from MIPAS and the missing upward propagation of the seasonal signal in ACE-FTS observations. Specific deficits of the satellite retrievals and the model are responsible for the inconsistent results. The revision of the individual insufficiencies of the retrievals, however, are expected to alter the observations towards the EMAC results. It has been found, that the sparse temporal resolution of the ACE-FTS measurements has a considerable effect on the  $\delta\text{D}(\text{H}_2\text{O})$  tape recorder signal.

- *To what extent are the individual physical and chemical processes contributing to the patterns of the isotope composition of stratospheric water vapour?*

The analysis showed, that the fractionation effects caused by methane oxidation dampens and blurs the stratospheric  $\delta D(H_2O)$  tape recorder signal. Stratospheric isotope chemistry is therefore the reason for the less pronounced tape recorder signal in  $\delta D(H_2O)$ , compared to the signals in  $H_2O$  and  $HDO$ .

The Asian Summer Monsoon could be identified, to be the main contributor to the isotopically enriched water vapour in the lower stratosphere during boreal summer in the EMAC model. Since EMAC underestimates  $\delta D(H_2O)$  here, this suggests, that the effect of overshooting convection, especially in the North American Monsoon region and in the inner tropics, plays an important role for the patterns of  $\delta D(H_2O)$  in the stratosphere.

- *How can the simulated water isotope ratios serve for further investigations of the trends and variations in the stratospheric water vapour budget??*

Despite the quantitative differences in stratospheric  $HDO$  and  $\delta D(H_2O)$  between EMAC and satellite observations, the conclusion can be drawn, that the new MESSy submodel  $H_2OISO$ , used in the framework of the EMAC model, provides the possibility to attain additional insights into the mechanisms, which control the stratospheric water vapour budget. The physical and chemical properties of the isotopologue  $HDO$  in relation to 'normal' water, allow new investigation measures, with respect to the isotopic fingerprint, which specific processes leave in the water vapour content. The  $H_2OISO$  submodel will be available in future EMAC versions as an additional option for all users.

This study has set the basis for further analyses in order to determine the connection between the variations and trends in stratospheric  $\delta D(H_2O)$  and  $H_2O$ . This can be used to investigate specific changes of the stratospheric water vapour mixing ratios. The year 2001, for example, which exhibits a large drop in water vapour, can be examined in depth, using water isotopologues. Not only the decreasing tropopause temperature during that time may play a crucial role for this abrupt change. Also a change in the strength of the Monsoon systems, the patterns of convection or methane oxidation, or also a superposition of several of these effects can alter the stratospheric water vapour budget vastly. The additional information provided by the water isotope ratio can be of significant support to unravel the factors, which contribute to this and also to other abrupt and slow trends and variations in the stratospheric water vapour budget.

Further investigations of the UTLS, using water isotopologues, can hence be used to evaluate and revise the representation of the hydrological cycle in climate models. Subsequently, this will improve our understanding of the water vapour feedback to radiative forcing and to ozone chemistry. Therefore, a better quantification of the processes controlling the stratospheric water vapour budget, through the here implemented and analysed isotopologues, will, in the future, contribute to more reliable climate projections.



# Bibliography

- Ambach, W., Dansgaard, W., Eisner, H., and Møller, J. (1968). The altitude effect on the isotopic composition of precipitation and glacier ice in the Alps. *Tellus*, 4:595–600.
- Bannister, R. N., O'Neill, A., Gregory, A. R., and Nissen, K. M. (2004). The role of the south-east Asian monsoon and other seasonal features in creating the 'tape-recorder' signal in the Unified Model. *Quarterly Journal of the Royal Meteorological Society*, 130:1531–1554.
- Bates, D. R. and Nicolet, M. (1950). The photochemistry of atmospheric water vapor. *Journal of Geophysical Research*, 55(3):301–327.
- Bolot, M., Legras, B., and Moyer, E. (2013). Modelling and interpreting the isotopic composition of water vapour in convective updrafts. *Atmospheric Chemistry and Physics*, 13:7903–7935.
- Bradley, R. (1999). *Paleoclimatology*. Academic Press, Harcourt Brace and Company, San Diego, California.
- Brass, M. and Röckmann, T. (2010). Continuous-flow isotope ratio mass spectrometry method for carbon and hydrogen isotope measurements on atmospheric methane. *Atmospheric Measurement Techniques*, 3:1707–1721.
- Brewer, A. W. (1949). Evidence for a world circulation provided by the measurements of helium and water vapour distribution in the stratosphere. *Quarterly Journal of the Royal Meteorological Society*, 75:351–363.
- Brutsaert, W. (1975a). The roughness length for water vapor, sensible heat and other scalars. *Journal of Atmospheric Sciences*, 32:2028–2031.
- Brutsaert, W. (1975b). Theory for local evaporation (or heat transfer) from rough and smooth surfaces at ground level. *Water Resources Research*, 11:543–550.
- Chaboureaud, J.-P., Cammas, J.-P., Duron, J., Mascart, P. J., Sitnikov, N. M., and Voessing, H.-J. (2007). A numerical study of tropical cross-tropopause transport by convective overshoots. *Atmospheric Chemistry and Physics*, 7:1731–1740.
- Charney, J. G. and Drazin, P. G. (1961). Propagation of Planetary-Scale Disturbances from the Lower into the Upper Atmosphere. *Journal of Geophysical Research*, 66/1:83–109.
- Clough, S. A. and Iacono, M. J. (1995). Line-by-Line calculation of atmospheric fluxes and cooling rates: 2. Application to carbon dioxide, ozone, methane, nitrous oxide and the halocarbons. *Journal of Geophysical Research*, 100:519–535.
- Clough, S. A., Iacono, M. J., and Moncet, J.-L. (1992). Line-by-Line Calculations of Atmo-

- spheric Fluxes and Cooling Rates: Application to Water Vapor. *Journal of Geophysical Research*, 97/D14:761–785.
- Coffey, M. T., Hannigan, J. W., and Goldman, A. (2006). Observations of upper tropospheric/lower stratospheric water vapor and its isotopes. *Journal of Geophysical Research*, 111:D14313.
- Corti, T., Luo, B. P., de Reus, M., Brunner, D., Cairo, F., Mahoney, M. J., Martucci, G., Matthey, R., Mitev, V., dos Santos, F. H., Schiller, C., Shur, G., Sitnikov, N. M., Spelten, N., Vossing, H. J., Borrmann, S., and Peter, T. (2008). Unprecedented evidence for overshooting convection hydrating the tropical stratosphere. *Geophysical Research Letters*, 35:L10810.
- Craig, H. and Gordon, L. I. (1965). *Stable Isotopes in Oceanographic Studies and Paleotemperatures*, chapter Deuterium and oxygen 18 variations in the ocean and the marine atmosphere, pages 9–130. V. Lischi, Pisa, Italy.
- Danielsen, E. F. (1982). A dehydration mechanism for the stratosphere. *Geophysical Research Letters*, 9:605–608.
- Dansgaard, W. (1964). Stable isotopes in precipitation. *Tellus*, 16:436–468.
- Dee, D. P., Uppala, S. M., Simmons, A. J., Berrisford, P., Poli, P., Kobayashi, S., Andrae, U., M. A. Balmaseda, M. A., Balsamo, G., Bauer, P., Bechtold, P., Beljaars, A. C. M., van de Berg, L., Bidlot, J., Bormann, N. B., Delsol, C., Dragani, R., Fuentes, M., Geer, A. J., Haimberger, L., Healy, S. B., Hersbach, H., Hólm, E. V., Isaksen, I., Kållberg, P., Köhler, M., Matricardi, M., McNally, A. P., Monge-Sanz, B. M., Morcrette, J.-J., Park, B.-K., Peubey, C., de Rosnay, P., Tavolato, C., Thépaut, J.-N., and Vitart, F. (2011). The ERA-Interim reanalysis: configuration and performance of the data assimilation system. *Quarterly Journal of the Royal Meteorological Society*, 656:553–597.
- Dessler, A. E., Hanisco, T. F., and Füglistaler, S. (2007). Effects of convective ice lofting on H<sub>2</sub>O and HDO in the tropical tropopause layer. *Journal of Geophysical Research - Atmospheres*, 112(D18).
- Dessler, A. E., Schoeberl, M. R., Wang, T., Davis, S. M., and Rosenlof, K. H. (2013). Stratospheric water vapor feedback. *PNAS*, 110:18087–18091.
- Dessler, A. E. and Sherwood, S. C. (2003). A model of HDO in the tropical tropopause layer. *Atmospheric Chemistry and Physics*, 3:4489–4513.
- Dethof, A., O'Neill, A., Slingo, J. M., and Smit, H. G. J. (1999). A mechanism for moistening the lower stratosphere involving the Asian summer monsoon. *Quarterly Journal of the Royal Meteorological Society*, 125:1079–1106.
- Dewalle, D. and Swistock, B. (1994). Differences in oxygen-18 content of throughfall and rainfall in hardwood and coniferous forests. *Hydrological Proceedings of the Royal Society of Medicine*, 8:75–82.
- Dobson, G., Brewer, A., and Cwilog, B. (1946). Meteorology of the lower stratosphere. *Proceedings of the Royal Society of Medicine*, Ser. A, 185:144–175.
- Durry, G., Amarouche, N., Joly, I., Liu, X., Parvitte, B., and Zninari, V. (2008). Laser diode spectroscopy of H<sub>2</sub>O at 2.63  $\mu$ m for atmospheric applications. *Applied Physics B, Lasers and Optics*, 90:573–580.

- Dvortsov, V. L. and Solomon, S. (2001). Response of the stratospheric temperatures and ozone to past and future increases in stratospheric humidity. *Journal of Geophysical Research*, 106/D7:7505–7514.
- Forster, P. M. d. F. and Shine, K. P. (1999). Stratospheric water vapour changes as a possible contributor to observed stratospheric cooling. *Journal of Geophysical Research*, 26(21):3309–3312.
- Forster, P. M. d. F. and Shine, K. P. (2002). Assessing the climate impact of trends in stratospheric water vapour. *Geophysical Research Letters*, 29:6/1086.
- Friedmann, I. and Smith, G. (1970). Deuterium content of snow cores from Sierra Nevada area. *Science*, 169:467–470.
- Fritz, P., Cherry, J., Weyer, K., and Sklash, M. (1976). Storm runoff analysis using environmental isotopes and major ions. In *Interpretation of Environmental Isotopes and Hydrochemical Data in Groundwater Hydrology*. Vienna: International Atomic Energy Agency.
- Fritz, P. and Fontes, J. (1980). *Handbook of environmental isotope geochemistry*. Elsevier Scientific Pub. Co.
- Füglister, S., Dessler, A. E., Dunkerton, J. T., Folkins, I., Fu, Q., and Mote, P. W. (2009). Tropical Tropopause Layer. *Reviews of Geophysics*, 47:RG1004.
- Füglister, S., Wernli, H., and Peter, T. (2004). Tropical troposphere-to-stratosphere transport inferred from trajectory calculations. *Journal of Geophysical Research*, 109:D03108.
- Gat, J. (1996). Oxygen and hydrogen isotopes in the hydrological cycle. *Annual Review of Earth and Planetary Sciences*, 24:225–262.
- Gettelman, A. and Kinnison, D. E. (2004). Impact of monsoon circulations on the upper troposphere and lower stratosphere. *Journal of Geophysical Research*, 109:D22101.
- Gettelman, A., Randel, W. J., Wu, F., and Massie, S. T. (2002a). Transport of water vapor in the tropical tropopause layer. *Geophysical Research Letters*, 29(1):1009.
- Gettelman, A., Salby, M. L., and Sassi, F. (2002b). The distribution and influence of convection in the tropical tropopause region. *Journal of Geophysical Research*, 107:4080.
- Gromov, S., Jöckel, P., Sander, R., and Brenninkmeijer, C. A. M. (2010). A kinetic chemistry tagging technique and its application to modelling the stable isotopic composition of atmospheric trace gases. *Geoscientific Model Development*, 3:337–364.
- Grosvenor, D. P., Choularton, T. W., Coe, H., and Held, G. (2007). A study of the effect of overshooting deep convection on the water content of the TTL and lower stratosphere from Cloud Resolving Model simulations. *Atmospheric Chemistry and Physics*, 7:4977–5002.
- Hagemann, R., Nief, G., and Roth, E. (1970). Absolute isotopic scale for deuterium analysis of natural waters. Absolute D/H ratio for SMOW. *Tellus*, 22:712–715.
- Hagemann, S., Arpe, K., and Roeckner, E. (2005). Evaluation of the Hydrological Cycle in the ECHAM5 Model. *Journal of Climate*, 19:3810–3827.
- Hanisco, T. F., Moyer, E. J., Weinstock, E. M., St Clair, J. M., Sayres, D. S., Smith, J. B., Lockwood, R., Anderson, J. G., Dessler, A. E., Keutsch, F. N., Spackman, J. R., Read,

- W. G., and Bui, T. P. (2007). Observations of deep convective influence on stratospheric water vapor and its isotopic composition. *Geophysical Research Letters*, 34:L04814.
- Haynes, P. and McIntyre, M. (1987). On the Evolution of Vorticity and Potential Vorticity in the Presence of Diabatic Heating and Frictional or Other Forces. *Journal of the Atmospheric Sciences*, 44:828–841.
- Haynes, P. H., Marks, C. J., McIntyre, M. E., Shepherd, T. G., and Shine, K. P. (1991). On the "Downward Control" of Extratropical Diabatic Circulations by Eddy-Induced Mean Zonal Forces. *Journal of the Atmospheric Sciences*, 48:651–679.
- Hoffmann, G. (1995). *Stabile Wasserisotope im allgemeinen Zirkulationsmodell ECHAM*. PhD thesis, Universität Hamburg.
- Hoffmann, G., Jouzel, J., and Masson, V. (2000). Stable water isotopes in atmospheric general circulation models. *Hydrological Process*, 14:1385–1406.
- Hoffmann, G., Werner, M., and Heimann, M. (1998). Water isotope module of the ECHAM atmospheric general circulation model: A study on timescales from days to several years. *Journal of Geophysical Research*, 103:16,871–16,896.
- Holton, J. R. and Gettelman, A. (2001). Horizontal transport and the dehydration of the stratosphere. *Geophysical Research Letters*, 28/14:2799–2802.
- Holton, J. R., Haynes, P. H., McIntyre, M. E., Douglass, A. R., Rood, R. B., and Pfister, L. (1995). Stratosphere-Troposphere Exchange. *Reviews of Geophysics*, 33,4:403–439.
- Hoskins, B. J., McIntyre, M. E., and Robertson, A. W. (1985). On the use and significance of isentropic potential vorticity maps. *Quarterly Journal of the Royal Meteorological Society*, 111:847–946.
- Hurrell, J. W., Hack, J. J., Shea, D., Caron, J. M., and Rosinski, J. (2008). A New Sea Surface Temperature and Sea Ice Boundary Dataset for the Community Atmosphere Model. *Journal of Climate*, 21:5145–5153.
- Hurst, D. F., Oltmans, S. J., Vömel, H., Rosenlof, K. H., Davis, S. M., Ray, E. A., Hall, E. G., and Jordan, A. F. (2011). Stratospheric water vapor trends over Boulder, Colorado: Analysis of the 30 year Boulder record. *Journal of Geophysical Research*, 116:D02306.
- IAEA (1992). Statistical Treatment of Data on Environmental Isotopes in Precipitation, Series No. 331. Technical report, International Atomic Energy Agency, Vienna.
- IAEA (2001). GNIP Maps and Animations, International Atomic Energy Agency, Vienna; Available at <http://isohis.iaea.org>.
- IAEA (2009). Reference Sheet for VSMOW2 and SLAP2 international measurement standards. *International Atomic Energy Agency*, Vienna:p. 5, URL: [http://curem.iaea.org/catalogue/SI/pdf/VSMOW2\\_SLAP2.pdf](http://curem.iaea.org/catalogue/SI/pdf/VSMOW2_SLAP2.pdf).
- IPCC (2007). *The Physical Science Basis. Contribution of Working Group I to the Fourth Assessment Report of the Intergovernmental Panel on Climate Change*. Cambridge University Press, Cambridge, United Kingdom and New York, NY, USA.
- Irion, F. W., Moyer, E. J., Gunson, M. R., Rinsland, C. P., Yung, Y. L., Michelsen, H. A., Salawitch, R. J., Chang, A. Y., Newchurch, M. J., Abbas, M. M., Abrams, M. C., and Zander, R. (1996). Stratospheric observations of CH<sub>3</sub>D and HDO from ATMOS



- infrared solar spectra: Enrichments of deuterium in methane and implications for HD. *Geophysical Research Letters*, 23:2381–2384.
- James, R., Bonazzola, M., Legras, B., Surbled, K., and Fueglistaler, S. (2008). Water vapor transport and dehydration above convective outflow during Asian monsoon. *Geophysical Research Letters*, 35:L20810.
- Jensen, E. J., Ackerman, A. S., and Smith, J. A. (2007). Can overshooting convection dehydrate the tropical tropopause layer? *Journal of Geophysical Research*, 112:D11209.
- Jöckel, P., Kerkweg, A., Buchholz-Dietsch, J., Tost, H., Sander, R., and Pozzer, A. (2008). Technical Note: Coupling of chemical processes with the Modular Earth Submodel System (MESSy) submodel TRACER. *Atmospheric Chemistry and Physics*, 8:1677–1687.
- Jöckel, P., Kerkweg, A., Pozzer, A., Sander, R., Tost, H., Riede, H., Baumgärtner, A., Gromov, S., and Kern, B. (2010). Development cycle 2 of the Modular Earth Submodel System (MESSy2). *Geoscientific Model Development*, 3:1423–1501.
- Jöckel, P., Sander, R., Kerkweg, A., Tost, H., and Lelieveld, J. (2005). Technical Note: The Modular Earth Submodel System (MESSy), a new approach towards Earth System Modeling. *Atmospheric Chemistry and Physics*, 5:433–444.
- Johnson, D. G., Jucks, K. W., Traub, W. A., and Chance, K. V. (2001a). Isotopic composition of stratospheric water vapor: Implications for transport. *Journal of Geophysical Research*, 106:12219–12226.
- Johnson, D. G., Jucks, K. W., Traub, W. A., and Chance, K. V. (2001b). Isotopic composition of stratospheric water vapor: Measurements and photochemistry. *Journal of Geophysical Research*, 106:12211–12217.
- Joussaume, S., Sadourny, R., and Jouzel, J. (1984). A General Circulation Model of Water Isotope Cycles in the Atmosphere. *Nature*, 311(5981):24–29.
- Jouzel, J. and Merlivat, L. (1984). Deuterium and oxygen 18 in precipitation: Modeling of the isotopic effects during snow formation. *Journal of Geophysical Research*, 89:11749–11757.
- Jouzel, J., Russell, G., Suozzo, R., Koster, D., White, J., and Broecker, W. (1987). Simulations of the HDO and H<sub>2</sub><sup>18</sup>O atmospheric cycles using the NASA GISS general circulation model: The seasonal cycle for present-day conditions. *Journal of Geophysical Research*, 92:14739–14760.
- Kaye, J. A. (1987). Mechanisms and observations for isotope fractionation of molecular species in planetary atmospheres. *Reviews of Geophysics*, 25:1609–1658.
- Kerkweg, A. and Jöckel, P. (2012). The 1-way on-line coupled atmospheric chemistry model system MECO(n) - Part 1: Description of the limited-area atmospheric chemistry model COSMO/MESSy. *Geoscientific Model Development*, 5:87–110.
- Khaykin, S., Pommereau, J.-P., Korshunov, L., Yushkov, V., Nielsen, J., Larsen, N., Christensen, T., Garnier, A., Lukyanov, A., and Williams, E. (2009). Hydration of the lower stratosphere by ice crystal geysers over land convective systems. *Atmospheric Chemistry and Physics*, 9:2275–2287.
- Kuhn, W. and Thürkauf, M. (1958). Isotopentrennung beim Gefrieren von Wasser und

- Diffusionskonstanten von D und  $^{18}\text{O}$  im Eis. Mit Diskussion der Möglichkeit einer Multiplikation der beim Gefrieren auftretenden Isotopentrennung in einer Haarnadelgegenstromvorrichtung. *Helvetica Chimica Acta*, 41:938–971.
- Kurita, N., Sugimoto, A., Fujii, Y., Fukazawa, T., Makarov, V. N., Watanabe, O., Ichiyangi, K., Numaguti, A., and Yoshida, N. (2005). Isotopic composition and origin of snow over Siberia. *Journal of Geophysical Research*, 110:D13102.
- Landgraf, J. and Crutzen, P. J. (1998). An Efficient Method for Online Calculations of Photolysis and Heating Rates. *Journal of Atmospheric Sciences*, 55:863–878.
- Le Texier, H., Solomon, S., and Garcia, R. R. (1988). The role of molecular hydrogen and methane oxidation in the water vapour budget of the stratosphere. *Quarterly Journal of the Royal Meteorological Society*, 114:281–295.
- Lee, J.-E. and Fung, I. (2007). Amount effect of water isotopes and quantitative analysis of post-condensation processes. *Hydrological Processes*, 22:1–8.
- Lee, J.-E., Fung, I., DePaolo, D. J., and Henning, C. C. (2007). Analysis of the global distribution of water isotopes using the NCAR atmospheric general circulation model. *Journal of Geophysical Research*, 112:D16306.
- LeGrande, A. N. and Schmidt, G. A. (2006). Global gridded data set of the oxygen isotopic composition in seawater. *Geophysical Research Letters*, 33:L12604.
- Lelieveld, J., Brühl, C., Jöckel, P., Steil, B., Crutzen, J. P., Fischer, H., Giorgetta, M. A., Hoor, P., Lawrence, M. G., Sausen, R., and Tost, H. (2007). Stratospheric dryness: model simulations and satellite observations. *Atmospheric Chemistry and Physics*, 7:1313–1332.
- Lin, S. J. and Rood, R. B. (1996). Multidimensional flux form semi-lagrangian transport. *Monthly Weather Review*, 124:2046–2068.
- Lossow, S., Steinwagner, J., Urban, J., Dupuy, E., Boone, C. D., Kellmann, S., Linden, A., Kiefer, M., Grabowski, U., Glatthor, N., Höpfner, M., Röckmann, T., Murtagh, D. P., Walker, K. A., Bernath, P. F., von Clarmann, T., and Stiller, G. P. (2011). Comparison of HDO measurements from Envisat/MIPAS with observations by ODIN/SMR and SCISAT/ACE-FTS. *Atmospheric Measurement Techniques*, 4:1855–1874.
- Majoube, M. (1971a). Fractionnement en oxygène-18 entre la glace et la vapeur d'eau. *Journal de Chimie et de Physique*, 68:625–636.
- Majoube, M. (1971b). Fractionnement en oxygène-18 et en deutérium entre l'eau et sa vapeur. *Journal de Chimie et de Physique*, 68:1423–1436.
- Masson-Delmotte, V., S., H., Ekaykin, A., Jouzel, J., Aristarain, A., Bernardo, R. T., Bromwich, D., Cattani, O., M., D., Falourd, S., Frezzotti, M., Gallée, H., Genoni, L., Isaksson, E., Landais, A., Helsen, M. M., Hoffmann, G., Lopez, J., Morgan, V., Motoyama, H., Noone, D., Oerter, H., Petit, J. R., Royer, A., Uemura, R., Schmidt, G. A., Schlosser, E., Simões, J. C., Steig, E. J., Stenni, B., Stievenard, M., van den Broeke, M. R., van de Wal, R. S. W., van de Berg, W. J., Vimeux, I. F., and White, J. W. C. (2008). A review of antarctic surface snow isotopic composition: Observations, atmospheric circulation, and isotopic modeling. *Journal of Climate*, 21:3359–3387.
- Mathieu, R., Pollard, D., Cole, J. E., White, J. W. C., Webb, R. S., and Thompson, S. L. (2002). Simulation of stable water isotope variations by the GENESIS GCM for modern

- conditions. *Journal of Geophysical Research (Atmospheres)*, 107(D4):4037.
- Maycock, A. C., Joshi, M. M., Shine, K. P., and Scaife, A. A. (2013). The Circulation Response to Idealized Changes in Stratospheric Water Vapor. *Journal of Climate*, 26:545–561.
- Maycock, A. C. and Shine, K. P. (2012). Stratospheric water vapor and climate: Sensitivity to the representation in radiation codes. *Journal of Geophysical Research*, 117:D13102.
- Merlivat, L. (1978). Molecular diffusivities of  $\text{H}_2^{16}\text{O}$ ,  $\text{HD}^{16}\text{O}$ , and  $\text{H}_2^{18}\text{O}$  in gases. *Journal of Chemical Physics*, 69:2864–2871.
- Merlivat, L. and Jouzel, J. (1979). Global Climatic Interpretation of the Deuterium-Oxygen 18 Relationship for Precipitation. *Journal of Geophysical Research*, 84:5029–5033.
- Mook, W. G. (2000a). Environmental isotopes in the hydrological cycle: Principals and applications. In *Volume 1, Introduction: Theory, Methods, Review*. International Hydrological Programme.
- Mook, W. G. (2000b). Environmental isotopes in the hydrological cycle: Principals and applications. In *Volume 2, Atmospheric water*. International Hydrological Programme.
- Mordaunt, D. H., Lambert, I. R., Morley, G. P., Ashfold, M. N. R., Dixon, R. N., Western, C. M., Schnieder, L., and Welge, K. H. (1992). Primary product channels in the photodissociation of methane at 121.6 nm. *Journal of Chemical Physics*, 98:2054–2065.
- Mote, P., Rosenlof, K., Holton, J., Harwood, R., and Waters, J. (1995). Seasonal variations of water vapor in the tropical lower stratosphere. *Geophysical Research Letters*, 22:1093–1096.
- Mote, P., Rosenlof, K., McIntyre, M., Carr, E., Gille, J., Holton, J., Kinnersley, J., Pumphrey, H., Russel, J., and Waters, J. (1996). An atmospheric tape recorder: The imprint of tropical tropopause temperatures on stratospheric water vapor. *Journal of Geophysical Research*, 101:3989–4006.
- Mote, P. W., Dunkerton, T. J., McIntyre, M. E., Ray, E. A., Haynes, P. H., and Russell, J. M. (1998). Vertical velocity, vertical diffusion, and dilution by midlatitude air in the tropical lower stratosphere. *Journal of Geophysical Research*, 103/D8:8651–8666.
- Nair, H., Summers, M. E., Miller, C. E., and Yung, Y. L. (2005). Isotopic fractionation of methane in the martian atmosphere. *Icarus*, 175:32–35.
- Nassar, R., Bernath, P. F., Boone, C. D., Gettelman, A., McLeod, S. D., and Rinsland, C. P. (2007). Variability in  $\text{HDO}/\text{H}_2\text{O}$  abundance ratios in the tropical tropopause layer. *Journal of Geophysical Research*, 112:D21305.
- Newell, R. E. and Gould-Steward, S. (1981). A Stratospheric Fountain. *Journal of the Atmospheric Sciences*, 38:2789–2796.
- Nielsen, J. K., Larsen, N., Cairo, F., Di Donfrancesco, G., Rosen, J. M., Durr, G., Held, G., and Pommereau, J. P. (2007). Solid particles in the tropical lowest stratosphere. *Atmospheric Chemistry and Physics*, 7:685–695.
- Nier, A. O. (1947). A Mass Spectrometer for Isotope and Gas Analysis. *Review of Scientific Instruments*, 18:398–411.
- Niwano, M., Yamazaki, K., and Shiotani, M. (2003). Seasonal and QBO variations of ascent

- rate in the tropical lower stratosphere as inferred from UARS HALOE trace gas data. *Journal of Geophysical Research*, 108:D24, 4794.
- Nixon, C. A., Temelso, B., Vinatier, S., Teanby, N. A., Bézard, B., Achterberg, R. K., Mandt, K. E., Sherrill, C. D., Irwin, P. G. J., Jennings, D. E., Romani, P. N., Coustenis, A., and Flasar, F. M. (2012). Isotopic ratios in Titan's methane: Measurements and Modelling. *The Astrophysical Journal*, 759:159.
- Noone, D. (2006). Evaluation of hydrological cycles and processes with water isotopes: Report to GEWEX-GHP from the Stable Water-isotope Intercomparison Group (SWING). *Pan-GEWEX Meeting*, Frascati:Italy.
- Noone, D. and Simmonds, I. (2002). Associations between  $\delta^{18}\text{O}$  of water and climate parameters in a simulation of atmospheric circulation 1979-1995. *Journal of Climate*, 15:3150–3169.
- Noone, D. and Sturm, C. (2010). *Isoscapes: Understanding Movement, Patterns, and Process on EARTH through Isotope Mapping*, chapter Comprehensive dynamical models of global and regional water isotope distributions, pages 195–219. Springer.
- Notholt, J., Toon, G. C., Fueglistaler, S., Wennberg, P. O., Irion, F. W., McCarthy, M., Scharringhausen, M., Siek Rhee, T., Kleinböhl, A., and Velazco, V. (2010). Trend in ice moistening the stratosphere - constraints from isotope data of water and methane. *Atmospheric Chemistry and Physics*, 10:201–207.
- Oinas, V., Lacis, A., Rind, D., Shindell, D., and Hansen, J. (2001). Radiative cooling by stratospheric water vapor: Big differences in GCM results. *Geophysical Research Letters*, 28/14:2791–2794.
- Plumb, A. R. (2002). Stratospheric Transport. *Journal of the Meteorological Society of Japan*, 80:793–809.
- Plumb, R. A. and Ko, M. K. W. (2004). Interrelationships between mixing ratios of long lived stratospheric constituents. *Journal of Geophysical Research*, 101:3957–3972.
- Randel, W. J. and Jensen, E. J. (2013). Physical processes in the tropical tropopause layer and their roles in a changing climate. *Nature Geoscience*, 6:169–176.
- Randel, W. J., Moyer, E., Park, M., Jensen, E., Bernath, P., Walker, K., and Boone, C. (2012). Global variations of HDO and HDO/H<sub>2</sub>O ratios in the upper troposphere and lower stratosphere derived from ACE-FTS satellite measurements. *Journal of Geophysical research*, 117:D06303.
- Ravishankara, A. R. (1988). Kinetics of radical reactions in the atmospheric oxidation of CH<sub>4</sub>. *Annual Review of Physical Chemistry*, 39:367–394.
- Reid, G. C. and Gage, K. S. (1996). The tropical tropopause over the western Pacific: Wave driving, convection, and the annual cycle. *Journal of Geophysical Research*, 101:21,233–21,241.
- Rhee, T. S., Brenninkmeijer, C. A. M., Braß, M., and Brühl, C. (2006). Isotopic composition of H<sub>2</sub> from CH<sub>4</sub> oxidation in the stratosphere and the troposphere. *Journal of Geophysical Research*, 111:D23303.
- Ridal, M. (2002). Isotopic ratios of water vapor and methane in the stratosphere: Compari-

- son between ATMOS measurements and a one-dimensional model. *Journal of Geophysical Research*, 107:D16,4285.
- Ridal, M., Jonsson, A., Werner, M., and Murtagh, D. P. (2001). A one-dimensional simulation of the water vapor isotope HDO in the tropical stratosphere. *Journal of Geophysical Research*, 106:32283–32294.
- Ridal, M. and Siskind, D. E. (2002). A two-dimensional simulation of the isotopic composition of water vapor and methane in the upper atmosphere. *Journal of Geophysical Research*, 107:D24,4807.
- Risi, C., Bony, S., Vimeux, F., and Jouzel, J. (2010). Water-stable isotopes in the LMDZ4 general circulation model: Model evaluation for present-day and past climates and applications to climatic interpretations of tropical isotopic records. *Journal of Geophysical Research*, 115:D12118.
- Röckmann, T., Brass, M., Borchers, R., and Engel, A. (2011). The isotopic composition of methane in the stratosphere: high-altitude balloon sample measurements. *Atmospheric Chemistry and Physics*, 11:13287–13304.
- Röckmann, T., Rhee, T. S., and Engel, A. (2003). Heavy hydrogen in the stratosphere. *Atmospheric Chemistry and Physics*, 3:2015–2023.
- Roeckner, E., Bäuml, G., Bonaventura, L., Brokopf, R., Esch, M., Giorgetta, M., Hagemann, S., Kirchner, I., Kornblueh, L., Manzini, E., Rhodin, A., Schlese, U., Schulzweida, U., and Tompkins, A. (2003). The atmospheric general circulation model ECHAM 5. PART I: Model description. *Max-Planck-Institut für Meteorologie*, Hamburg:Report No. 349.
- Roeckner, E., Brokopf, R., Esch, M., Giorgetta, M., Hagemann, S., Kornblueh, L., Manzini, E., Schlese, U., and Schulzweida, U. (2006). Sensitivity of simulated climate to horizontal and vertical resolution in the ECHAM5 atmosphere model. *Journal of Climate*, 19(16):3771–3791.
- Rohs, S., Schiller, C., Riese, M., Engel, A., Schmidt, U., Wetter, T., Levin, I., Nakazawa, T., and Aoki, S. (2006). Long-term changes of methane and hydrogen in the stratosphere in the period 1978–2003 and their impact on the abundance of stratospheric water vapor. *Journal of Geophysical Research*, 111:D14315.
- Rosenlof, K. H., Oltmans, S. J., Kley, D., Russell, J. M., Chiou, E.-W., Chu, W. P., Johnson, D. G., Kelly, K. K., Michelsen, H. A., Nedoluha, G. E., Remsberg, E. E., Toon, G. C., and McCormick, M. P. (2001). Stratospheric water vapor increases over the past half-century. *Geophysical Research Letters*, 28/7:1195–1198.
- Rosenlof, K. H. and Reid, G. C. (2008). Trends in the temperature and water vapor content of the tropical lower stratosphere: Sea surface connection. *Journal of Geophysical Research*, 113:D06107.
- Rosenlof, K. H., Tuck, A. F., Kelly, K. K., Russell, J. M., and McCormick, M. P. (1997). Hemispheric asymmetries in water vapor and inferences about transport in the lower stratosphere. *Journal of Geophysical Research*, 102:13213–13234.
- Rozanski, K., Araguas-Araguas, L., and Giofanti, R. (1993). Isotopic patterns in modern global precipitation. *Geophysical Monograph*, 78:1–36.

- Russell, P. B., Pfister, L., and Selkirk, H. B. (1993). The tropical experiment of the Stratosphere-Troposphere Exchange Project (STEP): science objectives, operations, and summary findings. *Journal of Geophysical Research*, 98:8563–8589.
- Saueressig, G., Bergamaschi, P., Crowley, J., Fischer, H., and Harris, G. (1996). D/H kinetic isotope effects in the reaction  $\text{CH}_4 + \text{Cl}$ . *Geophysical Research Letters*, 23:3619–3622.
- Saueressig, G., Crowley, J., Bergamaschi, P., Brühl, C., Brenninkmeijer, C., and Fischer, H. (2001). Carbon 13 and D kinetic isotope effects in the reactions of  $\text{CH}_4$  with  $\text{O}(^1\text{D})$  and OH: New laboratory measurements and their implications for the isotopic composition of stratospheric methane. *Journal of Geophysical Research*, 106:23127–23138.
- Sayres, D. S., Pfister, L., Hanisco, T. F., Moyer, E. J., Smith, J. B., St Clair, J. M., O'Brian, A. S., Witinski, M. F., Legg, M., and Anderson, J. G. (2010). Influence of convection on the water isotopic composition of the tropical tropopause layer and tropical stratosphere. *Journal of Geophysical Research*, 115:D00J20.
- Schmidt, G. A., Hoffmann, G., Shindell, D. T., and Hu, Y. (2005). Modeling atmospheric stable water isotopes and the potential for constraining cloud processes and stratosphere-troposphere water exchange. *Journal of Geophysical Research*, 110:D21314.
- Schotterer, U., Oldfield, F., and Fröhlich, K. (1996). Global Network for Isotopes in Precipitation (GNIP) - Brochure. IAEA-WMO.
- Sherwood, S. A. and Dessler, A. E. (2000). On the control of stratospheric humidity. *Geophysical Research Letters*, 27:2513–2516.
- Shindell, D. T. (2001). Climate and ozone response to increased stratospheric water vapor. *Geophysical Research Letters*, 28/8:1551–1554.
- Sime, L. C., Tindall, J. C., Wolff, E. W., Conolley, W. M., and Valdes, P. J. (2008). Antarctic isotopic thermometer during a  $\text{CO}_2$  forced warming event. *Journal of Geophysical Research*, 113:D24119.
- Solomon, S., Garcia, R. R., Rowland, F. S., and Wuebbles, D. J. (1986). On the depletion of Antarctic ozone. *Nature*, 321:755–758.
- Solomon, S., Rosenlof, K. H., Portmann, R. W., Daniel, J. S., Davis, S. M., Sanford, T. J., and Plattner, G.-K. (2010). Contributions of Stratospheric Water Vapor to Decadal Changes in the Rate of Global Warming. *Science*, 327:1219–1223.
- Souchez, R., Jouzel, J., Lorrain, R., Sleewaegen, S., Stiévenard, M., and Verbeke, V. (2000). A kinetic isotope effect during ice formation by water freezing. *Geophysical Research Letters*, 27:1923–1926.
- Souchez, R. A. and Jouzel, J. (1984). On the isotopic composition in  $\delta\text{D}$  and  $\delta^{18}\text{O}$  of water and ice. *Journal of Glaciology*, 30:369–372.
- Steinwagner, J., Füglistaler, S., Stiller, G., von Clarmann, T., Kiefer, M., Borsboom, P.-P., van Delden, A., and Röckmann, T. (2010). Tropical dehydration processes constrained by the seasonality of stratospheric deuterated water. *Nature Geoscience*, 3(4):262–266.
- Steinwagner, J., Milz, M., von Clarmann, T., Glatthor, N., Grabowski, U., Höpfner, M., Stiller, G. P., and Röckmann, T. (2007). HDO measurements with MIPAS. *Atmospheric Chemistry and Physics*, 7:2601–2615.

- Stenke, A. (2005). *Stratosphärischer Wasserdampf in einem gekoppelten Klima-Chemie-Modell: Simulation, Trends und Bedeutung für die Ozonchemie*. PhD thesis, Ludwig-Maximilians-Universität München.
- Stenke, A. and Grewe, V. (2005). Simulation of stratospheric water vapor trends: impact on stratospheric ozone chemistry. *Atmospheric Chemistry and Physics*, 5:1257–1272.
- Stewart, M. K. (1975). Stable isotope fractionation due to evaporation and isotopic exchange of falling waterdrops: Applications to atmospheric processes and evaporation of lakes. *Journal of Geophysical Research*, 80:1133–1146.
- Tiedtke, M. (1989). A comprehensive mass flux scheme for cumulus parameterization in large-scale models. *Monthly Weather Review*, 117:1779–1800.
- Tindall, J. C., Valdes, P. J., and Sime, L. C. (2009). Stable water isotopes in HadCM3: Isotopic signature of El Niño Southern Oscillation and the tropical amount effect. *Journal of Geophysical Research*, 114:D04111.
- Uma, K. N., Das, S. K., and Das, S. S. (2014). A climatological perspective of water vapor at the UTLS region over different global monsoon regions: observations inferred from the Aura-MLS and reanalysis data. *Climate Dynamics*, 42:10.1007.
- Urban, J., Lautié, N., Murtagh, D., Eriksson, P., Kasai, Y., Lossow, S., Dupuy, E., de La Noë, J., Frisk, U., Olberg, M., Le Flochmoën, E., and Ricaud, P. (2007). Global observations of middle atmospheric water vapour by the Odin satellite: An overview. *Planetary and Space Science*, 55:1093–1102.
- Urey, H. C. (1948). Oxygen isotopes in nature and in the laboratory. *Science*, 108:489–496.
- Urey, H. C. and Teal, G. K. (1935). The Hydrogen Isotope of Atomic Weight Two. *Reviews of Modern Physics*, 7:34–94.
- Weinstock, E., Hintsä, E., Dessler, A., and Anderson, J. (1995). Measurements of water vapor in the tropical lower stratosphere during the CEPEX Campaign: Results and interpretation. *Geophysical Research Letters*, 22:3231–3234.
- Werner, M., Heimann, M., and Hoffmann, G. (2001). Isotopic composition and origin of polar precipitation in present and glacial climate simulations. *Tellus B*, 53B:53–71.
- Werner, M., Langebroek, P. M., Carlsen, T., Herold, M., and Lohmann, G. (2011). Stable water isotopes in the ECHAM5 general circulation model: Toward high-resolution isotope modeling on a global scale. *Journal of Geophysical Research*, 116:D15109.
- White, J. (1989). Stable hydrogen isotope ratios in plants: A review of current theory and some potential applications. In *Stable Isotopes in Ecological Research*. Springer, New York.
- WMO (2006). Scientific Assessment of Ozone Depletion. In *Global Ozone Research and Monitoring Project-Report No.50*. World Meteorological Organisation, Geneva, Switzerland.
- Yoshimura, K., Kanamitsu, M., Noone, D., and Oki, T. (2008). Historical isotope simulation using Reanalysis atmospheric data. *Journal of Geophysical Research*, 113:D19108.
- Zahn, A., Franz, P., Bechtel, C., Grooss, J., and Röckmann, T. (2006). Modelling the budget of middle atmospheric water vapour isotopes. *Atmospheric Chemistry and Physics*,

6:2073–2090.

Zellner, R. (1999). Topics in Physical Chemistry. In *Global Aspects of Atmospheric Chemistry, Vol. 6*. Steinkopff ISBN 3-7985-1127-6.

Zhong, W. and Haigh, J. D. (2003). Shortwave radiative forcing by stratospheric water vapor. *Geophysical Research Letters*, 30:1113.



# List of Figures

1.1	Schematic of the different pathways of water vapour through the tropics into the stratosphere, Steinwagner et al. (2010). . . . .	2
2.1	Vertical water vapour profile, Durry et al. (2008) . . . . .	8
2.2	Dynamical aspects of stratosphere-troposphere exchange, Holton et al. (1995). . . . .	9
2.3	Schematic of cloud processes and transport and of zonal mean circulation, Füglistaler et al. (2009). . . . .	10
2.4	Stratospheric water vapour mixing ratio from 1980 to 2010, Hurst et al. (2011). . . . .	12
2.5	Stratospheric tropical water vapour tape recorder from 1993 to 2005, Rosenlof and Reid (2008) . . . . .	13
2.6	Measured and modelled temperature changes relative to 1980, Solomon et al. (2010). . . . .	14
2.7	The water isotopologues $\text{H}_2^{16}\text{O}$ , $\text{H}_2^{18}\text{O}$ and $\text{HD}^{16}\text{O}$ , M. Werner (personal communication, 2013) . . . . .	16
2.8	Temperature dependency of the fractionation factors, Hoffmann (1995) . . . . .	18
2.9	The Rayleigh box model, Mook (2000b) . . . . .	21
2.10	Enrichment of an isotope by the Rayleigh process, Mook (2000a) . . . . .	22
2.11	Schematic overview of the hydrological cycle showing $\delta^{18}\text{O}(\text{H}_2\text{O})$ , Schotterer et al. (1996) . . . . .	26
3.1	Sketch of the four layers of MESSy (Kerkweg and Jöckel, 2012). . . . .	28
3.2	Operator splitting concept. . . . .	30
3.3	Schematic of the MESSy TENDENCY submodel within the framework of the EMAC model system. . . . .	31
3.4	Zonally averaged specific humidity and total tendency of the specific humidity from $5^\circ\text{S}$ - $5^\circ\text{N}$ . . . . .	38
3.5	Zonally averaged process tendencies of the specific humidity from $5^\circ\text{S}$ - $5^\circ\text{N}$ . . . . .	40
3.6	Temporally and zonally averaged process tendencies of the specific humidity at the equator. . . . .	41
3.7	Schematic overview of the two hydrological cycles, M. Werner (personal communication, 2013) . . . . .	44
4.1	Relative numerical error. . . . .	55

4.2	$\delta^{18}\text{O}(\text{H}_2\text{O})$ in precipitation. EMAC, GNIP and the absolute values of GNIP minus EMAC. . . . .	57
4.3	$\delta\text{D}(\text{H}_2\text{O})$ in precipitation. EMAC, GNIP and the absolute values of GNIP minus EMAC. . . . .	58
4.4	Comparison of the seasonal cycle of $\delta\text{D}(\text{H}_2\text{O})$ between GNIP and EMAC for selected regions. . . . .	60
4.5	Annual $\delta^{18}\text{O}(\text{H}_2\text{O})$ in precipitation, for the two EMAC simulations, globally and for Europe. . . . .	61
4.6	GNIP measurements and ECHAM5-wiso results of $\text{H}_2^{18}\text{O}$ in precipitation, Werner et al. (2011) . . . . .	62
4.7	Comparison of $\delta\text{D}(\text{H}_2\text{O})$ in precipitation between EMAC and ECHAM5-wiso in Antarctica. . . . .	63
4.8	Comparison of $\delta\text{D}(\text{CH}_4)$ with altitude between EMAC, CHEM2D, CHEM1D. . . . .	66
4.9	Comparison of $\delta\text{D}(\text{CH}_4)$ vertical profiles between the model simulation and balloon borne data. . . . .	67
4.10	Comparison of the relations of $\text{CH}_4$ to $\delta\text{D}(\text{CH}_4)$ between EMAC and balloon borne data. . . . .	69
4.11	Comparison of HDO altitude profiles between EMAC and various satellite observations. . . . .	71
4.12	Altitude-time diagrams of tropical $\text{H}_2\text{O}$ , HDO and $\delta\text{D}(\text{H}_2\text{O})$ in EMAC and MIPAS. . . . .	72
4.13	Altitude-time diagrams of the vertical profile of the anomaly of tropical $\text{H}_2\text{O}$ , HDO and $\delta\text{D}(\text{H}_2\text{O})$ in EMAC and MIPAS. . . . .	73
4.14	Altitude-time diagrams of $\text{H}_2\text{O}$ , HDO mixing ratios and $\delta\text{D}(\text{H}_2\text{O})$ in the tropics derived from ACE-FTS observations, Randel et al. (2012) . . . . .	75
4.15	Altitude-time diagrams of tropical $\text{H}_2\text{O}$ , HDO and $\delta\text{D}(\text{H}_2\text{O})$ in EMAC with the entire data set and with selected months. . . . .	76
4.16	Zonally averaged seasonal $\delta\text{D}(\text{CH}_4)$ . . . . .	78
5.1	Time series of stratospheric water vapour at the equator, HALOE/MIPAS and EMAC. . . . .	82
5.2	Time series of stratospheric water vapour and $\delta\text{D}(\text{H}_2\text{O})$ anomalies at 18 km and at 30 km altitude. . . . .	83
5.3	$\delta\text{D}(\text{H}_2\text{O})$ tape recorder with the effect of methane oxidation. . . . .	85
5.4	$\delta\text{D}(\text{H}_2\text{O})$ tape recorder without the effect of methane oxidation. . . . .	85
5.5	Differences in $\delta\text{D}(\text{H}_2\text{O})$ between the simulation with and without the methane oxidation effect. . . . .	86
5.6	Averaged annual amplitudes of $\delta\text{D}(\text{H}_2\text{O})$ with altitude, with and without the effect of methane oxidation. . . . .	87
5.7	Zonally and seasonally averaged $\delta\text{D}(\text{H}_2\text{O})$ . . . . .	88
5.8	Zonal averages of monthly $\delta\text{D}(\text{H}_2\text{O})$ from the 380 to the 400 K isentrope. . . . .	90
5.9	Seasonally averaged $\delta\text{D}(\text{H}_2\text{O})$ from the 380 to the 400 K isentrope. . . . .	91
5.10	Zonal cross section of $\delta\text{D}(\text{H}_2\text{O})$ from $30^\circ\text{N}$ to $40^\circ\text{N}$ for JJA. . . . .	92

---

5.11	Difference in $\delta D(H_2O)$ between the zonal average from $80^\circ E$ to $180^\circ E$ and $140^\circ W$ to $40^\circ W$ for JJA. . . . .	93
5.12	$\delta D(H_2O)$ between the 370 and the 390 K isentrope for JJA and frame around the regions used for the correlation analysis. . . . .	94
5.13	Pearson's correlation coefficient of $\delta D(H_2O)$ between the tropical tape recorder signal and the ASM and the NAM. . . . .	94
5.14	$H_2O$ and $\delta D(H_2O)$ in the UTLS. . . . .	95
5.15	Relation between $H_2O$ and $\delta D(H_2O)$ in the UTLS in JJA. . . . .	96
5.16	Ice water content and $\delta D(H_2O)$ in ice in the UTLS in JJA. . . . .	97
5.17	Ice water content and $\delta D(H_2O)$ in ice at 14 km altitude in JJA. . . . .	98



# List of Tables

2.1	Stable water isotopologues: Molecules, abundances and molecular masses, IAEA (2009). . . . .	17
2.2	Kinetic isotope fractionation coefficients for CH <sub>3</sub> D, Röckmann et al. (2011). . . . .	24
3.1	Required modification of submodels for including the TENDENCY feature. . . . .	34
3.2	Stable water isotopologue-enabled GCMs. . . . .	42



# Appendix A

## Abbreviations

<b>ACE-FTS</b>	Atmospheric Chemistry Experiment - Fourier Transform Spectrometer (satellite instrument on SCISAT)
<b>ADVECT</b>	MESSy submodel for ADVECTION
<b>ASM</b>	Asian Summer Monsoon
<b>ATMOS</b>	Atmospheric Trace MOlecule Spectroscopy (space shuttle instrument)
<b>CARIBIC</b>	Civil Aircraft for the Regular Investigation of the atmosphere Based on an Instrument Container
<b>CCM</b>	Chemistry-Climate model
<b>CH4</b>	MESSy submodel for methane oxidation
<b>CHEM1D</b>	1-dimensional chemical transport model
<b>CHEM2D</b>	2-dimensional chemical transport model
<b>CLOUD</b>	MESSy submodel for large scale-CLOUDs
<b>CONVECT</b>	MESSy submodel for CONVECTive clouds
$\delta D$	Standardised isotope ratio w.r.t. Deuterium
$\delta^{18}O$	Standardised isotope ratio w.r.t. $^{18}O$
<b>DJF</b>	December January February
<b>ECHAM</b>	ECmwf HAMburg (global circulation model)
<b>ECHAM5-wiso</b>	5th generation ECHAM model with included water isotopologues
<b>EMAC</b>	ECHAM MESSy Atmospheric Chemistry (chemistry-climate model system)
<b>Envisat</b>	Environmental Satellite
<b>ESM</b>	Earth System Model
<b>FREE_VAL</b>	FREE running EMAC VALidation simulation
<b>FTIR</b>	Fourier Transform InfraRed spectroscopy (measurement device of CARIBIC)
<b>GCM</b>	General Circulation Model
<b>GISS-E</b>	Goddard Institute for Space Studies - ModelE (ESM)
<b>GNIP</b>	Global Network on Isotopes in Precipitation (measurement survey)
<b>HDO</b>	Isotopologue of water ( $^1H^2H^{16}O$ ) / deuterated water
<b>H<sub>2</sub><sup>18</sup>O</b>	Isotopologue of water ( $^1H^1H^{18}O$ )
<b>IAEA</b>	International Atomic Energy Agency
<b>JJA</b>	June July August

---

<b>LMDZ</b>	Laboratoire de Météorologie Dynamique Zoom (general circulation model)
<b>MAM</b>	March April May
<b>MESSy</b>	Modular Earth Submodel System (submodel-coupling interface)
<b>MIPAS</b>	Michelson Interferometer for Passive Atmospheric Sounding (satellite instrument on ENVISAT)
<b>MLS</b>	Microwave Limb Sounder (satellite instrument on the EOS (Earth Observing System) Aura satellite)
<b>NAM</b>	North American Monsoon
<b>Odin</b>	Satellite (named after god Odin)
<b>RAD4ALL</b>	MESSy submodel for RADiation
<b>SCISAT</b>	SCIENCE SATellite
<b>SD_REF</b>	EMAC REFERENCE simulation with Specified Dynamics
<b>SD_NOCD</b>	EMAC simulation with modified chemistry tendency for HDO (NO Chemical alteration of $\delta D$ ) with Specified Dynamics
<b>SMR</b>	Sub-Millimetre Radiometer (satellite instrument on Odin)
<b>SON</b>	September October November
<b>SURF</b>	ECHAM submodel for SURFace processes (note, that in EMAC versions 2.50 and newer, this has been replaced by the MESSy submodel SURFACE)
<b>TTL</b>	Tropical Tropopause Layer
<b>UTLS</b>	Upper Troposphere and Lower Stratosphere
<b>VDIFF</b>	ECHAM submodel for Vertical DIFFusion
<b>WMO</b>	World Meteorological Organization



# Appendix B

## MESSy TENDENCY user manual

### B.1 Introduction

Since the MESSy generic submodel TENDENCY was developed in a manner that all MESSy users can use and extend it to other sub- and basemodels, this document provides a more detailed description the submodel. TENDENCY is a comprehensive and easily expandable submodel to access process-based tendencies of state variables (including tracers) for analyses and further usage.

The outsourcing of the time integration and the tendency accounting for the prognostic variables from the respective submodels to the TENDENCY submodel is implemented for all physical and dynamical processes, as well as for several chemistry related submodels within the version 2.42 (or later) of the ECHAM/MESSy Atmospheric Chemistry (EMAC) model. As a pre-processor directive is used for the implementation, and the conventions follow the MESSy coding standard, the procedure can easily be extended to other submodels attached to the system or when a submodel is replaced. Due to its independency of the time integration scheme it is also applicable to other basemodels.

### B.2 Subroutines called from BMIL

The subroutine `main_tendency_initialize`

This subroutine

- reads the coupling (CPL) namelist from file *tendency.nml* and broadcasts its entries (Sect. B.4),
- assigns a unique identifier (“handle”) to the ECHAM5 basemodel specific processes (see Sect. B.3), which have not (yet) been reimplemented as MESSy submodels,
- registers the state variables (including tracers), which are subject to modification by these processes, and
- assigns handles to two additional generic processes (`mtend_diff` and `mtend_sum`) used for the optional closure test and registers all state variables for those.

### The subroutine `main_tendency_init_coupling`

With this subroutine the channels and channel objects for the full diagnostic output, the diagnostic sums and the closure test are defined, as requested by the user via the corresponding coupling (CPL) namelist (see Sect. B.4). For further information on channels and channel objects see Jöckel et al. (2010).

### The subroutine `main_tendency_global_end`

This subroutine displays the user requested tendency records in the log file. If the closure test is activated, the difference between the internal and the external tendencies (definition see corresponding article) are computed. With these differences the subroutine `compute_eps_and_clear` (see Sect. B.5) is called.

### The subroutine `main_tendency_reset`

In this subroutine all the internal tendencies are reset to zero at the end of every time step.

### The subroutine `main_tendency_free_memory`

In this subroutine the memory, which is used throughout the submodel and is not related to channel objects, is deallocated at the end of the model simulation.

### The subroutine `mtend_set_sqcst_scal`

SUBROUTINE <code>mtend_set_sqcst_scal</code> (scale_flag)			
name	type	intent	description
<b>mandatory arguments:</b>			
scale_flag	LOGICAL	IN	switch to enable wind scaling

This subroutine is specific for the ECHAM5 basemodel and it is called twice from within *physc*. It sets the internal LOGICAL `scale_flag` providing the information to TENDENCY, in which state the tendencies of the wind velocity components are: either scaled with the cosine of the latitude (`scale_flag = .TRUE.`), or unscaled (`scale_flag = .FALSE.`).

## B.3 Subroutines and functions called from SMIL

### The function `mtend_get_handle`

INTEGER FUNCTION <code>mtend_get_handle</code> (name [,lnew])			
name	type	intent	description
<b>mandatory arguments:</b>			
name	CHARACTER(LEN=*)	IN	name of calling submodel
<b>optional arguments:</b>			
lnew	LOGICAL	IN	handle already existing?

With this subroutine a unique process identifier of type `INTEGER` (called “handle”) is assigned to the calling process by its module name (`name`). The handle is stored within an internal structure. Calling this function multiple times with the same name will yield the same handle. The optional parameter `lnew` (default: `.TRUE.`) can be used to suppress (`lnew = .FALSE.`) the assignment of a new handle, i.e., to probe for the handle corresponding to a specific process (`name`). The handle is `-1`, if the process is not present / not running.

### The subroutine `mtend_register`

SUBROUTINE <code>mtend_register</code>		(handle ,mtend_id [,idt_1   idt])	
name	type	intent	description
<b>mandatory arguments:</b>			
handle	<code>INTEGER</code>	IN	process identifier
mtend_id	<code>INTEGER</code>	IN	variable identifier
<b>optional arguments:</b>			
idt_1	<code>INTEGER, DIMENSION(:)</code>	IN	list of tracer indices
idt	<code>INTEGER</code>	IN	tracer index

Within this subroutine every calling process or submodel registers those prognostic variables, which it is going to alter. The information is stored as `LOGICAL` in an internal structure for each process - prognostic variable pair. This information is used for subsequent computations within `TENDENCY`.

The optional parameters define, if the submodel is used for a prognostic variable of the basemodel (no optional arguments), a single tracer (`idt`) or a list of tracers (`idt_1`). Further information on tracers and tracer identifiers can be found in Jöckel et al. (2008).

The identifiers for the prognostic variables are predefined as `INTEGER PARAMETERS`:

- `mtend_id_t` for the temperature,
- `mtend_id_q` for the specific humidity,
- `mtend_id_xl` for the liquid water content,
- `mtend_id_xi` for the ice water content,
- `mtend_id_u` for the u-wind component,
- `mtend_id_v` for the v-wind component,

for the ECHAM5 specific prognostic variables, and

- `mtend_id_tracer` for tracers.

The subroutine `mtend_get_start_l/_g`

SUBROUTINE <code>mtend_get_start_l/_g</code> <sup>*)</sup>		(mtend_id [,v0] [,idt] [,v0t])	
name	type	intent	description
<b>mandatory arguments:</b>			
mtend_id	INTEGER	IN	variable identifier
<b>optional arguments:</b>			
v0	REAL(DP), DIMENSION(:, :, /, :)*)	OUT	start value
idt	INTEGER	IN	tracer index
v0t	REAL(DP), DIMENSION(:, :, /, :)*)	OUT	start value of all tracers

<sup>\*)</sup>Note: The two subroutines (`mtend_get_start_l` and `mtend_get_start_g`) differ by the rank of the parameters `v0` and `v0t`. The respective subroutine has to be chosen depending on the main entry point from where the corresponding process performs: some are called from the outer (global) loop and some from the inner (local) loop (see also Sect. 3.2.1.3).

This subroutine computes the initial values of the prognostic variable defined by its identifier `mtend_id` (see Sect. B.3). This is done by adding the product of the current tendency (i.e., the sum of all tendencies of prior processes in the same time step) with (two times) the length of the time step to the value of the respective variable of the time step before.

The optional arguments determine, if the subroutine is used for one of the basemodel specific prognostic variables (`v0`), a single tracer (`v0` and `idt`) or the complete tracer set (`v0t`). For usage with tracers the variable identifier `mtend_id` must be `mtend_id_tracer`, for prognostic variables the corresponding identifier (see Sect. B.3). Further information on tracer sets, tracers and tracer identifiers can be found in Jöckel et al. (2008).

The subroutine `mtend_add_l/_g`

SUBROUTINE <code>mtend_add_l/_g</code> <sup>*)</sup>		(handle ,mtend_id [,px] [,idt] [,pxt])	
name	type	intent	description
<b>mandatory arguments:</b>			
handle	INTEGER	IN	process identifier
mtend_id	INTEGER	IN	variable identifier
<b>optional arguments:</b>			
px	REAL(DP), DIMENSION(:, :, /, :)*)	IN	tendency to add
idt	INTEGER	IN	tracer index
pxt	REAL(DP), DIMENSION(:, :, /, :)*)	IN	tendency to add for all tracers

<sup>\*)</sup>Note: The two subroutines (`mtend_add_l` and `mtend_add_g`) differ by the rank of the parameters `px` and `pxt`. The respective subroutine has to be chosen depending on the main entry point from where the corresponding process performs: some are called from the outer (global) loop and some from the inner (local) loop (see also Sect. 3.2.1.3).

With these subroutines the individual process tendencies for all variables are collected. They are used to update the total tendency and the internal sum of tendencies. A copy of

the tendency of every process - prognostic variable pair (as requested in the CPL namelist, see Sect. B.4) is stored in a separate channel object. Additional messages, useful for development, are optionally printed to the log file (see Sect. B.4).

The optional arguments determine, if the subroutine is used for one of the basemodel specific prognostic variables (`px`), a single tracer (`px` and `idt`), or the complete tracer set (`pxt`). For usage with tracers the variable identifier `mtend_id` must be `mtend_id_tracer`, for prognostic variables the respective identifier (see Sect. B.3). Further information on tracer sets, tracers and tracer identifiers can be found in Jöckel et al. (2008).

## B.4 User interface

### TENDENCY CPL namelist

The coupling (CPL) namelist of the TENDENCY submodel comprises entries to control the creation of additional channels and corresponding channel objects, the conduction of an internal closure test and the output of additional information. All options are independent of each other and therefore not exclusive:

- `l_full_diag` is a logical switch, which enables the full diagnostic output. If set `.TRUE.` (default is `.FALSE.`), a channel object is created for each possible process - prognostic variable pair.
- `l_closure` is a logical switch for the internal closure test. The default is `.FALSE.`, the test is enabled if `l_closure` is set to `.TRUE.`. If enabled, two extra pseudo process identifiers (`I_HANDLE_SUM` and `I_HANDLE_DIFF`) are defined (see Sect. B.2).
- `l_clos_diag` is a logical switch, which causes additional output to the log file during the model execution, if set `.TRUE.` (default is `.FALSE.`). The output comprises information on the external and the internal tendencies and their differences, and is mostly used for debugging purposes, e.g., when including a new submodel for TENDENCY.
- Individual output switches for the prognostic variables serve to diagnose individual tendencies from specific processes (or tailor made sums of those). With this approach, only the minimum memory required is used: For every state variable (or tracer), one channel object is created for each requested “sum over processes”, plus one additional channel object summing all “unaccounted” processes, which are not part of the user specified list. The syntax is

```
TDIAG(i) = 'X', 'p1;p2+p3;...;pn',
```

where `i` is an arbitrary but unique number, `X` is the name of the prognostic variable (or tracer), and `p1` to `pn` are the names of the processes. For the example

```
TDIAG(1) = 't' , 'vdiff; cloud + rad4all + convect; surf + dyn',
```

four channel objects are created with temperature tendencies: One for the tendency caused by *vdiff*, one for the sum of *cloud*, *rad4all* and *convect*, one for the sum of *surf* and *dyn*, and one for the sum of all not listed processes, i.e., for the “unaccounted”.

### The subroutine `mtend_request`

SUBROUTINE <code>mtend_request</code>		(status ,process_string ,mtend_id ,ptr_out [,idt])	
name	type	intent	description
<b>mandatory arguments:</b>			
status	INTEGER	OUT	
process_string	CHARACTER(LEN=32)	IN	name of requested process
mtend_id	INTEGER	IN	variable identifier
ptr_out	REAL(DP), DIMENSION(:, :, :)	POINTER	pointer to requested tendency array
<b>optional arguments:</b>			
idt	INTEGER	IN	tracer index

This subroutine can be called during the coupling phase from any submodel to access the individual tendency (of the variable defined by `mtend_id`) from any other submodel (with name `process_string`). One channel object is generated for the tendency of each requested process - prognostic variable pair within the TENDENCY submodel. The pointer (`ptr_out`) to its corresponding memory is returned to the calling submodel for further access. By calling the subroutine `mtend_add` (Sect. B.3) from the requested submodel (with name `process_string`), TENDENCY stores a copy of the corresponding individual tendency in the channel object memory accessible by the pointer `ptr_out`.

The optional parameter `idt` (a tracer identifier) determines the individual tracer, if a tracer tendency is requested (`mtend_id = mtend_id_tracer`, see Sect. B.3).

Further information on tracers and tracer identifiers can be found in Jöckel et al. (2008).

## B.5 Private subroutines

### The subroutine `compute_eps_and_clear`

SUBROUTINE <code>compute_eps_and_clear</code>		(text ,array ,array_diff)	
name	type	intent	description
<b>mandatory arguments:</b>			
text	CHARACTER(LEN=*)	IN	variable string
array	REAL(DP), DIMENSION(:, :, :)	POINTER	pointer to external tendency array
array_diff	REAL(DP), DIMENSION(:, :, :)	POINTER	pointer to difference between internal and external tendency array

If `l_closure` (see Sect. B.4) is set `.TRUE.`, this subroutine computes an  $\varepsilon = (\max |xte_e|) \cdot 10^{-10}$ , where  $xte_e$  denotes the external tendency, for each state variable at the end of each time step. The difference between the internal and the external tendency should be smaller than  $\varepsilon$ . If this condition is not fulfilled, an error message is displayed in the log file and the model execution is terminated.

The subroutine `tendency_read_namelist_cpl`

SUBROUTINE <code>tendency_read_namelist_cpl</code> (status, iou)			
name	type	intent	description
<b>mandatory arguments:</b>			
status	INTEGER	OUT	
iou	INTEGER	IN	

With this subroutine the coupling (CPL) namelist is read from the file *tendency.nml*.

The subroutine `tendency_parse_nml_cpl`

This subroutine parses the namelist strings. At first the strings are separated by the semicolons into the diagnostic sum strings. In the next step, the latter are separated by the plus signs into the individual process strings. This allows to assign the process identifiers to generate the required channel objects.





# Danksagung

Mein Dank gilt Prof. Dr. Robert Sausen für das Ermöglichen dieser Arbeit sowie seine hilfreichen Anregungen und Kommentare während der gesamten Zeit.

Vielen Dank auch an Prof. Dr. George Craig für die Übernahme des Zweitgutachtens.

Unermesslicher Dank gilt meinem Betreuer Dr. Patrick Jöckel, der immer ein offenes Ohr für mich hatte, mir mit Rat und Tat zur Seite stand und scheinbar sogar noch in jenen Phasen an ein Gelingen der Arbeit glaubte, als ich dies selbst nicht mehr tat, und natürlich für die Idee dieses Thema zu behandeln.

Ein umfassendes Dankeschön geht an das Institut für Physik der Atmosphäre des DLR Oberpfaffenhofen, im Speziellen an Abteilung 1 für die Kollegialität und das angenehme Arbeitsumfeld. Insbesondere seien Sabine, Hella und Duy zu erwähnen, die sich stets für mein Thema interessierten und mir wertvolle Tipps gaben. Vielen Dank auch an meine Bürokollegin Eleni und den Rest der Mittagsrunde, Mattia und Sabrina für die Gespräche zur Ablenkung sowie über die Arbeit.

Bedanken möchte ich mich ebenfalls bei den Institutsdirektoren Prof. Dr. Markus Rapp und Prof. Dr. Ulrich Schuhmann für das Ermöglichen diese Arbeit anzufertigen und die kritischen Kommentare dazu.

Dank geht ebenfalls an das SHARP Projekt, in dem ich einen sehr fruchtbaren Rahmen für meine Arbeit vorfinden durfte. Im speziellen seien hier Dr. Stefan Lossow sowie Prof. Dr. Gabriele Stiller für die wertvollen Gespräche und das Bereitstellen der Satellitendaten erwähnt.

Großer Dank gilt auch Dr. Martin Werner für seinen aufschlussreichen Besuch am DLR sowie die Bereitstellung des ECHAM5-wiso Codes, Prof. Dr. Thomas Röckmann für das Bereitstellen der Radiosondendaten und Alex für die Korrekturen.

Ein herzlicher Dank gilt all meinen Freunden die mich immer wieder daran erinnern, dass es neben der Welt der Wissenschaft auch ein normales Leben gibt.

Der wohl größte Dank gilt meinen Eltern und meiner gesamten Familie, ohne die sowieso nichts von alledem entstanden wäre.

Ganz besonderer Dank gilt Anna.



# Lebenslauf

## Persönliche Daten

---

Name:	Roland Eichinger
Geburtsdatum:	26.05.1982
Geburtsort:	München

## Schulbildung

---

09/1988 - 07/1992	Grundschule Grafing
09/1992 - 07/2002	Gymnasium Grafing Allgemeine Hochschulreife (Abitur)

## Studium

---

10/2003 - 04/2010	Studiengang Meteorologie an der Ludwig-Maximilians-Universität München
04/2009 - 04/2010	Diplomarbeit am Alfred Wegener Institut für Polar- und Meeresforschung, Bremerhaven: <i>Analyse thermohaliner Ozeandynamik - Eine konzeptionelle Modellstudie mit Meereis</i>
04/2011 - 03/2014	Promotionsstudium an der Ludwig-Maximilians- Universität
seit 10/2010	Doktorand am Institut für Physik der Atmosphäre am Deutschen Zentrum für Luft- und Raumfahrt e.V., Oberpfaffenhofen